A soft-magnetic slender body in a highly viscous fluid

James D. Martindale

A dissertation submitted to the faculty of the University of North Carolina at Chapel Hill in partial fulfillment of the requirements for the degree of Doctor of Philosophy in the Department of Mathematics.

Chapel Hill
2013

Approved by:

Roberto Camassa

Richard McLaughlin

Laura Miller

Sorin Mitran

Leandra Vicci

Abstract

JAMES D. MARTINDALE: A soft-magnetic slender body in a highly viscous fluid
(Under the direction of Roberto Camassa and Richard McLaughlin)

Theoretical, numerical, and experimental studies for a rotating soft-magnetic body in low Reynolds number flow which imitates the motion of nodal cilia are considered. This includes a discussion of the torque balance for the coupled magnetic-fluid interaction for a rod rotating in a viscous fluid, and a discussion of experimental results which have suggested alterations to the current slender body theory used to find the flow around a rotating rod.

Firstly, the current state of the theory for a slender rod attached to a no-slip plane sweeping out a cone will be discussed in terms of the singularity strength distribution which allows us to calculate the forces and torques on the slender body. This theory has been developed in the works of Terry Jo Leiterman [**11**] and Longhua Zhao [**16**] for straight and bent rod geometries respectively. Analogous techniques of the classical fluid slender body theory are then applied for a soft-magnetic rod in free space in order to generate the appropriate strength distribution for the singularities placed along the center line of the rod. A discussion of the magnetic slender body theory is presented for a rod in free space and for a rod held fixed about a point in a uniform background field. Once the appropriate strength distribution is found through asymptotic matching, the magnetic torque on the rod may be calculated.

A steady-state problem is considered where the position of the rod relative to the magnetic field may be found by balancing the fluid and magnetic torques. For a straight rod sweeping an upright cone in a uniform background magnetic field, this problem reduces to finding the solution to a polynomial whose arguments are

trigonometric functions of the angles involved in describing the position of the rod and magnetic field. From this polynomial, we may construct explicit intervals in which the solution is unique. We also examine various limiting cases that should be seen in the physical experiment as a first-order check to the validity of the magnetic model. The magnetic problem is then extended to bent rod geometries, again using similar techniques derived in the fluid slender body theory. This bent rod geometry creates rather unwieldy expressions for the fluid and magnetic torque, but nonetheless, the torque balance may be solved numerically. This theory is not currently put to use in our experiment since the exact properties of our driving magnet have not been considered.

Next, a discussion of the current state of our experiments for a rod rotating in a viscous fluid is presented. It is of great importance to understand the results of our Lagrangian particle tracking which were discussed for both straight and bent pin geometries by Leiterman and Zhao. Progress has been made in the procedure for tracking the rod which ensures that better measurements for the angles which describe the rod position are passed the the theory for comparison. Key differences between the theory and experimental results are presented. In order to corroborate these Lagrangian results and suggest alterations to the current fluid theory, we use a full three-dimensional particle image velocimetry (PIV) to capture an Eulerian view of the fluid flow structure in a horizontal plane slightly above the tip of the rotating rod. A discussion of the experimental setup and parameters is discussed, as well as the metrics we will use to compare the two experimental methods. Results of these experiments are then compared with the theory in various regards.

Finally, alterations to the current theory including a consideration of the free surface and lubrication effects are discussed. A comparison is made between particle trajectories for a sphere in a uniform flow over a plane using lubrication theory and singularity theory to establish whether this effect will be non-negligible in our experiment.

Acknowledgements

To my parents, Rich and Jenny, for always believing in me when I did not believe in myself, for teaching me independent thought and instilling in me a spirit which questions everything and a mind that seeks to understand. To my brother Kyle, whose courage to do what his heart tells him makes me proud. To Grammy, Paw-Paw, Oma, and Opa for their support over the years, and for never letting me miss out on a chance to better myself.

To my advisors, Rich and Roberto, for sticking with me all of these years, and for teaching me what it means to be a researcher. To Leandra for always having brilliant physical insight into the experimental process, for being an integral member of our research group, and for sitting on my committees.

To Greg, Laura, and Sorin for giving of their time to sit on my committees, and for giving their insight regarding my work. To Longhua Zhao, who continues to be a mentor, for her willingness to teach me the experimental process, and for her continued support and work for the RMX research group. To David Adalsteinsson for helping me with image analysis procedures that greatly improved my rod tracking results.

To Andrea, Andrew, Brad, Dan, Emily, Keith, Lauren, Matt, and Sam.

Finally, I must acknowledge the grants RTG NSF DMS-0502266 and NSF DMS-1009750 for providing financial support which allowed me to focus on research, and the department of mathematics for finding me teaching positions which provided financial support as well as contributing to my growth as an instructor.

Table of Contents

List of Figures

CHAPTER 1

Introduction: background information and slender body theory for a rod sweeping a cone in a highly viscous fluid

1.1. A slender rod sweeping a cone above an upright plane

The motion of a slender body sweeping a cone in a highly viscous fluid is important to understand because of its many biological applications regarding the spinning motion of cilia. The flows generated by such motion are critical to many biological organisms, and govern phenomena such as left-right symmetry breaking in developing mammalian embryos where nodal cilia undergo rotational motion [**15**]. The exact velocity field for a spheroid sweeping a double cone in free space has been obtained in Camassa et al [**2**], and both the velocity field and particle trajectories have been obtained for a slender body sweeping out an upright cone above a no-slip plane using classical slender body theory and an image method [**11**].

We model a nodal cilia as a rigid slender rod whose motion is then constrained to be purely rotational. The large-scale flow structures as well as particle trajectories are highly dependent on rod geometry. Terry Jo Leiterman discussed the case of a

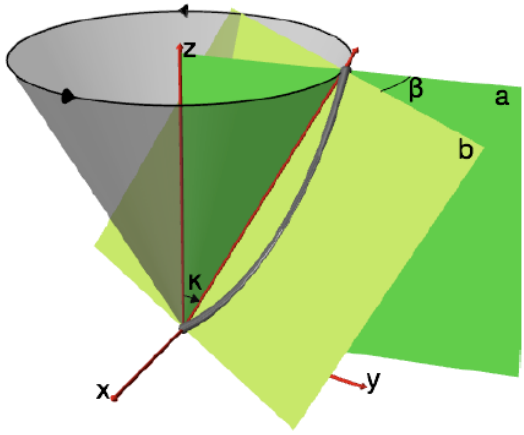

FIGURE 1.1. Rod geometry (Zhao, 2010).

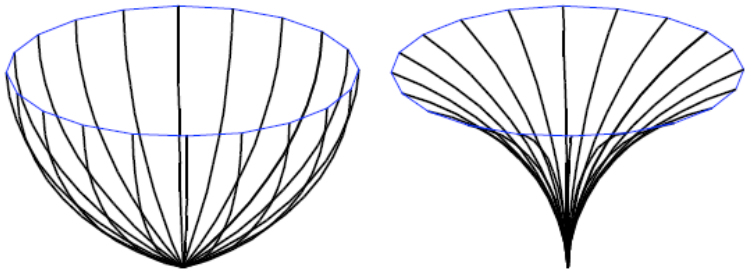

(a) Belly out ($\beta = 0$)

(b) Belly in ($\beta = \pi$)

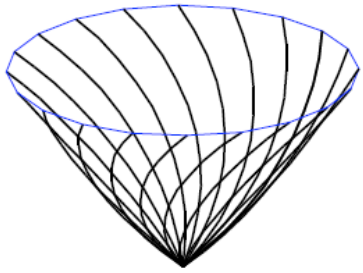

(c) Scoop ($\beta = \frac{\pi}{2}$)

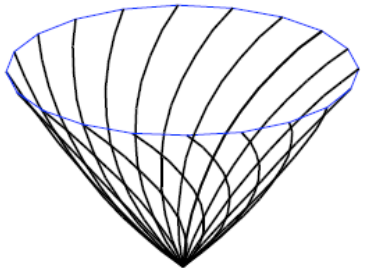

(d) Anti-scoop ($\beta = \frac{3\pi}{2}$)

FIGURE 1.2. Several examples of scooping angles (Zhao, 2010).

straight rod sweeping a cone above a no-slip plane [**11**], and Longhua Zhao extended this result to a bent rod above a no-slip plane [**16**]. The geometry of the problem is shown in Figure 1.1 [**16**]. The rod position may be described by a cone angle κ, defined as the angle between the chord of the rod and the cone axis, and a scooping angle β, defined as the angle between the plane of the rod and the vertical plane through the cone axis. Note that for a straight rod, there is no scooping angle.

In each case, the velocity field is contructed in the body frame where the rod is fixed in the presence of a rotational background flow. Stokeslets, the primary Green's functions of Stokes flow, are then distributed along the center-line of the rod. The strength distribution of the Stokeslets are found by asymptotic matching in the velocity field on the rod surface using a no-slip boundary condition. To enforce a no-slip boundary condition on the plane, image singularities are distributed in a prescribed way below the plane. This solution with Stokeslet and image singularity distribution is termed the Blakeslet solution. A transformation from the body to lab frame allows us to examine particle trajectories.

Further discussion of the extremely interesting case of a tilted cone may be found in Zhao [**16**]. This case of a tilted cone produces a fully time dependent flow in the body frame. Here, I will constrain the discussion to the case of a rod sweeping out an upright cone above a no-slip plane. The Blakeslet problem for a straight rod geometry has been discussed in detail [**11**]. We construct the solution by employing three fundamental singularities, the Stokeslet, Stokes doublet, and potential doublet (a point-source dipole). The construction and strength of the image singularities is found *a posteriori* in a way which satisfies the no-slip condition on the plane. A review of these singularities may be found in Blake & Chwang [**1**] and Chwang & Wu [**7**]. The velocity field satisfying

$$\begin{aligned} \mu\nabla^2\mathbf{u}_B + 8\pi\mu\boldsymbol{\alpha}\delta(\mathbf{x}-\mathbf{s}) &= \nabla p, \\ \nabla\cdot\mathbf{u}_B &= 0, \\ \mathbf{u}_B|_{x=0} &= 0 \end{aligned}$$

in the upper half space $\{\mathbf{x}=(x,y,z)\in\mathbb{R}^3 | z\geq 0\}$ is given as the Blakeslet $\mathbf{u}_B(\mathbf{x}-\mathbf{s};\boldsymbol{\alpha})$ defined as

$$\begin{aligned} \mathbf{u}_B(\mathbf{x}-\mathbf{s};\boldsymbol{\alpha}) &= \mathbf{u}_S(\mathbf{x}-\mathbf{s};\boldsymbol{\alpha}) + \mathbf{u}_S(\mathbf{x}-\mathbf{s};-\boldsymbol{\alpha}) \\ &\quad +\mathbf{u}_{SD}(\mathbf{x}-\mathbf{s}';\mathbf{e}_z,2h\boldsymbol{\alpha}') + \mathbf{u}_D(\mathbf{x}-\mathbf{s}';-2h^2\boldsymbol{\alpha}') \end{aligned}$$

where $\mathbf{s}=(s_1,s_2,s_3)$ is the location of the Stokeslet, $\mathbf{s}'=(s_1,s_2,-s_3)$ is the location of the image system, $\boldsymbol{\alpha}=(\alpha_1,\alpha_2,\alpha_3)$ is the strength of the Stokeslet, $\boldsymbol{\alpha}=(\alpha_1,\alpha_2,-\alpha_3)$, and $h=s_3$ is the distance from the Stokeslet to the plane.

When a slender rod sweeps an upright cone, the cone angle is equivalent to the chord angle, defined as the angle between the chord of the rod and the positive z-axis. If this rod has length ℓ and angular velocity $\boldsymbol{\omega}=(0,0,\omega)$, the velocity field may be

described as

$$\begin{aligned}
\mathbf{u}(\mathbf{x}) &= \mathbf{U}(\mathbf{x}) + \int_0^\ell (\mathbf{u}_S(\mathbf{x}-\mathbf{s};\boldsymbol{\alpha}(s)) + \mathbf{u}_S(\mathbf{x}-\mathbf{s};-\boldsymbol{\alpha}(s)) \\
&\quad +\mathbf{u}_{SD}(\mathbf{x}-\mathbf{s}';\mathbf{e}_z,2h\boldsymbol{\alpha}'(s)) + \mathbf{u}_D(\mathbf{x}-\mathbf{s}';-2h^2\boldsymbol{\alpha}'(s)))ds \\
&= \mathbf{U}(\mathbf{x}) + \int_0^\ell \frac{\boldsymbol{\alpha}(s)}{|\mathbf{x}-\mathbf{x}_s|} + \frac{(\mathbf{x}-\mathbf{x}_s)((\mathbf{x}-\mathbf{x}_s)\cdot\boldsymbol{\alpha}(s))}{|\mathbf{x}-\mathbf{x}_s|^3} \\
&\quad -\left(\frac{\boldsymbol{\alpha}(s)}{|\mathbf{x}-\mathbf{x}_s|} + \frac{(\mathbf{x}-\mathbf{x}_s)((\mathbf{x}-\mathbf{x}_s)\cdot\boldsymbol{\alpha}(s))}{|\mathbf{x}-\mathbf{x}_s|^3}\right) \\
&\quad +2z_s\left(\frac{\boldsymbol{\alpha}'(s)}{|\mathbf{x}-\mathbf{x'}_s|^3} + \frac{(\mathbf{x}-\mathbf{x'}_s)\times\mathbf{e}_z\times\boldsymbol{\alpha}'(s)}{|\mathbf{x}-\mathbf{x'}_s|^3}\right. \\
&\quad \left. + \frac{3z(\mathbf{x}-\mathbf{x'}_s)((\mathbf{x}-\mathbf{x'}_s)\cdot\boldsymbol{\alpha}'(s)}{|\mathbf{x}-\mathbf{x'}_s|^5}\right) ds
\end{aligned}$$

where $\mathbf{U}(\mathbf{x}) = (\omega y, -\omega x, 0)$ is the rotating background flow in the body frame, $\mathbf{x}_s = (s\sin\kappa, 0, s\cos\kappa)$, $\mathbf{x'}_s = (s\sin\kappa, 0, -s\cos\kappa)$ for a straight rod, and $\boldsymbol{\alpha}(s) = \boldsymbol{\alpha}'(s) = \frac{\omega\epsilon\sin\kappa}{2}(0,s,0)$ where the slenderness parameter $\epsilon = \log^{-1}\left(\frac{\ell}{r}\right)$. Details regarding the calculation of the Stokeslet strength distribution can be found in Leiterman [**11**].

For the bent rod geometry, the center-line is parametrized by

$$\begin{aligned}
x_s &= -2a\cos\beta\cos\kappa\sin\left(\frac{\ell-s}{2a}\right)\sin\left(\frac{s}{2a}\right) + 2a\sin\kappa\cos\left(\frac{\ell-s}{2a}\right)\sin\left(\frac{s}{2a}\right) \\
y_s &= -2a\sin\beta\sin\left(\frac{\ell-s}{2a}\right)\sin\left(\frac{s}{2a}\right) \\
z_s &= 2a\cos\kappa\cos\left(\frac{\ell-s}{2a}\right)\sin\left(\frac{s}{2a}\right) + 2a\cos\beta\sin\kappa\sin\left(\frac{\ell-s}{2a}\right)\sin\left(\frac{s}{2a}\right)
\end{aligned}$$

for $0 \le s \le \ell$ where $K = \frac{1}{a}$ is the local non-dimensional curvature of the body center-line with respect to the body length. The Stokeslet strength in the Blakeslet is then given by

$$\boldsymbol{\alpha} = Rdiag(\frac{\epsilon}{4}, \frac{\epsilon}{2}, \frac{\epsilon}{2})R^{-1}\mathbf{U}$$

where $\mathbf{U} = \boldsymbol{\omega}\times\mathbf{x}_s$ and $R = (\mathbf{e}_\tau, \mathbf{e}_\eta, \mathbf{e}_\beta)$, where $\mathbf{e}_\tau = \frac{\partial\mathbf{x}_s}{\partial s}$, $\mathbf{e}_\eta = \frac{1}{K}\frac{\partial^2\mathbf{x}_s}{\partial s^2}$, and $\mathbf{e}_\beta = \mathbf{e}_\tau\times\mathbf{e}_\eta$. This matrix is explicity stated in Zhao [**16**].

With the rod length ℓ and curvature K known, this prescription allows us to find the velocities in the body frame given the angular speed ω and the set of angles (κ, β) which describe the position of the rod. These quantities are obtained experimentally and in Chapter 3, which concerns Lagrangian experiments with both straight and bent pin geometries, a discussion of the methods and accuracy for obtaining these quantities is presented.

1.2. Hydrodynamic torque

We present a discussion of the fluid torques which has been developed by Chwang & Wu [**7**], and for the specific rod geometry above by Leiterman [**11**] and Zhao [**16**]. The hydrodynamic force which the fluid exerts on the slender body is given by

$$\mathbf{f}(\mathbf{x}_0) = -\boldsymbol{\sigma} \cdot \hat{\mathbf{n}}$$

where $\mathbf{x}_0$ is a point on the surface of the body, $\hat{\mathbf{n}}$ is the outward normal vector at the point $\mathbf{x}_0$, and

$$\sigma_{ik} = -p\delta_{ik} + \mu \left(\frac{\partial u_i}{\partial x_k} + \frac{\partial u_k}{\partial x_i} \right)$$

is the stress tensor for a fluid in motion with velocity $\mathbf{u}$. The quantity p represents the pressure field, and δ_{ik} is the Kronecker delta function. With this definition of the hydrodynamic force, we may write the following expression for the torque about the origin:

$$\mathbf{T}_F(0) = -\int_S \mathbf{x} \times (\boldsymbol{\sigma} \cdot \hat{\mathbf{n}}) dS$$

where the subscript F will denote the hydrodynamic torque in order to distinguish it from the magnetic torque to be discussed in Chapter 2. The divergence theorem allows us to write the torque as a volumetric integral

$$\mathbf{T}_F(0) = -\int_V \mathbf{x} \times (\nabla \cdot \boldsymbol{\sigma}) dV$$

The divergence of this stress tensor is given by $\nabla \cdot \boldsymbol{\sigma} = -8\pi\mu\boldsymbol{\alpha}\delta(\mathbf{x}-\mathbf{y})$. Using the properties of the delta function, we can then transform the torque into a line integral given by

$$\mathbf{T}_F(0) = \int_0^\ell \mathbf{x}_s \times \boldsymbol{\alpha}(s) ds$$

where $\mathbf{x}_s$ is the center-line parametrization. In the next chapter, I carry out a discussion which takes into account the magnetic permeability of the rod to calculate a magnetic torque. From there, a discussion is presented of a torque balance to find the angles (κ, β) which determine the position of the rod given only the angular speed ω.

CHAPTER 2

A magnetically driven slender body

2.1. Problem Statement

It is important to understand the role that magnetism plays in the driven motion of model cilia since there are a variety of applications at micro- and macro-scales. Magnetic drivers are commonly used to control the motion of elastic cilia models as well as the macro-scale rigid nodal cilia model which was considered in Chapter 1. In this chapter, we discuss a coupled magnetic-hydrodynamic system by creating a model for the magnetic field induced by a slender soft-magnetic rod in a uniform background field which employs a singularity method analogous to the fluid model. This model allows us to understand the motion and orientation of a rod in free space, as well as its magnetic torque. We may also this so-called generator solution to obtain a slender body theory for a soft-magnetic rod in the upper half space with a base fixed at the origin. Embedding this rod in a highly viscous fluid will merit the consideration of a static problem where the uniform background magnetic field is rotating with the same angular speed as the rod after clearing some initial transient start-up time [**4**].

The main difference between the theory discussed in Chapter 1 is that here we may consider a potential problem with Dirichlet boundary conditions on the surface of the rod. It should also be noted that the plane plays no real role in the magnetic theory other than to define an origin about which the rod is constrained to move. The basic laws of magnetostatics are given by

$$\begin{aligned} \nabla \times \mathbf{B} &= \frac{4\pi k}{c^2}\mathbf{J} \\ \nabla \cdot \mathbf{B} &= 0 \end{aligned}$$

where $k = \frac{1}{4\pi\epsilon_0}$ is Coulomb's constant with ϵ_0 being the permittivity of free space and $c^2 = \frac{1}{\mu_0\epsilon_0}$ where μ_0 is the permeability of free space. In the static problem, we may assume that the current density is zero, and thus we may express the magnetic field $\mathbf{B}$ as a gradient of a magnetic scalar potential $\mathbf{B} = -\nabla\Phi_M$. In this case, the equations above reduce to Laplace's equation for Φ_M, and we may use techniques of classic electrostatics to solve this system.

Defining a background magnetic field $\mathbf{B_0}$ and a slender body Ω whose boundary is given as $\partial\Omega$, the problem we attempt to solve becomes

$$\begin{aligned} \nabla^2\Phi_M &= 0 \text{ outside } \Omega \\ \Phi_M|_{\partial\Omega} &= C \\ \nabla\Phi_M &\to \mathbf{B_0} \text{ as } |\mathbf{x}| \to \infty \end{aligned}$$

where C is some constant, which is justified in this static case. In order to solve this problem, we wish to form a generator solution where we first consider a straight rod with whose boundary is defined by

$$\partial\Omega = \{\mathbf{x} \in \mathbb{R}^3 | x_1^2 + x_2^2 = r^2, x_3 \in [-\ell, \ell]\}$$

We will write the full potential as a sum of the potential defined by the background magnetic field and the magnetic potential induced by the rod $\Phi_M = \Phi_0 + \Phi_\Omega$. As was previously stated, we will solve for this induced potential by distributing singularities along the rod center-line and solving for their strength distribution by asymptotic matching of the boundary condition. In this problem, to retain some physical relevance, I consider the point-source dipole, whose potential is given by

$$\Phi_D(\mathbf{x} - \mathbf{x}_s; \boldsymbol{\gamma}) = \frac{\mathbf{x} - \mathbf{x}_s}{|\mathbf{x} - \mathbf{x}_s|^3} \cdot \boldsymbol{\gamma}$$

where $\mathbf{x} = (x_1, x_2, x_3)$, $\mathbf{x}_s = (0, 0, s)$, and $\boldsymbol{\gamma}$ is the strength of the dipole located at the point $\mathbf{x}_s$. The total potential induced by a distribution of these singularities is

$$\Phi_\Omega = \int_{-\ell}^{\ell} \Phi_D(\mathbf{x} - \mathbf{x}_s; \boldsymbol{\gamma}(s))ds$$

where the strength distribution is defined as $\boldsymbol{\gamma}(s) = (g_1(s), g_2(s), g_3(s))$ where

$$g_i(s) = p_{0,i} + p_{1,i}s + p_{2,i}s^2, \ i = 1, 2, 3$$

We find the coefficients through the matching condition $\Phi_M|_{\partial\Omega} = C$, which with the definitions above can be written as

$$C - \Phi_0|_{\partial\Omega} = \left(\int_{-\ell}^{\ell} \Phi_D(\mathbf{x} - \mathbf{x}_s; \boldsymbol{\gamma}(s))ds \right) |_{\partial\Omega} = \int_{-\ell}^{\ell} \frac{x_1 g_1(s) + x_2 g_2(s) + (x_3 - s)g_3(s)}{(r^2 + (x_3 - s)^2)^{3/2}} ds$$

We approach this integral by making the substitution $t = \frac{x_3 - s}{r}$. The integral on the right hand side of the above equation then becomes

$$\frac{1}{r^2} \int_{(x_3-\ell)/r}^{(x_3+\ell)/r} \frac{x_1 g_1(x_3 - rt) + x_2 g_2(x_3 - rt) + rt g_3(x_3 - rt)}{(1 + t^2)^{3/2}} ds$$

In order to investigate the slender body limit of the integral, I define the slenderness ratio $\delta = \frac{r}{\ell}$ and define

$$\begin{aligned} a &= \frac{x_3 - \ell}{\ell} \\ b &= \frac{x_3 + \ell}{\ell} \end{aligned}$$

Then in terms of our slenderness ratio, the matching problem becomes

$$C - \Phi_0|_{\partial\Omega} = \frac{1}{\delta^2 \ell^2} \int_{a/\delta}^{b/\delta} \frac{x_1 g_1(x_3 - \delta\ell t) + x_2 g_2(x_3 - \delta\ell t) + \delta\ell t g_3(x_3 - \delta\ell t)}{(1 + t^2)^{3/2}} ds$$

2.2. Generator solution for a uniform background magnetic field

We consider a general uniform magnetic field $\mathbf{B_0} = (B_1, B_2, B_3)$, which implies that the background potential is given by

$$\Phi_0 = \mathbf{B}_0 \cdot \mathbf{x} + C_1$$

where C_1 is a constant and the matching condition presented in the previous section becomes

$$-B_1x_1 - B_2x_2 - B_3x_3 = \frac{1}{\delta^2\ell^2}\int_{\frac{a}{\delta}}^{\frac{b}{\delta}} \frac{x_1g_1(x_3 - \delta\ell t) + x_2g_2(x_3 - \delta\ell t) + \delta\ell t g_3(x_3 - \delta\ell t)}{(1+t^2)^{3/2}} ds$$

where the constant has been disregarded. Using the definition of the polynomials $g_i(s)$, we can write out a complete expression for our matching problem.

$$\begin{aligned} -B_1x_1 - B_2x_2 - B_3x_3 &= \frac{1}{\delta^2\ell^2}\int_{\frac{a}{\delta}}^{\frac{b}{\delta}} \left(\frac{x_1(p_{0,1} + p_{1,1}(x_3 - \delta\ell t) + p_{2,1}(x_3 - \delta\ell t)^2)}{(1+t^2)^{3/2}} \right) ds \\ &+ \frac{1}{\delta^2\ell^2}\int_{\frac{a}{\delta}}^{\frac{b}{\delta}} \left(\frac{x_2(p_{0,2} + p_{1,2}(x_3 - \delta\ell t) + p_{2,2}(x_3 - \delta\ell t)^2)}{(1+t^2)^{3/2}} \right) ds \\ &+ \frac{1}{\delta^2\ell^2}\int_{\frac{a}{\delta}}^{\frac{b}{\delta}} \left(\frac{\delta\ell t(p_{0,3} + p_{1,3}(x_3 - \delta\ell t) + p_{2,3}(x_3 - \delta\ell t)^2)}{(1+t^2)^{3/2}} \right) ds \end{aligned}$$

We note that there are no cross-terms on the left hand side, which means

$$p_{1,1} = p_{2,1} = p_{1,2} = p_{2,2} = 0$$

Thus our problem simplifies to

$$\begin{aligned} -B_1x_1 - B_2x_2 - B_3x_3 &= \frac{1}{\delta^2\ell^2}\int_{\frac{a}{\delta}}^{\frac{b}{\delta}} \left(\frac{x_1p_{0,1} + x_2p_{0,2}}{(1+t^2)^{3/2}} \right) ds \\ &+ \frac{1}{\delta\ell}\int_{\frac{a}{\delta}}^{\frac{b}{\delta}} \left(\frac{t(p_{0,3} + p_{1,3}(x_3 - \delta\ell t) + p_{2,3}(x_3 - \delta\ell t)^2)}{(1+t^2)^{3/2}} \right) ds \end{aligned}$$

We require the asymptotics of the follow integrals

$$\begin{aligned}
I_0 &= \frac{1}{\delta^2\ell^2}\int_{a/\delta}^{b/\delta}\frac{1}{(1+t^2)^{3/2}}dt \sim \frac{2}{r^2} - \frac{\ell^2+x_3^2}{(\ell^2-x_3^2)^2} + O\left(\delta^2\right) \\
I_1 &= \frac{1}{\delta\ell}\int_{a/\delta}^{b/\delta}\frac{t}{(1+t^2)^{3/2}}dt \sim \frac{2x_3}{\ell^2-x_3^2} + O(\delta^2) \\
I_2 &= \int_{a/\delta}^{b/\delta}\frac{t^2}{(1+t^2)^{3/2}}dt \sim 2log\left(\frac{2}{\delta}\right) - 2 + 2log\left(\sqrt{1-\frac{x_3^2}{\ell^2}}\right) + O(\delta^2) \\
I_3 &= \delta\ell\int_{a/\delta}^{b/\delta}\frac{t^3}{(1+t^2)^{3/2}}dt \sim 2x_3 + O(\delta^2)
\end{aligned}$$

We substitute these integrals into our matching problem to obtain

$$\begin{aligned}
C_2 - B_1x_1 - B_2x_2 - B_3x_3 &= x_1p_{0,1}I_0 + x_2p_{0,2}I_0 + (p_{0,3} + x_3p_{1,3} + x_3^2p_{2,3})I_1 \\
&\quad -(p_{1,3} + 2x_3p_{2,3})I_2 + p_{2,3}I_3
\end{aligned}$$

The matching condition to leading order for each strength polynomial then requires

$$\begin{aligned}
g_1(s) &= -B_1\left(\frac{r^2}{2}\right) \\
g_2(s) &= -B_2\left(\frac{r^2}{2}\right) \\
g_3(s) &= -B_3\frac{\epsilon}{4}\left(\ell^2 - s^2\right)
\end{aligned}$$

where the slenderness parameter is given by $\epsilon = \left[\log\left(\frac{2}{\delta}\right)\right]^{-1}$. Noting that $\frac{r^2}{2} << \frac{\epsilon}{4}$, we can express the dipole strength distribution as $\boldsymbol{\gamma}(s) = -B_3\frac{\epsilon}{4}(0, 0, \ell^2 - s^2)$. We recover the field outside the body via the relationship

$$\mathbf{B} = \nabla\Phi_M = \mathbf{B_0} + \nabla\left(\int_{-\ell}^{\ell}\Phi_D(\mathbf{x} - \mathbf{x}_s; \boldsymbol{\gamma}(s))ds\right)$$

For example, in Figure 2.1, I have set $\epsilon = 0.1$ which comparable to experimental parameters. The figure shows good qualitative agreement with our expectations.

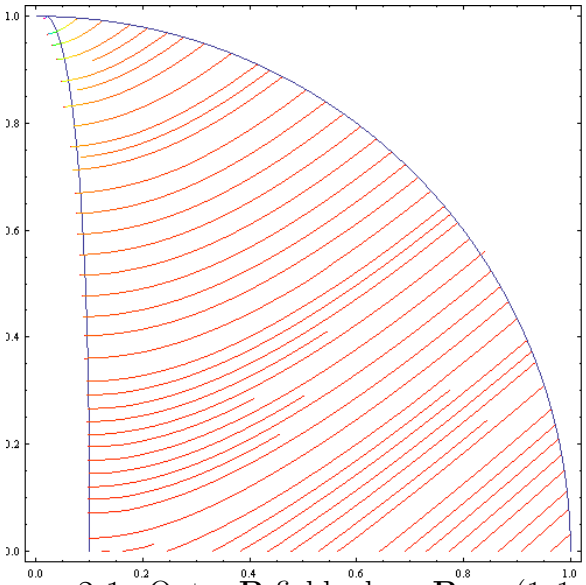

FIGURE 2.1. Outer $\mathbf{B}$ field where $\mathbf{B_0} = (1, 1, 1)$.

2.3. Torque balance and uniqueness in free space

Next, we wish to consider the coupled magnetic-hydrodynamic problem of a straight rod sweeping an upright double-cone in free space. Recall that the fluid torque about the origin for a slender body with chord angle κ is given by

$$\mathbf{T}_F(0) = 8\pi\mu \int_{-\ell}^{\ell} \mathbf{x}_s \times \boldsymbol{\alpha}(s) ds$$

where $\mathbf{x}_s = (s\sin\kappa, 0, s\cos\kappa)$ is the position of the singularities long the center-line of the rod, $\boldsymbol{\alpha} = \frac{\omega\epsilon}{2}\sin\kappa(0, s, 0)$ where ω is the angular speed of the rod, and $\epsilon = \left[\log\left(\frac{2}{\delta}\right)\right]^{-1}$ is our slenderness parameter. In the straight rod geometry, the calculation of the fluid torque is straightforward and gives

$$\begin{aligned} T_F^1 &= \frac{8}{3}\epsilon\ell^3\pi\omega\mu\sin\kappa\cos\kappa \\ T_F^2 &= 0 \\ T_F^3 &= -\frac{8}{3}\epsilon\ell^3\pi\omega\mu\sin^2\kappa \end{aligned}$$

For a uniform background field expressed as $\mathbf{B_0} = B(\sin\theta\cos\phi, \sin\theta\sin\phi, \cos\theta)$ where θ is the angle between the field line and the positive z-axis and ϕ is the azimuthal

angle. In this problem, we assume that initial transients have been cleared and we can treat this as a static problem where both the rod and magnetic field rotate with angular speed ω. This allows us to view the rod in body coordinates as always lying in the yz-plane. The magnetic field lines will then have a positive azimuthal angle ϕ ,which we call the lag angle, since the reactive force of the fluid on the rod will act to impede the motion of the rod. Solutions to the torque balance equation will then be given as the three angles (κ, β, ϕ) which will fully describe the position of the rod relative to the constantly rotating magnetic field. The magnetic torque can be represented as an integral over the surface of the rod using the formula from Jackson [**10**]

$$\mathbf{T}_M = \int_{\partial\Omega} \mathbf{x} \times \mathbf{B} dS$$

and we may transform this surface integral to an integral over the volume of the rod by

$$\begin{aligned} \mathbf{T}_M^i &= \int_\Omega (\nabla \cdot \mathbf{B_0})(\mathbf{x} \times \mathbf{B_0})_i dV \text{ where} \\ \nabla \cdot \mathbf{B_0} &= \int_{-\ell}^{\ell} \boldsymbol{\gamma}(s) \cdot \nabla \delta(\mathbf{x} - \mathbf{y}) ds \end{aligned}$$

using the properties of the delta function, we may tranform this expression to a line integral which gives the following expression for the magnetic torque

$$\mathbf{T}_M = 4\pi\mu_0 \int_{-\ell}^{\ell} \boldsymbol{\gamma}(s) \times \mathbf{B_0} ds$$

given more conveniently in component form as

$$\begin{aligned} T_M^1 &= 4\pi\mu_0 \int_{-\ell}^{\ell} \gamma_2 B_3 - \gamma_3 B_2 ds \\ T_M^2 &= 4\pi\mu_0 \int_{-\ell}^{\ell} \gamma_3 B_1 - \gamma_1 B_3 ds \\ T_M^3 &= 4\pi\mu_0 \int_{-\ell}^{\ell} \gamma_1 B_2 - \gamma_2 B_1 ds \end{aligned}$$

From here we must consider our generator solution, which prescribes the dipole strength distribution for in any rod orientation by replacing B_3 with the projection of the magnetic field onto the center-line of the rod. In this case with the background field described above, the scalar projection of the initial background field $\mathbf{B_0}$ onto the center-line of the rod is given by

$$B_\tau = \mathbf{B_0} \cdot (\sin\kappa, 0, \cos\kappa) = B(\sin\kappa\sin\theta\cos\phi + \cos\kappa\cos\theta)$$

and the dipole strength distribution is $\boldsymbol{\gamma}(s) = B_\tau(\ell^2 - s^2)(\sin\kappa, 0, \cos\kappa)$. The argument in the integrals above are

$$\begin{aligned}
\gamma_2 B_3 - \gamma_3 B_2 &= -(\ell^2 - s^2)BB_\tau \cos\kappa \sin\theta \sin\phi \\
\gamma_3 B_1 - \gamma_1 B_3 &= (\ell^2 - s^2)BB_\tau(\cos\kappa\sin\theta\cos\phi - \sin\kappa\cos\theta) \\
\gamma_1 B_2 - \gamma_2 B_1 &= (\ell^2 - s^2)BB_\tau \sin\kappa \sin\theta \sin\phi
\end{aligned}$$

Remembering the magnetic field constant $4\pi\mu_0$, the magnetic torque can be expressed as

$$\begin{aligned}
T_M^1 &= -\frac{8}{3}\epsilon\ell^3 B^2 \pi\mu_0 \cos\kappa \sin\theta \sin\phi(\sin\kappa\sin\theta\cos\phi + \cos\kappa\cos\theta) \\
T_M^2 &= \frac{8}{3}\epsilon\ell^3 B^2 \pi\mu_0(\cos\kappa\sin\theta\cos\phi - \sin\kappa\cos\theta)(\sin\kappa\sin\theta\cos\phi + \cos\kappa\cos\theta) \\
T_M^3 &= \frac{8}{3}\epsilon\ell^3 B^2 \pi\mu_0 \sin\kappa \sin\theta \sin\phi(\sin\kappa\sin\theta\cos\phi + \cos\kappa\cos\theta)
\end{aligned}$$

We may now plot the components of the magnetic torque as a function of any of these parameters holding the others fixed. In particular, we may first examine the magnetic torque by letting $\kappa = \frac{\pi}{3},\ \epsilon = 0.3,\ \ell = 1,\ B = 1,\ \mu_0 = 1.2566 \times 10^{-6}$ for various values of θ with $0 \leq \phi \leq 2\pi$. The component T_M^1 is presented in red, T_M^2 in green, and T_M^3 in blue. Figures 2.2- 2.5 show these results.

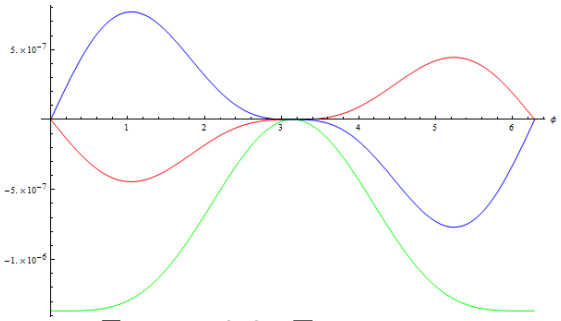

FIGURE 2.2. Torque components for $\theta = \pi/6$

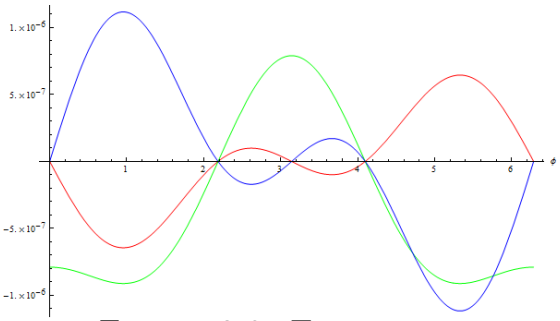

FIGURE 2.3. Torque components for $\theta = \pi/4$

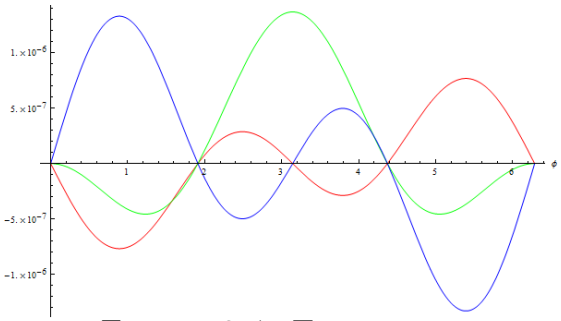

FIGURE 2.4. Torque components for $\theta = \pi/3$

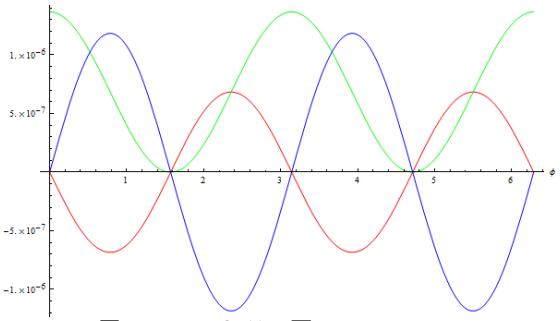

FIGURE 2.5. Torque components for $\theta = \pi/2$

We may repeat this procedure for various values of ϕ with $0 \leq \theta \leq 2\pi$, shown in Figures 2.6- 2.9. It is interesting to note that the torque does not appear to be as sensitive to changes in the azimuthal angle ϕ as it does to changes in the angle θ.

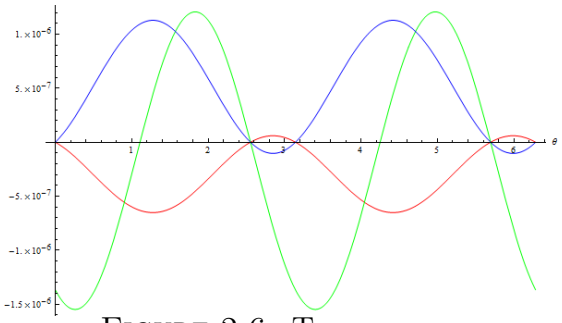

FIGURE 2.6. Torque components for $\phi = \pi/6$

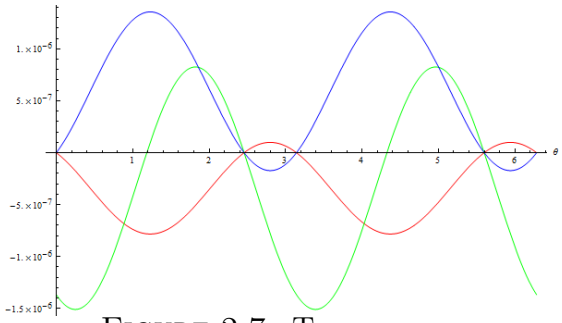

FIGURE 2.7. Torque components for $\phi = \pi/4$

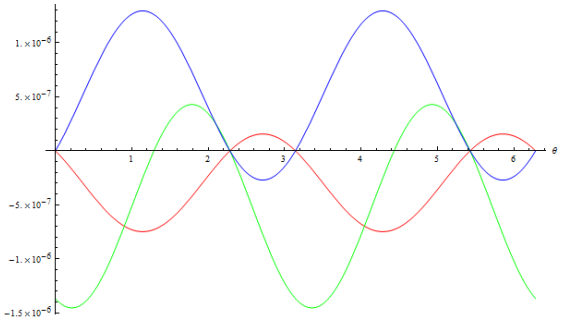

FIGURE 2.8. Torque components for $\phi = \pi/3$

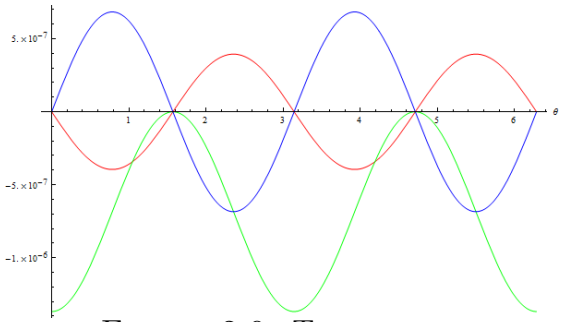

FIGURE 2.9. Torque components for $\phi = \pi/2$

Now that we have both the fluid and magnetic torques about the origin for a given angular speed ω, we may construct a torque balance which will yield equations to find the angles κ and β which describe the position of the rod. The torque balance is stated simply as $\mathbf{T} = \mathbf{T}_F + \mathbf{T}_M = \mathbf{0}$ assuming the origin is the point around which the torques are found. We seek to non-dimensionalize the torque balance by utilizing the parameter

$$\lambda = \frac{(\omega\mu)^2}{(B^2\mu_0)^2}$$

We can check the dimensionality of this parameter, by noting

$$\sqrt{\lambda} \approx \frac{1}{T}\frac{NT}{L^2}\frac{A^2}{N^2}\frac{NL^2}{A^2} = 1$$

The given parameters in this model are (B, θ, ω), and the parameters to be solved for are the lag angle ϕ and the cone angle κ. By considering each component of the

torque equation, we have

$$\begin{aligned} 0 &= \cos\kappa \sin\theta \cos\phi - \sin\kappa \cos\theta \\ \sqrt{\lambda} \sin\kappa \cos\kappa &= -\cos\kappa \sin\theta \sin\phi (\sin\kappa \sin\theta \cos\phi + \cos\kappa \cos\theta) \end{aligned}$$

which reduces to the following system

$$\begin{aligned} \tan\kappa &= \frac{\sin\theta\cos\theta\sin\phi}{\sqrt{\lambda} - \sin^2\theta\sin\phi\cos\phi} \\ \tan\kappa &= \tan\theta\cos\phi \end{aligned}$$

Setting the right hand sides of the above equations equal and then rearranging, we come up with a polynomial which is cubic in $\tan\phi$:

$$\cos^2\theta\tan^3\phi - \sqrt{\lambda}\tan^2\phi + \tan\phi - \sqrt{\lambda} = 0$$

Letting $T = \tan\phi$, the polynomial becomes

$$f(T) = \cos^2\theta T^3 - \sqrt{\lambda}T^2 + T - \sqrt{\lambda} = 0$$

From this equation, we wish to solve for $\tan\phi$ which can then be substituted to find the cone angle κ. Given the parameters (B, θ, ω) it is not difficult to numerically solve this equation. We should however show that the solution is unique, which is reduced to showing that this cubic polynomial has one real root. To show this, we note that the discriminant of the cubic equation $ax^3 + bx^2 + cx + d = 0$ is a quantity given by

$$\Delta = 18abcd - 4b^3d + b^2c^2 - 4ac^3 - 27a^2d^2$$

We have the following conditions depending on the sign of Δ:

if $\Delta < 0$, then $f(T)$ has one real root and two complex conjugate roots

if $\Delta = 0$, then $f(T)$ has multiple roots which are all real

if $\Delta > 0$, then $f(T)$ has three distinct real roots

For our polynomial above, this expression reduces to the following:

$$\Delta = -27\lambda\cos^4\theta + (18\lambda - 4)\cos^2\theta + (\lambda - 4\lambda^2)$$

To examine where Δ is greater than zero, we must look at the discriminant of the discriminant to find the zeros of Δ. The more familiar discriminant of a quadratic polynomial $ax^2 + bx + c = 0$ is given by $b^2 - 4ac$. Thus the next quantity of interest is given by:

$$\Delta_\Delta = -16(3\lambda - 1)^3$$

We can also state that

$$\begin{aligned}
&\text{if } \Delta_\Delta < 0, \text{ then } \Delta \text{ has two distinct complex conjugate roots} \\
&\text{if } \Delta_\Delta = 0, \text{ then } \Delta \text{ has one real root of multiplicity two} \\
&\text{if } \Delta_\Delta > 0, \text{ then } \Delta \text{ has two distinct real roots}
\end{aligned}$$

If $\Delta_\Delta < 0$, then Δ has no real roots, and as such we always have that $\Delta < 0$ which implies that there is a unique solution to our equation $f(T)$. In this case, it is easy to find such a condition for λ:

$$\lambda > \frac{1}{3}$$

Instead assume $\Delta_\Delta > 0$ so that we can find two real roots for Δ:

$$\begin{aligned}
r_+ &= \frac{-2 + 2(1 - 3\lambda)^{3/2} + 9\lambda}{27\lambda} \\
r_- &= \frac{-2 - 2(1 - 3\lambda)^{3/2} + 9\lambda}{27\lambda}
\end{aligned}$$

For $\lambda < \frac{1}{3}$, these roots are surely real, but we must remember that these are roots of Δ, which is quadratic in $\cos^2\theta$. We note that if $r_- < 0$, this root is not allowable as

$0 < \cos^2\theta < 1$.

$$\begin{aligned} r_- &< 0 \\ \frac{-2 - 2(1-3\lambda)^{3/2} + 9\lambda}{27\lambda} &< 0 \\ 9\lambda - 2 &< 2(1-3\lambda)^{3/2} \\ 4 - 36\lambda + 81\lambda^2 &< 4 - 36\lambda + 108\lambda^2 - 108\lambda^3 \\ \lambda &< \frac{1}{4} \end{aligned}$$

The roots converge at $\lambda = \frac{1}{3}$ to $r_\pm = \frac{1}{9}$ which corresponds to an angle $\theta \approx 70.53$ degrees To summarize

$$\begin{aligned} &\text{for } \lambda > \frac{1}{3},\ f(T) \text{ has a unique real solution} \\ &\text{for } \lambda \in (\frac{1}{4}, \frac{1}{3}),\ \Delta \text{ has two real roots over } 0 < \theta < \frac{\pi}{2} \\ &\text{for } \lambda < \frac{1}{4},\ \Delta \text{ has one real root over } 0 < \theta < \frac{\pi}{2} \end{aligned}$$

Another way of looking at this would be to view Δ as a quadratic polynomial in λ:

$$\Delta = -4\lambda^2 + \lambda(1 + 18\cos^2\theta - 27\cos^4\theta) - 4\cos^2\theta$$

In this case, we find that

$$\Delta_\Delta = 1 - 28\cos^2\theta + 270\cos^4\theta - 972\cos^6\theta + 729\cos^8\theta$$

We can find the zero of Δ_Δ by plotting this function for $\theta \in (0, \frac{\pi}{2})$. This value is $\theta \approx 70.53^o$. So for $\theta < 70.53^o$, $\Delta_\Delta < 0$ and thus Δ has no real roots. This implies that $\Delta < 0$ and we have a unique solution to $f(T)$. It should be noted that this uniqueness for $\theta < 70.53$ is independent of choice of λ. Now that we have information on the uniqueness of our solution, we can specify a value of θ and investigate the solution for various limits of λ. In the last section, we showed that the solution to $f(T)$ is unique for all λ when $\theta < 70.53^o$. For the purpose of the following calculations, I let

$\theta = \frac{\pi}{4}$ so that we are guaranteed a unique solution. The equation $f(T) = 0$ can then be solved numerically to find $\tan\phi$. This in turn can be used to find the cone angle κ. Before we solve this equation numerically, we can write out the real solution to $f(T) = 0$ for our choice of θ.

$$\begin{aligned}\tan\phi &= \frac{2}{3}\sqrt{\lambda} - \frac{6 - 4\lambda}{3(9\sqrt{\lambda} + 8\lambda^{3/2} + \sqrt{216 - 351\lambda + 432\lambda^2})^{1/3}} \\ &\quad + \frac{1}{3}(9\sqrt{\lambda} + 8\lambda^{3/2} + \sqrt{216 - 351\lambda + 432\lambda^2})^{1/3}\end{aligned}$$

Table 2.1 shows the values of κ and ϕ for various values of λ presented in degrees where $\theta = \frac{\pi}{4} = 45°$.

λ	0.01	0.1	1	10	100	1000
κ	44.86	43.50	28.53	9.09	2.87	0.91
ϕ	5.74	18.41	57.06	80.79	87.13	89.09

Table 2.1: Cone and lag angles for increasing λ.

For a general angle θ, the expression for $\tan\phi$ is lengthy, but we can report several asymptotic limits for the solution.

$$\begin{aligned}\tan\phi &\sim \sqrt{\lambda} + O\left(\lambda^{3/2}\right),\ \lambda \to 0 \\ \tan\phi &\sim \frac{\sqrt{\lambda}}{\cos^2\theta} + O\left(\frac{1}{\sqrt{\lambda}}\right),\ \lambda \to \infty \\ \tan\phi &\sim \frac{1}{3}\left(\frac{\lambda - 3}{\sqrt[3]{\lambda^{3/2} + 9\sqrt{\lambda} + 3\sqrt{3}\sqrt{(\lambda+1)^2}}} + \sqrt[3]{\lambda^{3/2} + 9\sqrt{\lambda} + 3\sqrt{3}\sqrt{(\lambda+1)^2}}\right. \\ &\quad \left. + \sqrt{\lambda}\right) + O\left(\lambda^{3/2}\right),\ \theta \to 0 \\ \tan\phi &\sim \frac{\sqrt{\lambda}}{\left(\theta - \frac{\pi}{2}\right)^2} + O\left(1\right),\ \theta \to \frac{\pi}{2}\end{aligned}$$

We may then find the solution for the chord angle κ and lag angle ϕ to leading order in these asymptotic limits of λ recalling that $\tan\kappa = \tan\theta\cos\phi$.

$$\begin{aligned}(\kappa,\phi) &\sim \left(\theta, \sqrt{\lambda}\right),\ \lambda \to 0\\ (\kappa,\phi) &\sim \left(0, \frac{\pi}{2}\right),\ \lambda \to \infty\end{aligned}$$

In investigating these limits, it is a good idea to remember that

$$\lambda = \frac{(\omega\mu)^2}{(E^2\epsilon_0)^2}$$

so that λ represents a balance between the angular speed and the magnetic field strength. Thus the limit $\lambda \to 0$ can be interpreted either as the case where the magnetic field strength is very large and dominates the angular speed or the case where the angular speed goes to zero. In either case, we expect that the cone angle κ would approach the field angle θ and the lag angle ϕ between the rod and the field would go to zero. Examination of the Table 2.1 shows this phenomenon. The limit where $\lambda \to \infty$ could be interpreted either as the case where ω is very large and dominates B or the case where B goes to zero. In either case, we expect that we happen upon a state where the rotation rate is so fast that the cone angle decreases to zero.

2.4. Torque balance for a rod above a no-slip plane

2.4.1. Straight rod geometry. We now turn to the problem of a slender soft-magnetic rod sweeping a cone above a no-slip plane. For a straight rod, the fluid torque may be represented by the same formula as the previous sections with only the limits of integration and the slenderness parameter changed

$$\mathbf{T}_F(0) = 8\pi\mu \int_0^\ell \mathbf{x}_s \times \boldsymbol{\alpha}(s) ds$$

where $\mathbf{x}_s = (s\sin\kappa, 0, s\cos\kappa)$ is the position of the singularities long the centerline of the rod, $\boldsymbol{\alpha} = \frac{\omega\epsilon}{2}\sin\kappa(0, s, 0)$ where ω is the angular speed of the rod, and

$\epsilon = \left[\log\left(\frac{1}{\delta}\right)\right]^{-1}$ is our slenderness parameter. In this case, the fluid torque has components

$$\begin{aligned} T_F^1 &= \frac{4}{3}\epsilon\ell^3\pi\omega\mu\sin\kappa\cos\kappa \\ T_F^2 &= 0 \\ T_F^3 &= -\frac{4}{3}\epsilon\ell^3\pi\omega\mu\sin^2\kappa \end{aligned}$$

The beauty of the full Blakeslet solution lies in the fact that the fluid torque can be represented by the same expression as the case of a rod in free space. This is true because the image singularities lie below the plane, thus they do not contribute to the integrals in the derivation of the fluid torque. A detailed justification may be found in Chwang and Wu [**7**].

When considering the magnetic torque, the strength distribution of the dipole singularities must change since our limits of integration have changed. In this case, our generator solution will dictate that we use the following strength distribution

$$\boldsymbol{\gamma}(s) = -B_3\epsilon(0, 0, s(\ell - s))$$

Together with the formula

$$\mathbf{T}_M = 4\pi\mu_0\int_0^\ell \boldsymbol{\gamma}(s)\times\mathbf{B_0}ds$$

in which case we have the following expression for the components of the magnetic torques

$$\begin{aligned} T_M^1 &= -\frac{4}{3}\epsilon\ell^3B^2\pi\mu_0\cos\kappa\sin\theta\sin\phi(\sin\kappa\sin\theta\cos\phi+\cos\kappa\cos\theta) \\ T_M^2 &= \frac{4}{3}\epsilon\ell^3B^2\pi\mu_0(\cos\kappa\sin\theta\cos\phi-\sin\kappa\cos\theta)(\sin\kappa\sin\theta\cos\phi+\cos\kappa\cos\theta) \\ T_M^3 &= \frac{4}{3}\epsilon\ell^3B^2\pi\mu_0\sin\kappa\sin\theta\sin\phi(\sin\kappa\sin\theta\cos\phi+\cos\kappa\cos\theta) \end{aligned}$$

The particular choice we made in our dipole strength distribution allows us to recover the same equations for the torque balance as in the previous section.

2.4.2. Bent rod geometry. Recall from Chapter 1 that the center-line for our bent rod geometry is described by

$$\begin{aligned} x_s &= -2a\cos\beta\cos\kappa\sin\left(\frac{\ell-s}{2a}\right)\sin\left(\frac{s}{2a}\right)+2a\sin\kappa\cos\left(\frac{\ell-s}{2a}\right)\sin\left(\frac{s}{2a}\right) \\ y_s &= -2a\sin\beta\sin\left(\frac{\ell-s}{2a}\right)\sin\left(\frac{s}{2a}\right) \\ z_s &= 2a\cos\kappa\cos\left(\frac{\ell-s}{2a}\right)\sin\left(\frac{s}{2a}\right)+2a\cos\beta\sin\kappa\sin\left(\frac{\ell-s}{2a}\right)\sin\left(\frac{s}{2a}\right) \end{aligned}$$

for $0 \leq s \leq \ell$ where $K = \frac{1}{a}$ is the local non-dimensional curvature of the body center-line with respect to the body length. The Stokeslet strength in the Blakeslet is then given by

$$\boldsymbol{\alpha} = Rdiag(\frac{\epsilon}{4}, \frac{\epsilon}{2}, \frac{\epsilon}{2})R^{-1}\mathbf{U}$$

where $\mathbf{U} = \boldsymbol{\omega}\times\mathbf{x}_s$ and $R = (\mathbf{e}_\tau, \mathbf{e}_\eta, \mathbf{e}_\beta)$, where $\mathbf{e}_\tau = \frac{\partial \mathbf{x}_s}{\partial s}$, $\mathbf{e}_\eta = \frac{1}{K}\frac{\partial^2 \mathbf{x}_s}{\partial s^2}$, and $\mathbf{e}_\beta = \mathbf{e}_\tau \times \mathbf{e}_\eta$. The magnetic strength distribution may be described in an analogous manner as

$$\boldsymbol{\gamma} = Rdiag(-\frac{\epsilon}{4}, 0, 0)R^{-1}\mathbf{B_0}$$

and the magnetic torque is given by

$$\mathbf{T}_M = 4\pi\mu_0 \int_0^\ell 4s(\ell - s)\left(\boldsymbol{\gamma}(s)\times\mathbf{B_0}\right) ds$$

The expressions in this case are much more complicated than those in the straight rod geometry. For example, the components of the Stokeslet strength distribution are

$$\begin{aligned}
\alpha_1 = \frac{1}{8}a\omega\epsilon\sin(\beta)\sin\left(\frac{s}{2a}\right)\Bigg(2\sin\left(\frac{s}{2a}\right)\Bigg(\sin\left(\frac{L}{2a}\right)\Bigg(\cos(\beta)\sin(2\kappa)\cos\left(\frac{s}{a}\right) \\
-\sin^2(\kappa)\sin\left(\frac{s}{a}\right)+\cos^2(\kappa)\sin\left(\frac{s}{a}\right)\Bigg)+\cos\left(\frac{L}{2a}\right)\Bigg(\cos(2\kappa)\cos\left(\frac{s}{a}\right) \\
-2\cos(\beta)\sin(\kappa)\cos(\kappa)\sin\left(\frac{s}{a}\right)\Bigg)\Bigg)+\sin\left(\frac{L-3s}{2a}\right)+7\sin\left(\frac{L-s}{2a}\right)\Bigg) \\
\alpha_2 = \frac{1}{4}a\omega\epsilon\sin\left(\frac{s}{2a}\right)\Bigg(-\Bigg(\sin^2(\beta)\Bigg(\cos\left(\frac{L-2s}{a}\right)+3\Bigg)+4\cos^2(\beta)\Bigg) \\
\cdot\Bigg(\cos(\beta)\cos(\kappa)\sin\left(\frac{L-s}{2a}\right)-\sin(\kappa)\cos\left(\frac{L-s}{2a}\right)\Bigg) \\
-2\sin^2(\beta)\sin\left(\frac{L-2s}{2a}\right)\sin\left(\frac{L-s}{2a}\right)\Bigg(\cos\left(\frac{s}{a}\right)\Bigg(\cos(\beta)\cos(\kappa)\sin\left(\frac{L}{2a}\right) \\
-\sin(\kappa)\cos\left(\frac{L}{2a}\right)\Bigg)-\sin\left(\frac{s}{a}\right)\Bigg(\cos(\beta)\cos(\kappa)\cos\left(\frac{L}{2a}\right)+\sin(\kappa)\sin\left(\frac{L}{2a}\right)\Bigg)\Bigg)\Bigg) \\
\alpha_3 = -\frac{1}{2}a\omega\epsilon\sin(\beta)\sin(\kappa)\sin^2\left(\frac{s}{2a}\right)\Bigg(\sin\left(\frac{L}{2a}\right)\Bigg(\cos(\beta)\sin(\kappa)\cos\left(\frac{s}{a}\right) \\
+\cos(\kappa)\sin\left(\frac{s}{a}\right)\Bigg)+\cos\left(\frac{L}{2a}\right)\Bigg(\cos(\kappa)\cos\left(\frac{s}{a}\right)-\cos(\beta)\sin(\kappa)\sin\left(\frac{s}{a}\right)\Bigg)\Bigg)
\end{aligned}$$

As an alternative to reporting the lengthy expressions for the dipole strength distribution, I instead present Figures 2.10- 2.13 which show its individual components. For all plots, γ_1 is shown in red, γ_2 in green, and γ_3 in blue.

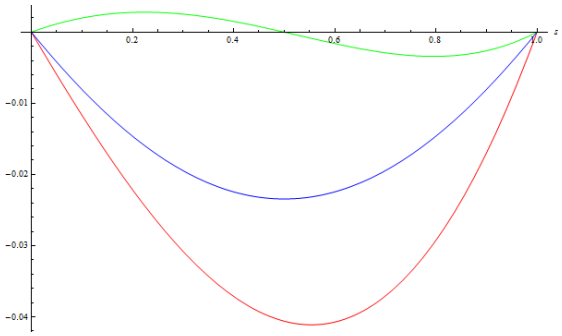

FIGURE 2.10. Strength components for $\kappa = \frac{\pi}{3},\ \beta = \frac{\pi}{3},\ \phi = \frac{\pi}{3},\ \theta = \frac{\pi}{3}$

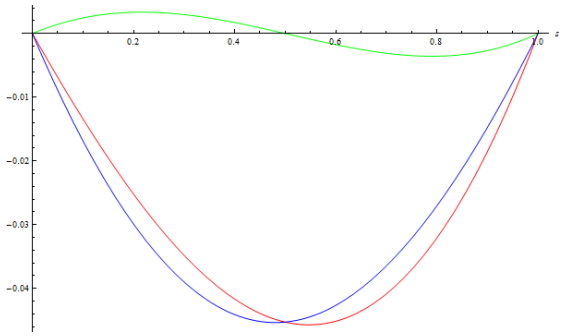

FIGURE 2.11. Strength components for $\kappa = \frac{\pi}{4},\ \beta = \frac{\pi}{4},\ \phi = \frac{\pi}{4},\ \theta = \frac{\pi}{4}$

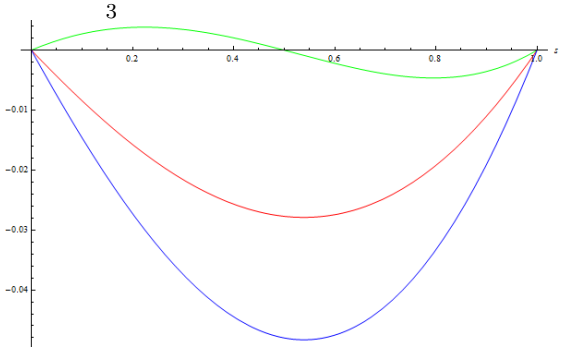

FIGURE 2.12. Strength components for $\kappa = \frac{\pi}{6},\ \beta = \frac{\pi}{2},\ \phi = \frac{\pi}{4},\ \theta = \frac{\pi}{3}$

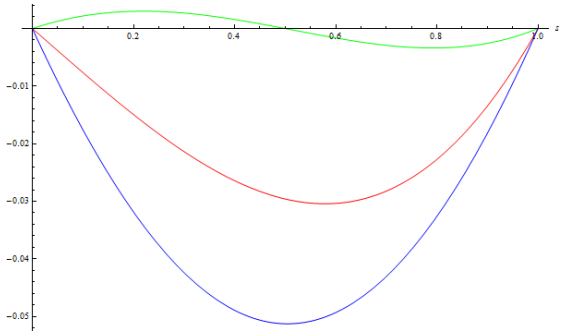

FIGURE 2.13. Strength components for $\kappa = \frac{\pi}{6},\ \beta = -\frac{\pi}{4},\ \phi = \frac{\pi}{3},\ \theta = \frac{\pi}{4}$

Complicated analytical expressions aside, we may still use the fluid and magnetic singularity distributions to find a torque balance $\mathbf{T} = \mathbf{T}_F + \mathbf{T}_M = 0$. Solutions to the torque balance will now be represented by three angles (κ, β, ϕ) where β is the scooping angle. In this case, the question of uniqueness of solutions is still of interest, but the complicated nature of the torque balance equations do not yield a system as with the torque balance in the straight rod geometry. We may however assume

regular expansions of the relevant angles in a small parameter Δ as follows

$$\begin{aligned}
\kappa &= \kappa_0 + \Delta\kappa_1 + \Delta^2\kappa_2 + \dots \\
\beta &= \beta_0 + \Delta\beta_1 + \Delta^2\beta_2 + \dots \\
\phi &= \phi_0 + \Delta\phi_1 + \Delta^2\phi_2 + \dots
\end{aligned}$$

Inserting these expansions into the torque balance yields a system for the first order solution

$$\begin{aligned}
T_1 &= -\frac{1}{12}\ell^3\epsilon(\omega\mu\sin(2\kappa_0) - B^2\mu_0\cos\kappa_0\sin\phi_0(\cos\kappa_0\sin(2\theta) + 2\sin\kappa_0\sin^2\theta\cos\phi_0)) \\
T_2 &= -\frac{1}{6}B^2\mu_0\ell^3\epsilon(\cos\kappa_0\sin\theta\cos\phi_0 - \sin\kappa_0\cos\theta)(\cos\kappa_0\cos\theta + \sin\kappa_0\sin\theta\cos\phi_0) \\
T_3 &= -\frac{1}{12}\ell^3\epsilon\sin\kappa_0(B^2\mu_0\cos\kappa_0\sin(2\theta)\sin\phi_0 + \sin\kappa_0(-2\omega\mu + B^2\mu_0\sin^2\theta\sin(2\phi_0))) \\
T_1 &= T_2 = T_3 = 0
\end{aligned}$$

We notice that the scooping angle β does not enter the torque balance at the leading order. This system reduces to

$$\begin{aligned}
\tan\kappa_0 &= \tan\theta\cos\phi_0 \\
\tan\kappa_0 &= \frac{\sin(2\theta)\sin\phi_0}{2\sqrt{\lambda} - \sin^2\theta\sin(2\phi_0)}
\end{aligned}$$

which we can solve in a similar fashion as the system in the straight rod case. Higher order terms in the series for the torque components can be obtained, allowing us to compute correction terms. We consider a numerical example with $\ell = 1,\ \epsilon = 0.3,\ \theta = \frac{\pi}{6},\ B^2\mu_0 = 1,\ \omega\mu = 1$. The first order torque balance yields the following solution for κ_0 and ϕ_0 in radians.

$$\begin{aligned}
\kappa_0 &= 0.359089 = 20.57^\circ \\
\phi_0 &= 0.863018 = 49.45^\circ
\end{aligned}$$

The first correction terms to these angles κ_1 and ϕ_1, along with the leading order term for the scooping angle β can then be determined numerically as

$$\begin{aligned}\kappa_1 &= -0.032425 = -1.86^\circ \\ \phi_1 &= -0.543755 = -31.15^\circ \\ \beta_0 &= 1.5708 = 90^\circ\end{aligned}$$

2.4.3. A straight rod in a linear background magnetic field. This slender body theory can be extended for any linearization of a general field. Setting aside the constant piece we would obtain from such an expression since it would be covered by the theory of the previous sections, we can examine a linear field of the form $\mathbf{B_0} = A(\mathbf{x} - \mathbf{x_0}) = A\mathbf{x}$ where the linearization point $\mathbf{x_0}$ is taken as the origin and A is of the form

$$A = \begin{pmatrix} a_{11} & a_{12} & a_{13} \\ a_{12} & a_{22} & a_{23} \\ a_{13} & a_{23} & -(a_{11}+a_{22}) \end{pmatrix}$$

Thus our initial potential is given as $\phi_0 = \frac{1}{2}\mathbf{x}^T A\mathbf{x}$. In this case we assume a general cubic strength distribution $\boldsymbol{\gamma}_L = (g_1^L(s), g_2^L(s), g_L^3(s))$ where

$$g_i^L(s) = g_{0,i} + g_{1,i}s + g_{2,i}s^2 + g_{3,i}s^3,\ i = 1,2,3$$

If we further assume that A is given by $A = diag(a_{11}, a_{22}, -(a_{11}+a_{22}))$ our initial potential is given by

$$\phi_0 = \frac{1}{2}\left(a_{11}x_1^2 + a_{22}x_2^2 - (a_{11}+a_{22})x_3^2\right)$$

The same matching procedure is carried out as in the previous section to obtain

$$\boldsymbol{\gamma}(s) \sim -\frac{\epsilon}{6(a_{11}+a_{22})}(0,0,s(\ell^2 - s^2)) + O(r^2)$$

where again $\epsilon = \left[\log\left(\frac{\ell}{r}\right)\right]^{-1}$. The outer field is then recovered by taking the gradient of the total potential as defined before

$$\mathbf{B} = \nabla\Phi_M = \mathbf{B_0} + \nabla\left(\int_0^\ell \Phi_D(\mathbf{x} - \mathbf{x}_s; \boldsymbol{\gamma}_L(s))ds\right)$$

We can present an example of the external field if $A = diag(1, 1, -2)$ in Figure 2.14.

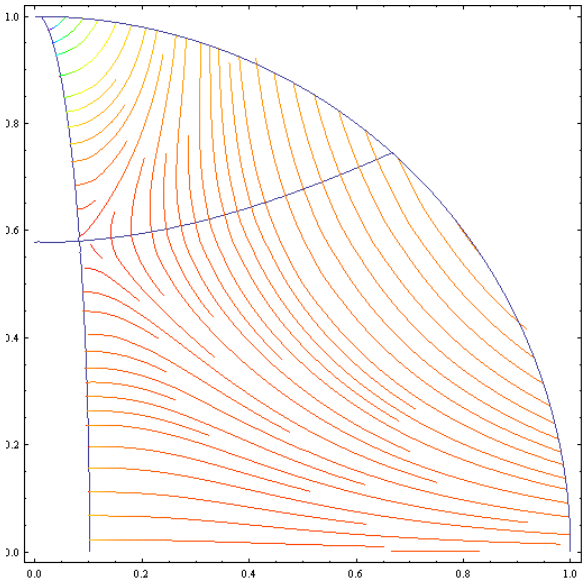

FIGURE 2.14. Outer $\mathbf{B}$ field where $A = diag(1, 1, -2)$.

2.5. Summary

I believe this magnetic slender body theory has the potential to find applications in a variety of ciliary and flagellar experiments which use magnetic drivers, from nodal ciliary models to models of low Reynolds number swimmers. One limiting factor is that the theory relies on a small curvature assumption in the bent rod geometry in order to neglect the dipole-dipole interactions that would be otherwise significant for large curvature.

CHAPTER 3

Lagrangian experiments for a rod sweeping a cone over a no-slip plane

The study of the fluid flow structure induced by a single nodal cilia in the Stokes regime is important problem in fluid dynamics. Such a study may lead to new insights regarding ciliated systems, and new work on the subject of left-right symmetry breaking for mouse embryos has shown that this phenomenon is possible with only two cilia in the nodal cavity [**14**]. A review of this left-right symmetry breaking can be found in Hamada [**8**]. Some studies have considered this problem from a theoretical fluid dynamics perspective taking into account large-scale flow structures produced from many cilia in the node [**15**]. However, there had been little work in regards to attacking the problem of the fluid structures created by a rotating model nodal cilia from a Lagrangian perspective until the work of Leiterman [**11**] and Zhao [**16**]. Such an experiment is very reasonable and practical to carry out since the results can be used to either validate or suggest improvements to the current slender body theory. Although these experiments were very useful in broadening our understanding of the role that rod geometry plays in the overall fluid structures, we still have some very important open questions. To investigate the fluid structures using another tactic, we have taken an Eulerian approach to this problem in the hopes that we may further illuminate the subtleties of this seemingly simple experiment.

In this chapter, the experimental setup and our work on the Lagrangian tabletop experiment with the Rotational Mixing Experiment (RMX) group will be discussed. The chapter will then focus on the setup and procedure for the 3-dimensional Eulerian particle image velocimetry (PIV) experiments.

3.1. RMX setup

The description of the RMX setup has been the same for a number of years, so much of this section may be found in the thesis by Zhao [**16**]. The RMX experiment is conducted in a 30 cm cubical, clear plexiglass tank filled approximately 10 cm in height with a highly viscous silicone oil for optical clarity. Figure 3.1 [**16**] shows the tank along with the lighting and camera setup on a kinematic mount. It should be noted that this figure reflects the current setup, although Karo corn syrup, and not silicone oil, is present in the tank. The two 1024×768 pixel black and white PointGray Dragonfly cameras are positioned at the front and left side of the tank in our experimental conventions. Fiber optic illuminators are placed opposite each camera and shine through glass diffuser plates, meaning the rod and tracer particle create a silhouette in the camera images. This process simplifies rod tracking in that edge detection will be simplified.

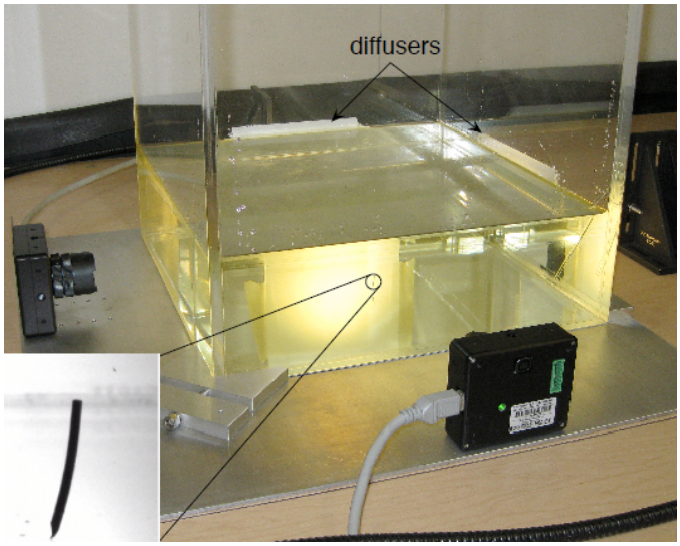

FIGURE 3.1. RMX setup (Zhao, 2010).

Above the horizontal base of the tank, a magnetically permeable rod precesses in a cone. The rod is driven by a 3000 G permanent magnet mounted on a turntable under the tank whose motion is driven by a stepper motor. Both straight and bent rods have been manufactured by Leandra Vicci with body length $l = 1$ cm and cross-sectional radius $r = 0.038 \pm .002$ cm. The curvature of the bent rods is approximately

0.40 ± 0.01 cm^{-1}. Figure 3.2 shows a collection of the bent rods used in various experiments. The base of the rod is sharpened, which provides a pivot point around which to precess.

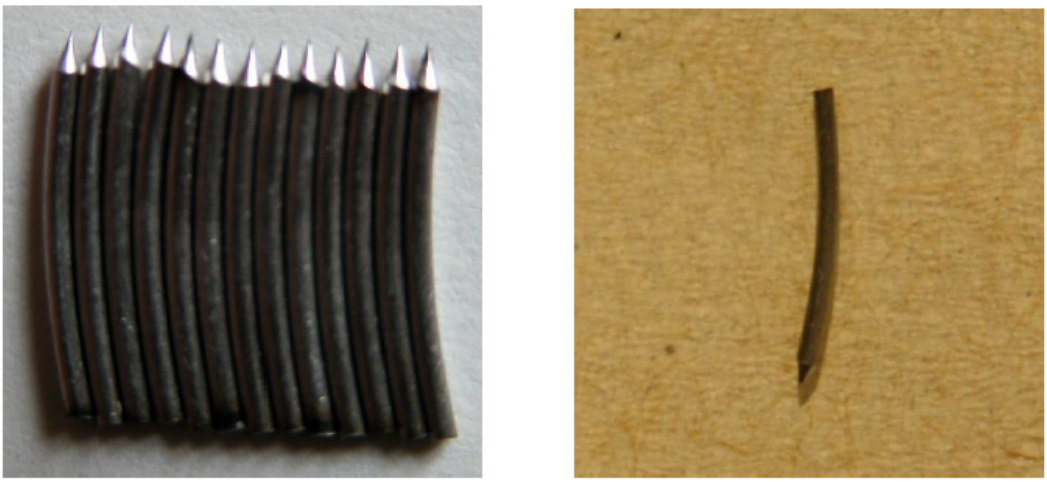

(a) A batch of uniformly bent pin with one sharped tip.

(b) One individual pin

FIGURE 3.2. Bent rods (Zhao, 2010).

The configuration of these rods is highlighted in Figure 3.3. Note that for a straight pin, the rod will simply be the red chord. For the bent rod, the sharpened base is bent out of the plane of the rod which causes a scooping angle β defined as the angle between the plane of the rod and the vertical plane through the cone axis. The chord angle κ is defined as the angle between the chord of the rod and the cone axis. This cone angle is determined by offsetting the magnet below the tank from the the rotational center of the turntable.

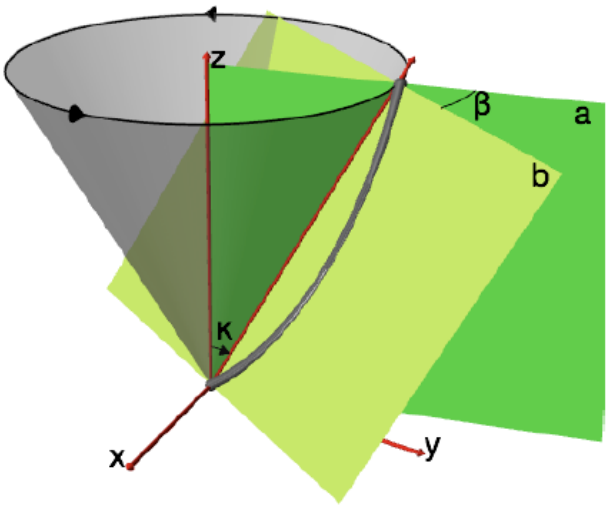

FIGURE 3.3. Rod geometry (Zhao, 2010).

The dynamic viscosity of the silicone oil and rotational rate of the magnet are selected so that we may bound the Strouhal and Reynolds numbers by 10^{-3}. With the rotational rate of the magnet defined as ω, the Reynolds number is defined as $Re = \frac{\rho\omega l^2 \sin\kappa}{\mu}$ and the Strouhal number as $Sr = \frac{\omega l}{U} = \frac{1}{\sin\kappa}$ where $U = \omega l \sin\kappa$ is the speed of the rod tip. Thus we have $SrRe = \frac{\omega l^2}{\nu}$. When $Re << 1$ and $SrRe << 1$, the fluid flow is in the Stokes regime. For the silicone oil, if the chord angle is approzimately 30 degrees and the characteristic length is given by the rod radius, the $Re \approx 10^{-4}$ and $SrRe \approx 10^{-3}$. The parameters in the problem are listed in the Table 3.1. From Cartwright [**6**], the Reynolds number for cilia flow is on the order of 10^{-3}, and is given by $Re = \frac{vL}{\nu}$ where L is the size of the nodal cilia, v is the flow rate, and ν is the kinematic viscosity of the embryonic fluid.

rod length	$l = 1$ cm
rod radius	$r = 0.036796$ cm
dynamic viscosity of silicone oil	$\mu = \rho\nu = 9500$ cP
density of silicone oil	$\rho = 0.975$ g cm^{-3}

3.2. 3D camera calibration, image processing, and 3D data construction

In order to obtain an accurate description of both the rod and tracer particle position in 3-dimensions, a calibration is performed with the Camera Calibration Toolbox for Matlab from caltech.edu. Details of this calibration process for the RMX experiment may be found in Zhao [**16**], and general information about this process may be found at the CCT website. The results of this calibration are intrinsic parameters which relate the position of each camera to the other around a commonly defined origin. Matlab functions included in the toolbox then take pixel coordinates for common points from each camera and convert them to a 3-dimensional point in space.

The video from each camera is captured as a set of raw images which are then converted to avi files for data analysis. A neutrally bouyant microballoon tracer particle is positioned at a point in the vicinity of the rod. This particle advects with the flow, and is tracked using the Video Spot Tracker program courtesy of Russ Taylor. An example frame of this particle tracking is shown in Figure 3.4. The tracking is completed for each camera, and the resulting data is then combined through the Caltech Matlab code to find the fully 3-dimensional particle trajectory.

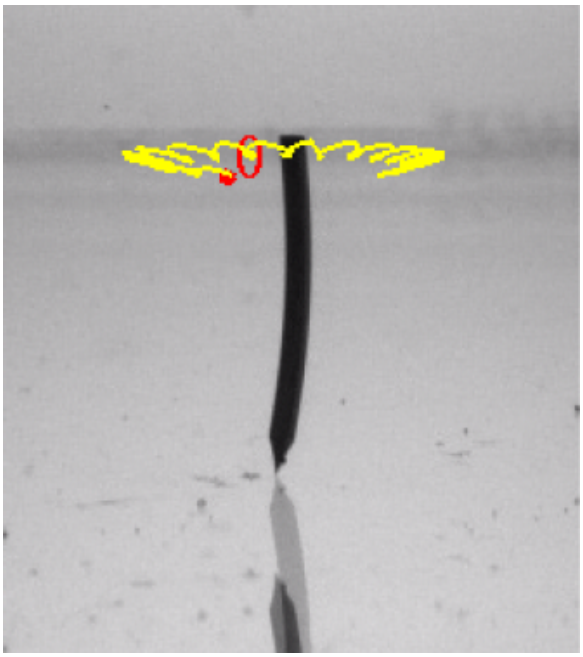

FIGURE 3.4. A sample short-term particle tracking (Zhao, 2010).

In order to compare the experimental trajectory with the fluid theory, we must have full knowledge of the angles which determine the position of the rod to input into the model. The model and geometry for this experiment are given in Figure 3.3. In order to find the chord angle κ, scooping angle β (only for the bent rod geometry), and azimuthal angle ϕ, we must track the position of the rod in the experiment. To do this, we take the following approach. First, each video is cropped to a much significantly smaller size that the native 1024×768 pixels, usually in the range of 110×170 pixels, in order to expedite the tracking. Matlab programs (presented in Appendix A) are then used to create a contour with N points at a user specified level which best describes the boundary of the rod for each video. An algorithmic approach developed with the help of David Adalsteinsson is taken to identify the extreme points on the rod.

- Let $C(i)$ represent the i^{th} point along the contour.
- For $i = 1$ through N, draw a straight line from $C(i)$ to $C(i + 6)$.
- For each of the points $C(i+n)$ where $1 \leq 5$, find the distance from said point to the straight line and call the distances $d(1)$ through $d(5)$.

- Find the maximum of these distances and log the point $C(i)$ at which this maximum occurs.
- Loop around the contour and find the maximum distances under certain constraints about the distance between the corresponding points.

A diagram of this algorithm for a given value of i is shown in Figure 3.5.

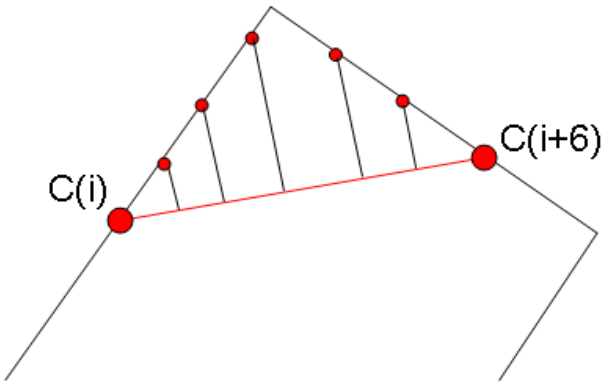

FIGURE 3.5. Corner-finding algorithm, where point $C(i+3)$ will be selected as the corner

The results are given in pixel coordinates and are the rod base along with the top left and right point of the rod tip. These last two points are then averaged to find the pixel coordinates of the rod tip. This process is repeated for each video, and correlating these pixel coordinates through the Caltech program yields coordinates in 3-dimensions for the rod base and tip. We use these coordinates along with geometrical considerations to find the chord angle κ, scooping angle β, and azimuthal angle ϕ.

In order to validate this tracking procedure, we can input these angles into the bent rod center-line geometry described in Chapter 1 to obtain a theoretical description of our 3-dimensional center-line. With knowledge of the rod radius and the Frenet-Serret frame, we can define circles around the center-line with the given radius. Such a diagram is shown in Figure 3.6 for a few such circles. Using inverse transformations in the Caltech code, we can then take the points of these 3-dimensional circles to find their pixel coordinates in each camera. For each circle in the pixel coordinates of

each camera, we may then define the extreme points and mark them on the original image. An example of this procedure is presented in Figures 3.7 and 3.8.

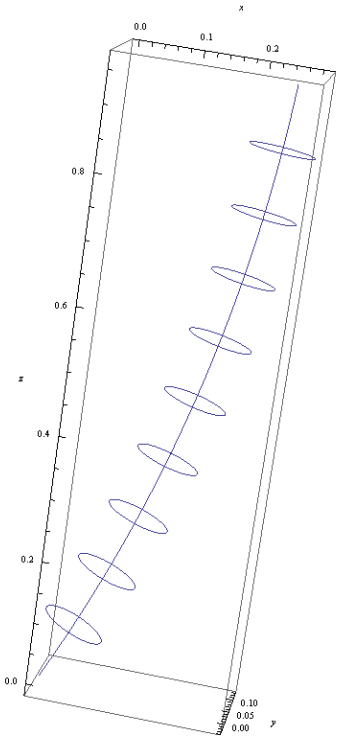

FIGURE 3.6. Theoretical center line with circles of radius r

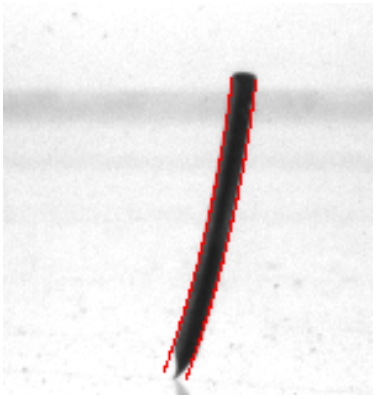

FIGURE 3.7. Edges for left camera

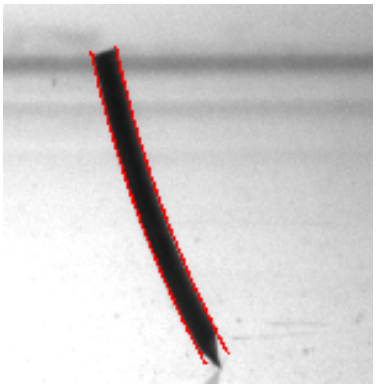

FIGURE 3.8. Edges for right camera

As we can see from the edge reproduction, this procedure does a very good job in replicating the outer contour of the rod. For a particular experiment, the tracked chord angle, smoothed cone angle, smoothed scooping angle, and azimuthal angles are presented. In the experimental setup, we follow strict alignment procedures to ensure that the cone which the rod sweeps is as upright as possible. Realistically for the bent rod geometry we may limit the tilt of this cone, which we define as the tilt angle, to under 2°. Since the chord angle is defined as the angle from the positive z-axis to the chord of the rod, and the cone angle is defined as the angle between to axis of the cone and the chord of the rod, we may define the tilt angle as the difference between

the chord and cone angles. By examination of Figures 3.9 and 3.10, we can see that the tilt angle for this particular experiment is approximately 2°. The scooping angle is always more difficult to find since it requires a third point along the center-line of the rod. We still see a pattern present in this angle, although we are not always able to perform a sinusoidal fit, and instead input the raw data into the theory.

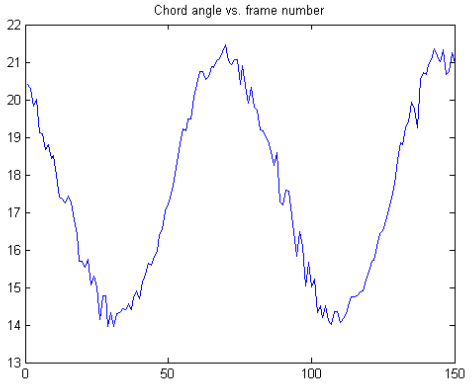

FIGURE 3.9. Tracked chord angle

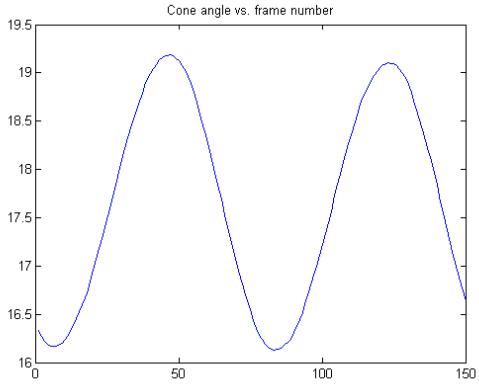

FIGURE 3.10. Tracked cone angle

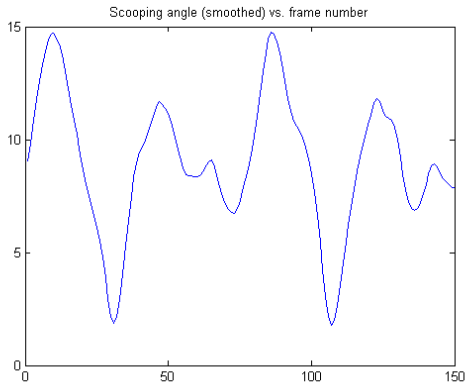

FIGURE 3.11. Smoothed scooping angle

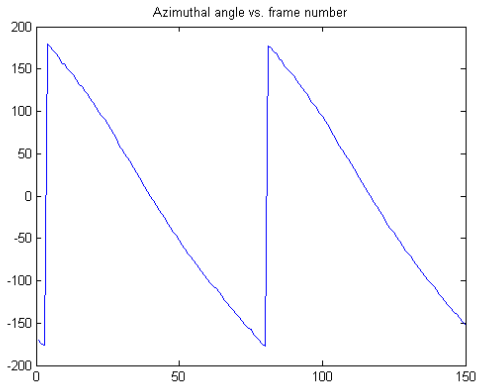

FIGURE 3.12. Tracked azimuthal angle

3.3. The role of rod geometry on particle trajectories

As the rod sweeps out a cone, a particle traces a large periodic orbit about this cone while at the same time undertaking a smaller epicyclic motion on the time scale of a single rod rotation. This motion has been been heavily documented [**11**] [**16**]. In particular, Zhao has reported the differences in these trajectories depending

on rod geometry where the initial position of the particle is $(0.6, 0, 0.5)$ cm, and using experimentally relevant parameters for the rod radius $r = 0.038$ cm, curvature $K = 0.395604$, cone angle $\kappa = 40°$, and scooping angle $\beta = 58°$. Her results presented in Figure 3.13 highlight one important difference in understanding the role of rod geometry, namely vertical transport in the case of a bent rod sweeping a cone. In the straight rod case, we see that the particle epicycles deviate from their inital plane, however there is no net vertical transport after a complete rod rotation. This vertical transport is critically important to our later discussion of the Eulerian experiments.

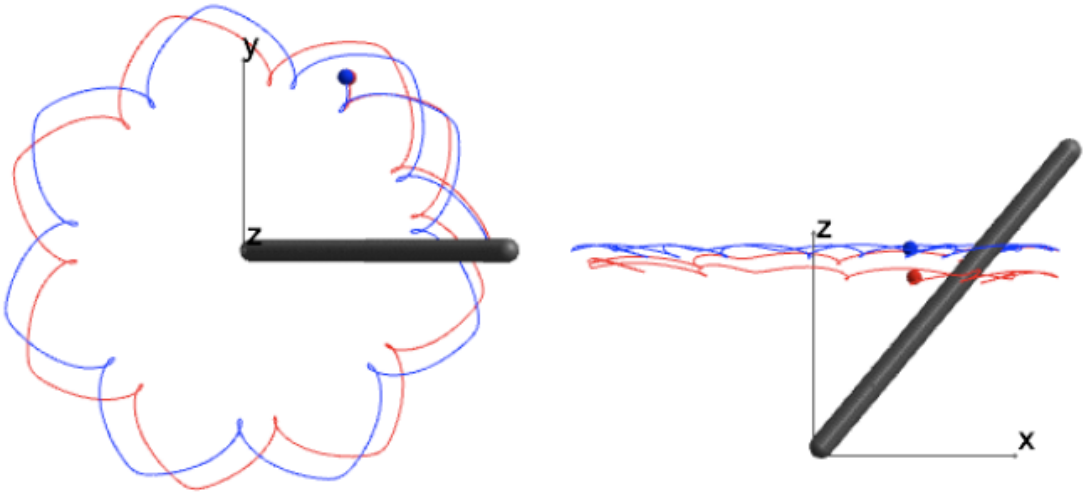

(a) Top view (b) Side view

FIGURE 3.13. Trajectories generated by a rotating straight and bent rod. The blue trajectory corresponds to the straight rod geometry, and the red trajectory corresponds to the bent rod (Zhao, 2010).

The symmetry breaking which occurs in the bent rod geometry gives rise to a long term toroidal fluid structure. This structure can be visualized by placing dye at a given point near the rod and allow the flow to develop. This structure is shown in Figure 3.14.

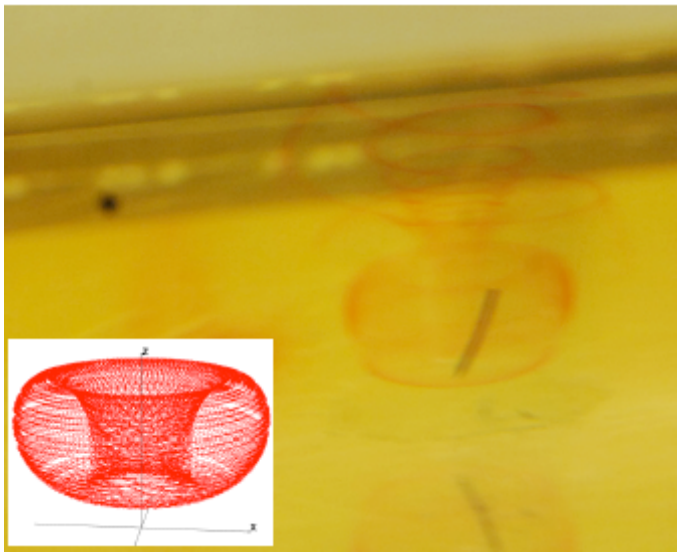

FIGURE 3.14. The long-term toroidal flow structure for a bent rod scooping a cone above the plane (Zhao, 2010).

The rotational motion of the rod in the experiment yields a theoretical velocity field defined in Chapter 1 with appropriate Stokeslet strength distribution given as $\boldsymbol{\alpha} = \frac{\omega\epsilon\sin\kappa}{2}(0, s, 0)$ for a straight rod sweeping an upright cone above a no-slip plane. Once we have dynamically tracked chord, scooping, and azimuthal angles to input into the theoretical model, this velocity field may then be numerically integrated using a standard Runge-Kutta scheme to find particle trajectories. These theoretical trajectories may then be directly compared to the experimentally tracked particle trajectories. For the case of a straight rod sweeping an upright cone, this direct comparison can be seen in Figure 3.15.

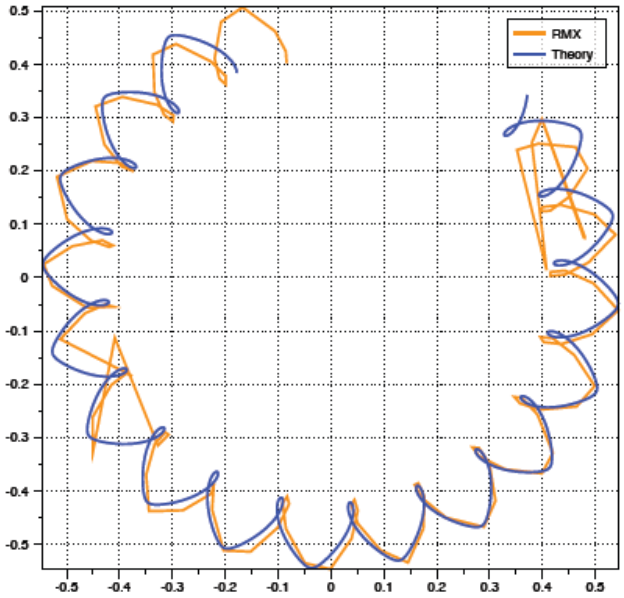

FIGURE 3.15. Epicycle agreement with experimetal data for the full Blakeslet no-slip solution (Leiterman, 2006).

The discontinuities in the experimental trajectories appear due to the tracer particle being occluded by the rod in one or both cameras for a given number of frames. What we see is in this comparison is that the epicycle amplitude, defined in one manner as the peak-to-peak distance of the epicycle, is predicted very well by the theory. Noting that in this experiment the period of the rod rotation is approximately 5 seconds, this agreement persists over long time scales.

If we move to the bent rod case, we see drastically different results [**5**]. Undertaking similar comparisons with experimental data yields 3-dimensional plots such as Figure 3.16. This plot shows an almost immediate deviation in epicycle amplitude from the experimental data. This deviation has been shown to be on the order of 15%. Understanding this disagreement between theory and experimental data is a crucial step in suggesting corrections for the theory.

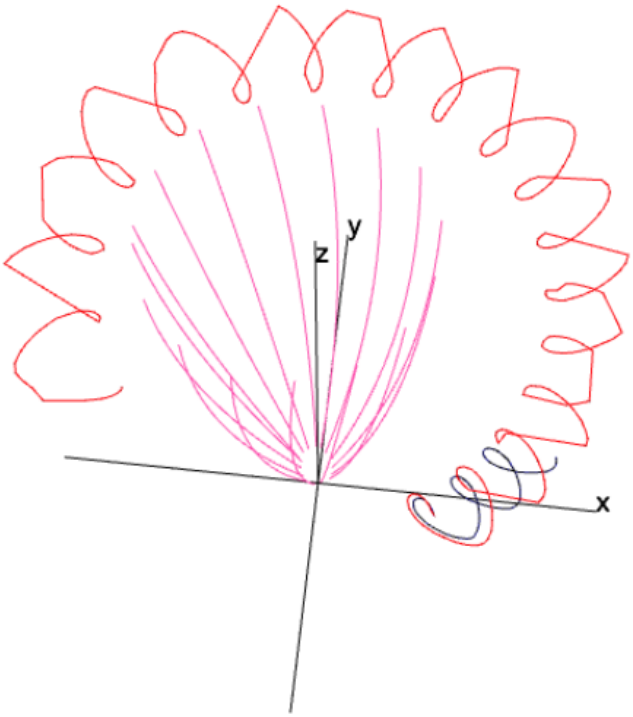

FIGURE 3.16. Short-time epicycle disagreement for the bent rod experiment. The experimentally tracked trajectory appears in red, and a short-time theoretical trajectory in black [**5**].

CHAPTER 4

Eulerian experiments for a rod sweeping a cone over a no-slip plane

In order to better understand this disagreement in epicycle amplitude between experimentally tracked particle trajectories and those created from the slender body theory, we approach this problem from an Eulerian point of view. By examining the velocity field over time, we have the potential to give valuable insight into the shape of the velocity field, the vertical transport, and particle epicycle amplitudes. We employ particle image velocimetry (PIV) in this experiment in order to obtain a fully 3-dimensional velocity field in a horizontal plane just above the rod tip.

PIV involves seeding the fluid with microscale hollow glass spheres which are assumed to be small enough that they do not have any induced effect on the fluid flow. These particles are then illuminated by a laser sheet, and their motion is captured by two cameras. For each camera, frames are examined pairwise, and an algorithm discerns how the position of discrete patches of these particles change. Proper calibration allows the algorithm to correlate these patches in 3-dimensional space, which will then result in a fully 3-dimensional velocity field reported in the plane of the calibration. Care should be taken to ensure that this calibration plane is approximately the same plane as that of the laser sheet.

In this section, we will first discuss the unique setup for this experiment, along with the calibration and data collection procedures. Next, a discussion as to the efficacy of the PIV system will first be presented in the form of a benchmark using well-know results for rotational flow. Finally, we will discuss the many results obtained by these experiments for a rod rotating above a no-slip plane, along with their implications for the current theory.

4.1. PIV setup, calibration, and data collection

In the PIV experiment, we will use the same 30 cm clear, cubicle, plexiglass tank from the traditional table-top RMX experiment. This tank is attached to a kinematic mount and filled to a height of approximately 10 cm with 1250 cSt silicone oil. For the PIV experiment, the silicone oil is then seeded with microscale hollow glass spheres. The Dragonfly cameras from the Lagrangian experiment remain attached to the kinematic mount, which allows us to run a PIV experiment and then capture rod position data in order to dynamically track the angles describing the position of the rod.

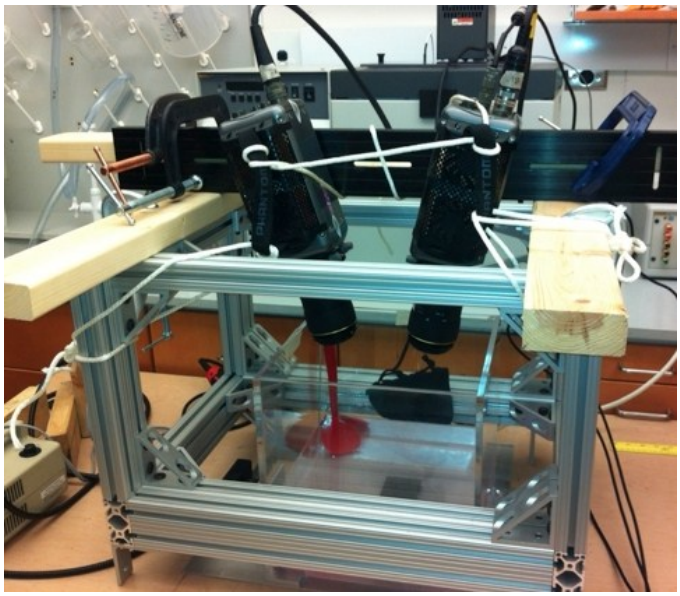

FIGURE 4.1. Setup for PIV experiment.

The PIV experiment itself contains a much more sensitive setup. Two Phantom v9.1 cameras are mounted on an optical rail and secured to a cage structure built from 80/20 material is positioned to envelop the tank. These cameras are each fitted with a Scheimpflug mount to correct for optical distortions, as well as a Tokina AT-X PRO D 100 nm F2.8 macro lens. These macro lenses will allow us to examine the fluid velocities on a small scale for small focal lengths. A Litron Lasers NANO L50-100PIV Nd:YAG laser is positioned approximately 1 meter from the tank, and the optical head is set to produce a horizontal laser sheet at a user-defined pulse rate.

The setup for this experiment is shown in Figure 4.1. The laser and cameras are synchronized through an external triggering mechanism. This mechanism is attached to a computer specially equiped by LaVision Inc. to run these PIV experiments within a program called DaVis. This program allows us to calibrate the system, fully control the laser and camera timing, and process the raw data to obtain 3-dimensional velocity field results.

The field of view for this experiment is approximately 50×50 mm, so the laser being positioned 1 meter away from the tank (in order to have room for a person to set up the experiment) means that the alignment of all the constituent pieces of the experiment plays an essential role. The first step in our setup is to align the rod in the same manner as the table-top Lagrangian experiment. To do this, we adjust the magnet under the tank to align it with the center of rotation of the carriage. Once this is done, we may move the tank on its kinematic mount in order to align the rod in a vertical position. We then hold the tank steady for the duration of the calibration and experiment.

In order to calibrate the cameras, a 55×55 mm calibration plate with markers in two planes is positioned horizontally at a desired height above the base of the tank. From here two separate procedures must be undertaken. First, we must calibrate the cameras. This is done within the DaVis program by specifying our calibration plate type, and then manually adjusting the focus and Scheimpflug correction for each camera so that the calibration plate is sharply in focus. This procedure takes an image of this calibration plate from each camera and correlates them in 3-dimensions using commonly defined markers on the plate. An example of the marker detection is shown in Figures 4.2 and 4.3.

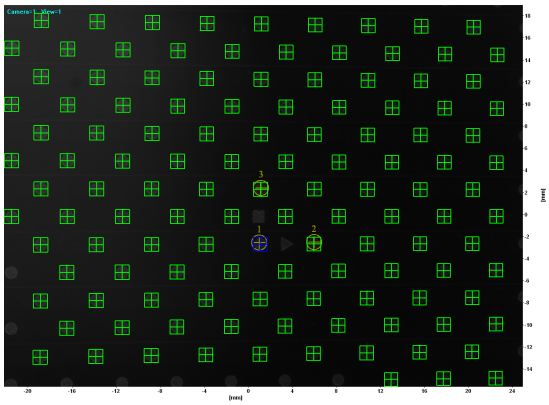

FIGURE 4.2. Marker detection: left camera.

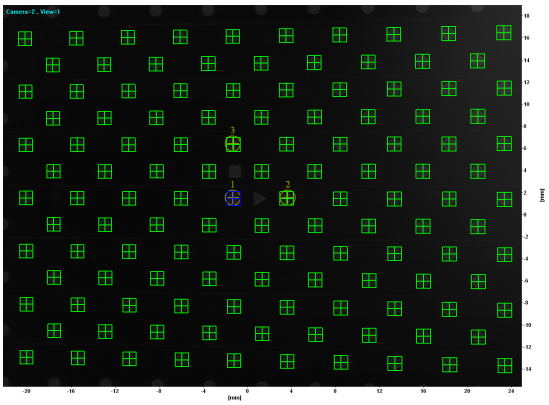

FIGURE 4.3. Marker detection: right camera.

Since the focal length of the cameras will be set at $f2.8$, the laser sheet must be accurately aligned with the calibration plate to ensure that the illuminated tracer particles will be visible and in focus within the field of view of the camera. The laser alignment is a manual user-controlled process, meaning that alignment in the vertical position of the laser, as well as the vertical and horizontal alignment of the laser sheet, must be done by hand. This process requires constant checking in multiple directions in the space between the optical head and the tank to ensure precision in the roll and pitch of the laser sheet. This manual process may be time consuming, but with the use of a ruler precise to the 100th of a centimeter, we can ensure by basic trigonometry that the roll and pitch of the laser sheet are well within a tenth of a degree across the field of view of the camera.

Once the cameras are calibrated and the laser is aligned, we remove the calibration plate and replace the rod, taking care to align it in its previous vertical position. The magnetic carriage is then adjusted to set the magnet off of the center of rotation, which sets the cone angle defined in the problem.

The experiment itself is run for 60 seconds, where our angular speed is set so that a single rod rotation takes approximately 6.7 seconds. The procedure followed states that we start the stepper motor which controls the magnetically driven rotation of the rod and let this system remain untouched for at least one minute. This ensures

that initial transients are cleared and the rod motion should be steady. Once this time has elapsed, we synchronize the laser and cameras so that each time the laser pulses at $15Hz$, the cameras record a frame. The resulting 15 fps video is then moved from the cameras to the computer via ethernet for local storage.

Next, the data is processed by inputting the raw videos into a program which performs the PIV calculation and outputs the result as a vector field for each frame. This process makes use of the intrinsic paramters relating the cameras which were found in the calibration step. An example of a vector field resulting from the PIV calculations for an experiment with a bent rod sweeping a cone is presented in Figure 4.4. We will discuss such results in depth in the coming sections.

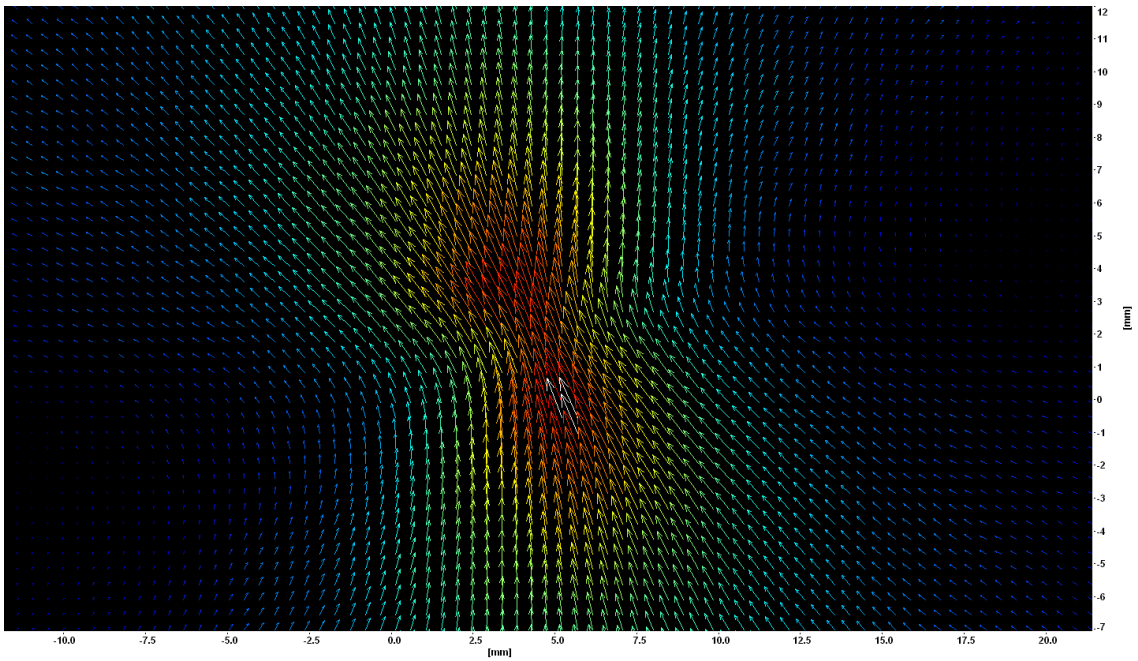

FIGURE 4.4. Example frame of vector field data.

The vector field we obtain is defined in the plane of the calibration plate, and it shows the projection of the 3-dimensional velocity vectors onto this plane. The color shown represents the magnitude of this velocity. This vector data may be exported as text files for each frame which gives the x and y position in this plane along with each of the three velocity components. This data is then analyzed using specially designed Matlab programs to investigate particular features of the velocity field.

4.2. PIV benchmarking

As utilizing this PIV system to the extent presented here had not yet been done, it was a natural question to ask about the efficacy of this system. Our goal is to accurately measure 3-dimensional velocity fields in a certain plane in an Eulerian experiment which we know from our Lagrangian experiments may have unresolved issues. In order to understand the extent to which may may trust measurements in this system, we undertook a benchmark using the well know results of rigid body rotational flow. In this benchmarking experiment, we place a cylindrical tank with diameter 30 cm on the rotating carriage from the table-top experiment. The tank is filled with the same 1250 cSt silicone oil and seeded with the same PIV tracer particles as previously stated in the PIV setup. If we allow this cylindrical tank to rotate for long enough, it should reduce to the case of rigid body rotation, where the magnitude of the velocity in some horizontal plane is given simply as

$$v = r\omega$$

where r represents the distance of a point from the center of rotation and ω is the angular speed. Such an experiment would yield somewhat useful results, but here we are more concerned with the accuracy in our measurements of vertical velocity. To obtain a vertical velocity measurement in this setting, we used a laser sheet which was tilted by an angle α. The cameras must then be calibrated to the calibration plate tilted at this same angle. Velocity measurements in this tilted plane will then yield an out-of-plane component along slices which are perpendicular to the front of the tank. Basic geometry tells us that the vertical velocity along such a slice through the center of rotation should then be given by

$$v_z = r\omega \sin\alpha$$

In this particular experiment, we match frames in the raw video to obtain our rotational rate. We find that the tank takes 127 frames to complete one revolution,

which at a recording rate of 15 fps, gives us an angular speed of $\omega = .742$ 1/s. The tilt angle in the laser sheet was measured to be 13.6°, which gives us our expected vertical velocity along a slice through the center of rotation as

$$v_z = 0.1745r$$

The PIV data in our benchmarking experiment appears in Figure 4.5.

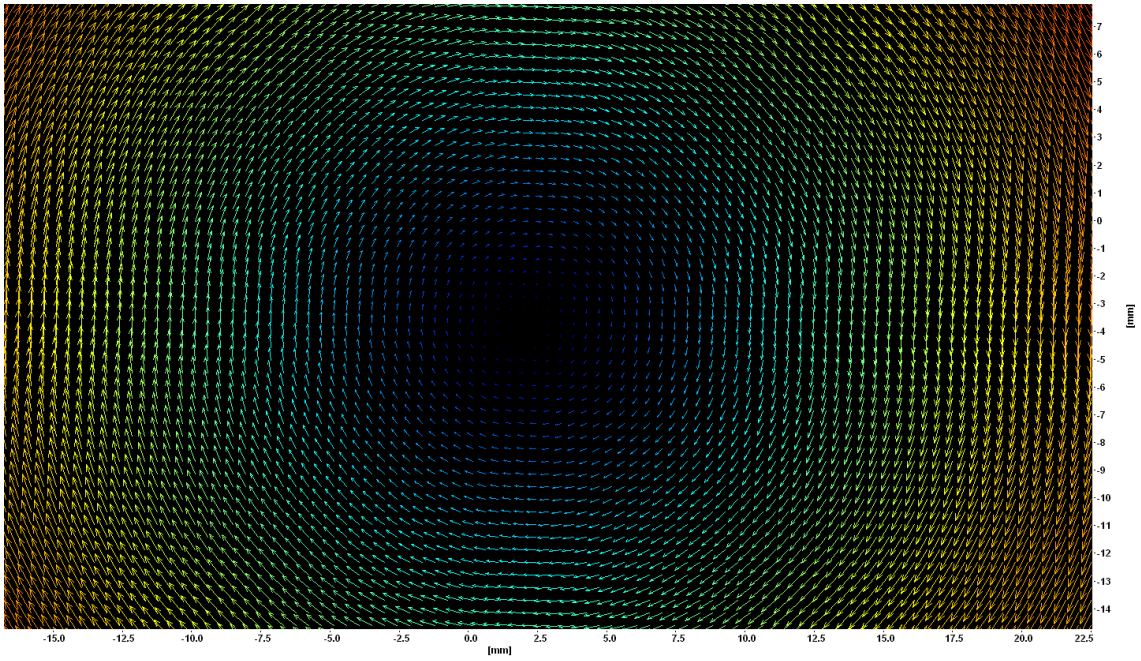

FIGURE 4.5. Example frame of vector field data in the benchmarking experiment.

Exporting the vector field data to Matlab allows us to define the center of rotation and to find the vertical velocity along a vertical slice through this point for all frames, which may then then plot in Figure 4.6. This figure also contains the mean of these slice. We note that the individual slices have some jaggedness due to interpolation in the PIV procedure, but the mean is quite smooth. This fact will be exploited in our later PIV experiments to obtain time-averaged measurements along slices.

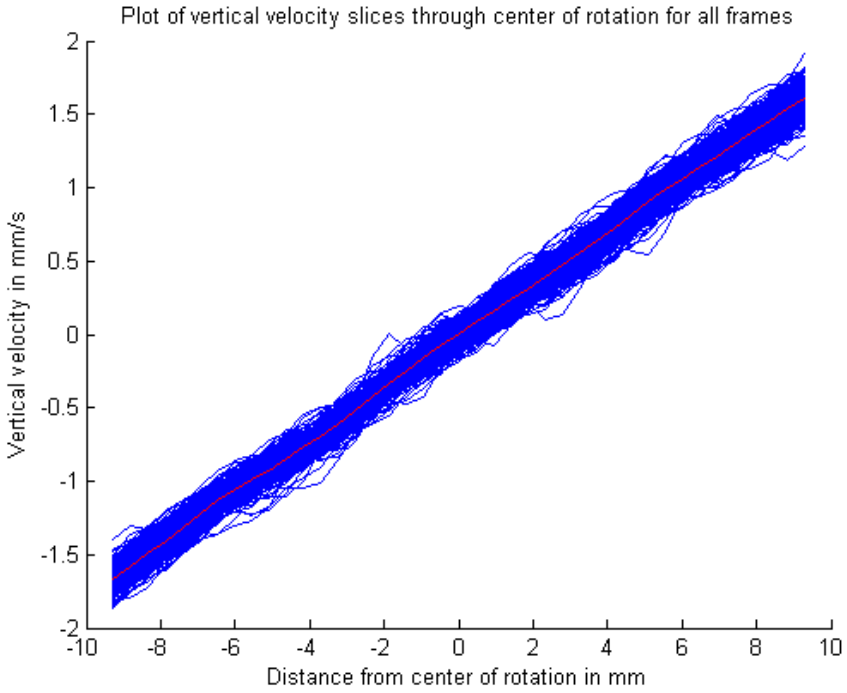

FIGURE 4.6. Vertical velocity along slices through center of rotation.

With our expression above for the vertical velocity, we would like to compare the slope of this mean with our theoretical value of 0.1745. The slope of this mean line in the experiment is 0.1768, and the relative error is given by

$$Error_{rel} = 100 \times \frac{0.1768 - 0.1745}{0.1745} \approx 1.3230\%$$

This result shows that measurements in the vertical velocity should be very accurate for experiments with comparable flow rate. The resulting slopes of the vertical velocity component being clustered closely together shows yet another important aspect which must be taken into consideration in the experiment - namely that convection effects will not dominate our velocity signal. Independent PIV measurements have been caried out in the RMX tank which confirm that drift due to convection is on the order of .25 mm per minute.

It should be noted that the vertical velocity along a perpendicular slice through the center of rotation of the cylindrical tank will always be zero. This is easily explained as the velocity vectors in rotational flow at these points will lie completely within the

tilted plane. The result when examining such slices gives a good idea of the noise present in the system, and we do recover a mean of zero in this case.

4.3. PIV results for a bent rod sweeping a no-slip cone above a plane

In this experiment, we investigate the 3-dimensional velocity field in a plane at a height of 1.105 cm above the base of the tank. As we move away from the rod, the velocity will decay rapidly, so this height is chosen so that we are close enough to the rod tip to see a well-defined velocity profile. The laser sheet thickness must be chosen such that the tracer particles do not leave the sheet between processed frames. In our experiment, the laser sheet has a thickness of approximately 1 mm, which because of the rather slow flow rate which is bounded by the speed of the tip of the rod $\omega\ell \sin\kappa$, allows us to resolve the motion of the tracer particles in 3-dimsensions.

Unfortunately with this PIV method, we are unable to investigate velocity fields in a horizontal plane which intersects the rod due to large reflections from the rod surface. This problem may be overcome with the use of special tracer particles which, when excited by the laser, emit light at a different frequency. Band-pass filters may then be applied to the camera lens in order to reject frequencies outside of those emitted by the particles.

The main focus in these experiments is to obtain quantitative results describing vertical transport along with estimates of particle trajectories in order to directly compare these results to the theory. First, we examine the effect of the scooping angle on vertical transport in the bent rod geometry. We then discuss a comparison of particle epicycles for this experiment, which we will approach in a unique way when comparing them qualitatively with the theoretical predictions.

Finally, a study of the effects of the free-surface will be presented. In this study, we note that the current theory has neglected this free surface since it was assumed that its effects would be asymptotically subdominant to the flow induced near the rod. The results of this study are surprising, and may lead to a correction in the fluid theory.

4.3.1. Effects of scooping angle on vertical transport. When introducing a study of vertical transport, it is important to define the metrics which we will use to quantitatively analyze this phenomenon. By examination of velocity field in Figure 4.4, we see that one metric which describes vertical transport would be to examine the vertical velocity on a slice through the center of this field. The issue here is that the field is rotating over time, so that we must automate a procedure which tracks the shape of this field and then defines a slice through it in the proper manner.

To accomplish this, we set a treshold on the in-plane speed $\sqrt{v_x^2 + v_y^2}$, which will define a region. This region will have an associated orientation and center, which we will use to define a slice through the region. Once this slice is defined, we simply interpolate the vertical velocity field along the slice. An example of this region is shown in Figure 4.7, and an example of the resulting vertical velocity along this slice is given in Figure 4.8.

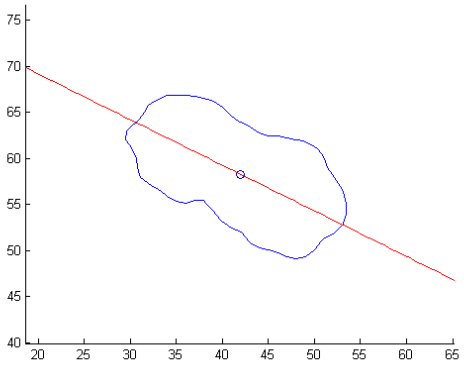

FIGURE 4.7. Example of region showing centroid and orientation.

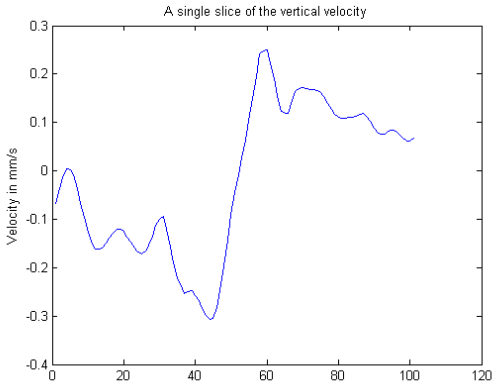

FIGURE 4.8. Example of vertical velocity along this slice.

In general, our measurements of the vertical velocity are much less smooth due to the orientation of the cameras. In order to obtain smoother results and a better metric for describing vertical transport, we time-average the slices which we obtain for each frame. This produces very smooth plots.

We consider an experiment for a bent rod sweeping an upright cone above a no-slip plane with a cone angle of 16.9° and rotational period $T = 6.5$ s over a duration of 60 seconds. We first run the experiment with the rod precessing counter-clockwise with scooping angle 58°. The experiment is then repeated, but by changing the direction of the stepper motor, the rod is now anti-scooping at an angle of 55°. For each experiment, we find the time-averaged mean of the vertical velocity along the slices we have defined earlier. The results are presented in Figure 4.9.

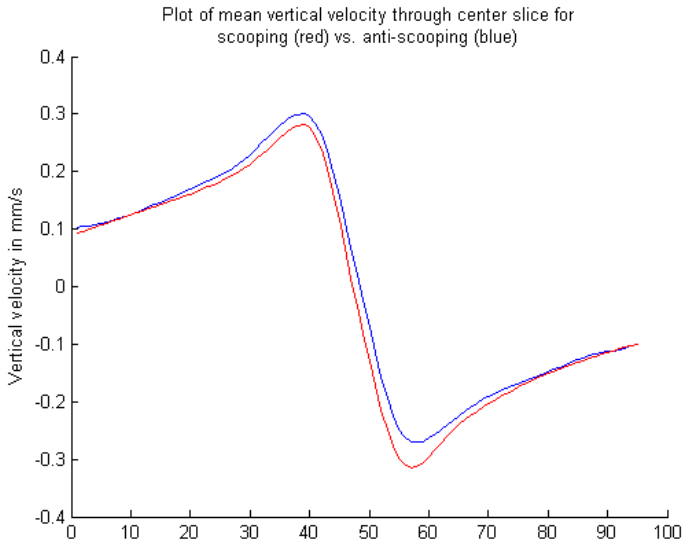

FIGURE 4.9. Mean vertical velocity along slices for $\kappa = 16.9°, \omega = \frac{2\pi}{6.5}$ and $\beta = 58°$ (red) and $\beta = -55°$ (blue).

From this plot, we can immediately see that the mean vertical velocity along this slice is greater for the case of an anti-scooping rod. In fact, we have that for the scooping rod the maximum vertical velocity here is $v_{max} = 0.2817$ mm/s and the minimum is $v_{min} = -0.3149$, while for the anti-scooping rod, the maximum vertical velocity here is $v_{max} = 0.3009$ mm/s and the minimum is $v_{min} = -0.2709$. Furthermore, the mean of each of these curves is given as

$$v_{z,avg}^{scoop} = -0.0095 \text{ mm/s}$$

$$v_{z,avg}^{anti-scoop} = 0.0070 \text{ mm/s}$$

In this metric, we see the important fact that vertical transport reverses direction depending on whether the rod is scooping or anti-scooping. We note that the scooping angle is slightly less in the case of reversing the direction of the rod motion. This phenomenon has been documented in Zhao [**16**], and we see the effects of this slightly smaller scooping angle by noticing that the maximum to minimum vertical velocity values are not as extreme in the case of the anti-scooping rod. This metric is useful in determining the vertical transport in regions very close to the tip of the rod.

It should also be noted that the estimate of the convection in the tank reported in the benchmarking section was approximately .25 mm per minute, which is 0.004 mm/s. This is the *magnitude* of the convection velocity, which itself is on the order of the average vertical velocities reported above. However, in the region in which the experiment takes place near the center of the tank, these convection effects are nearly all planar, and the vertical velocity due to convection in this region is approximately 5×10^{-5} mm/s reported from the PIV measurements. This allows us to conclude that convection will not dominate these vertical velocity signals even though they are extremely small.

4.3.2. Long-term vertical transport. From these same experiments, we may be able to understand the long-term toroidal flow structure shown in Chapter 3 using only this short-time experiment. To better understand the more general vertical transport properties of this flow, we now look at the average vertical velocity along circles of varying radii about the center of rotation of the rod. This metric will not only capture the vertical transport of a particle near the rod tip, but it also captures the behavior of particles at other points along the rotation of the rod.

To retrieve this data, we must use the region data from the previous discussion. As the rod rotates, we have rotating regions, each of which with a defined center. These centroids will define a center of rotation, and we may then define circles with a given radius about this point. These centroids are shown in Figure 4.10 for the scooping rod experiment.

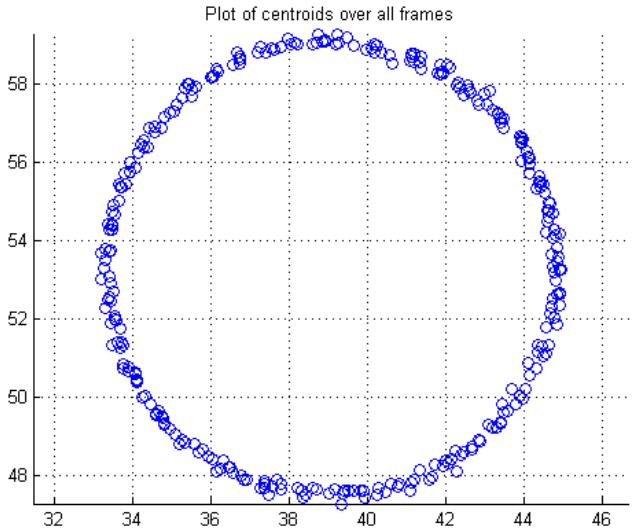

FIGURE 4.10. Tracked centroids for the scooping rod experiment.

In this case, we have two sets of experimental data. Both sets involve an angular speed of $\omega = \frac{2\pi}{6.5}$ and two individual runs, one with scooping angle $58°$ and the other with an anti-scooping rod with scooping angle $-55°$. The key difference between these two sets is that the cone angle in the first set is $16.9°$, and the cone angle in the second experiment is $14.1°$.

For the first set of experiments with cone angle $\kappa = 16.9°$, the average vertical velocity along circles is plotted against the circle radius. This can be seen in Figure 4.11 with red corresponding to the scooping data and blue corresponding to the anti-scooping data. Again here we can see that these curves are not exactly symmetric since the scooping angle of the anti-scooping rod is slightly less than the angle for the scooping rod.

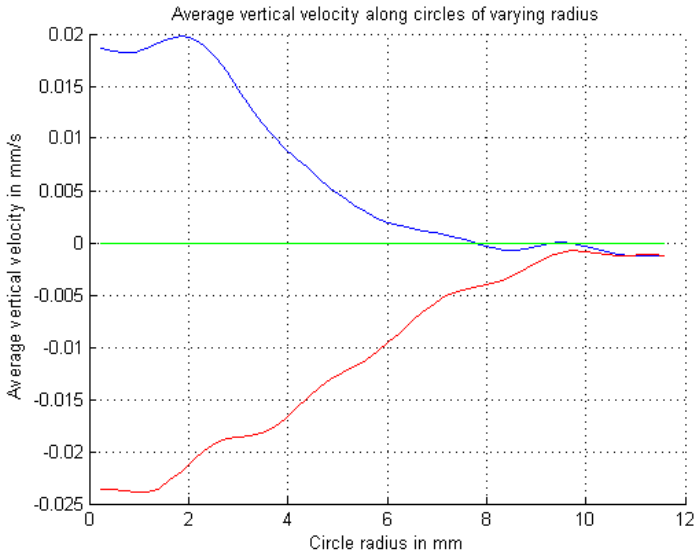

FIGURE 4.11. Average vertical velocity along circles of varying radius for $\kappa = 16.9°$.

The second set of experiments for $\kappa = 14.1°$, we produce a similar plot in Figure 4.12, again noting the asymmetry. We note that due to the slightly smaller cone angle, the vertical velocities are smaller than the previous set of experiments. The characteristics of the curve are also consistent with the results of the first set of experiments.

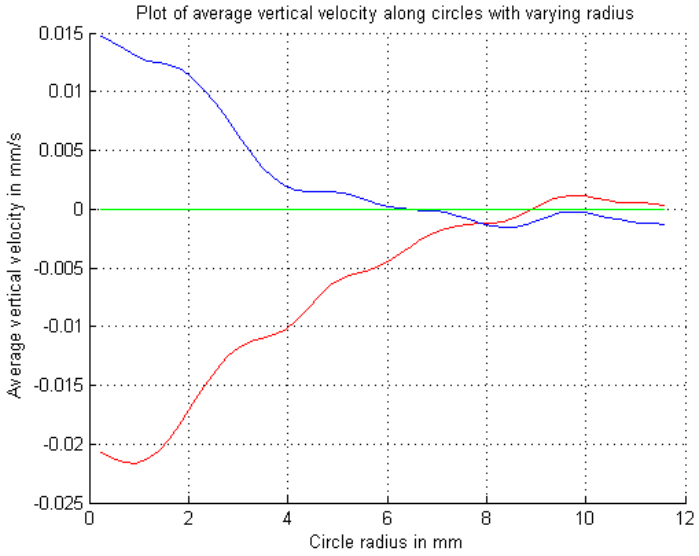

FIGURE 4.12. Average vertical velocity along circles of varying radius for $\kappa = 14.1°$.

These results give us the direction of vertical transport, and it is important to note that there is some radius for which the average velocity changes sign. This shows that within a certain region close to the rod, we may predict the direction of this long-term torus, and the scales on which it may develop. These results may be directly compared to the theoretical predictions shown in Figure 4.13 [**5**]. The previous plots show a very similar structure. It should be noted that the units in Figure 4.13 are non-dimensionalized so that the rotational period of the rod is 1 second. Conversion to our measurements in mm/s require dividing the velocity by a factor of 6.5, which is the rotational period for our experiments. Doing this, we see that we have both qualitative *and* quantitative agreement in this metric.

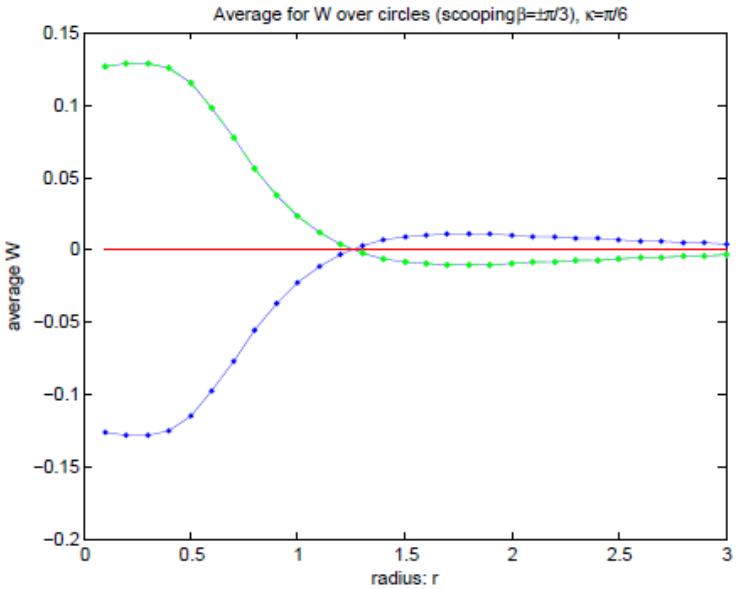

FIGURE 4.13. Theoretical average vertical velocity along circles of varying radius for $\kappa = \frac{\pi}{6}$.

4.3.3. Comparisons of experimental and theoretical trajectories. The results of the PIV experiments are fully 3-dimensional velocity fields given in a plane, but this plane only has a thickness on the order of 1 mm. This means that reconstructing fully 3-dimensional particle trajectories is impossible, as a given particle will certainly leave this plane. We can however constrain the vertical velocity to be zero, specify a starting point in this plane, and create trajectories using only the planar

velocity components. These trajectories, while not true trajectories of a particle starting at the given point, are projections of the trajectory in the horizontal plane. For the given starting point, we may construct particle trajectories using the fluid theory in a similar manner by constraining the vertical velocity to be zero. A comparison is made for a bent rod with scooping angle 58°, cone angle 16.9°, and period 6.5 s in Figure 4.14. For both the theory and experimental data, the trajectories are created using a fourth order Runge-Kutta scheme. Details of the Matlab code involved with this process may be found in the appendices.

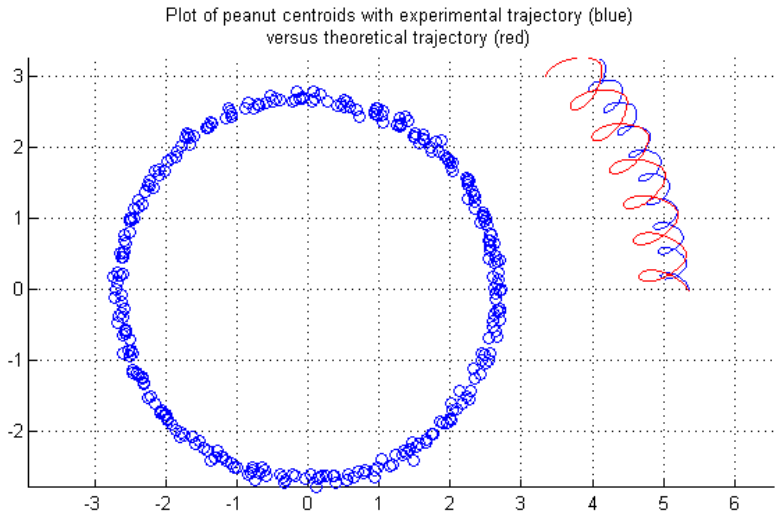

FIGURE 4.14. Experimental particle trajectories (blue) vs. theoretical particle trajectories (red).

In this figure, we see that the experimental particle trajectory has a smaller epicycle amplitude than the theoretical prediction. This results is in direct contradiction to our prior knowledge of the relative differences in epicycle amplitudes. The numerical integration scheme may contain errors which must be resolved, but the plot is shown here in any case as an example of such a direct comparison and an example of the power of the PIV measurements given as velocity components in a plane on a grid.

4.3.4. Free-surface effects on vertical transport and trajectories. In order to examine the effect of changing the free-surface height on the vertical transport, we run two experiments with the bent rod scooping an upright cone with scooping angle 58°. The first experiment is run with cone angle $\kappa = 19.1°$ and a free-surface height of 10.5 cm. The second is run with a cone angle of $\kappa = 18.5°$ and a free-surface height of 8.5 cm.

For each of these experiments, we may examine the two metrics discussed in the previous sections. First, we may look at the mean velocity along slice through the center of the velocity field at the rotating tip of the rod, shown in Figure 4.15. The means of these curves are very similar at -0.0033 mm/s, however we see that for the free-surface height of 10.5 cm, the values of the vertical velocity along this slice are more extreme from peak to peak.

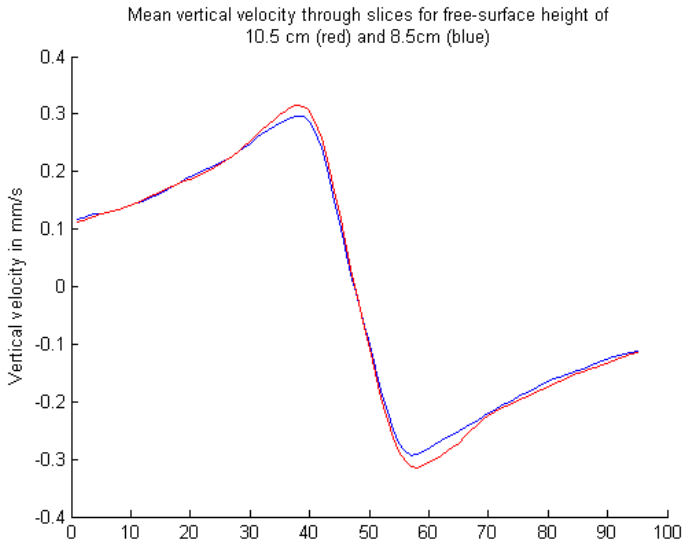

FIGURE 4.15. Mean velocity along slices for a free-surface height of 10.5 cm (red) and 8.5 cm (blue).

We may then examine the average vertical velocity along circles of varying radii for each experiment. This result is shown in Figure 4.16. The surprising conclusion drawn from this plot is that decreasing the free-surface height by only 2 cm decreases the average vertical velocity along circles by half. Plans are underway to verify this

phenomenon in a second experiment using three different free-surface heights since this result could alter the fluid theory greatly.

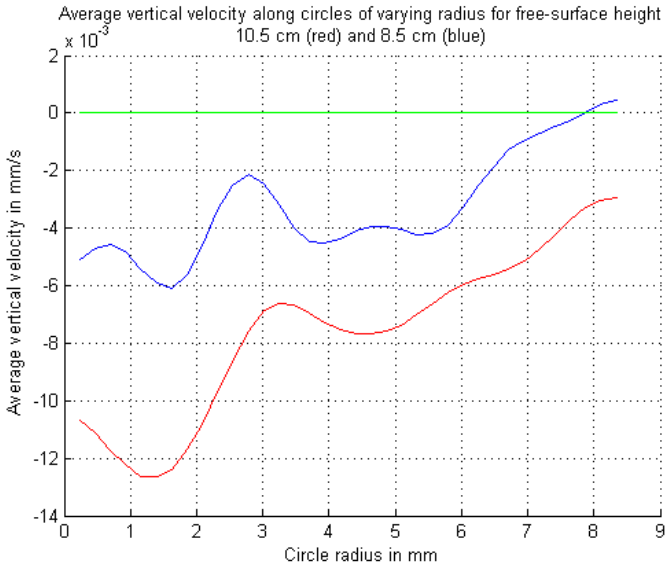

FIGURE 4.16. Average vertical velocity along circles of varying radius for free-surface height of 10.5 cm (red) and 8.5 cm (blue).

Finally for these two experiments, we may compare the particle trajectories which we obtain using velocity data from each experiment. In order to create these trajectories, we note that similarly to the previous case, the vertical velocity is constrained to be zero so that the particle trajectory is obtained using only the planar velocity. This comparison is presented in Figure 4.17 along with the tracked centroids for each experiment, which measure the center of the velocity field for each frame.

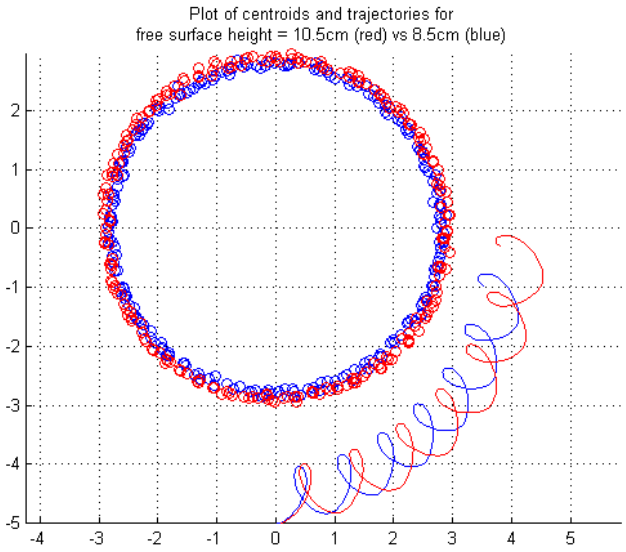

FIGURE 4.17. Experimental particle trajectories for a free-surface height of 10.5 cm (red) and 8.5 cm (blue).

We see that the particle travels further for a free-surface height of 10.5 cm. From this we may conclude that the planar velocity is greater for the higher free-surface. It should be noted that our cone angle is 0.6° larger for the higher free-surface experiment. This can be seen by observing that the for the higher free-surface case the tracked centroids in Figure 4.17 lie outside the centroids for the lower free-surface experiment. It has been shown from the theory that a 0.6° difference in cone angle is not enough to explain the difference in planar velocity which we see here.

4.3.5. Corrections to the fluid theory. As the theory currently stands, changing the free-surface height has little impact on the average vertical velocities over circle of varying radii, as shown in Figure 4.18. The free-surface is not orignally part of the model as we consider the full Blakeslet solution for a rod above a no-slip plane. If the free-surface is considered, we must satisfy the condition that there is no normal flow at this surface. This consideration necessitates the use of an image singularity above the free surface. The figure below shows that when a Stokeslet is used to satisfy the

surface boundary conditions, there is a small effect on the average vertical velocity as we change the height of the free-surface.

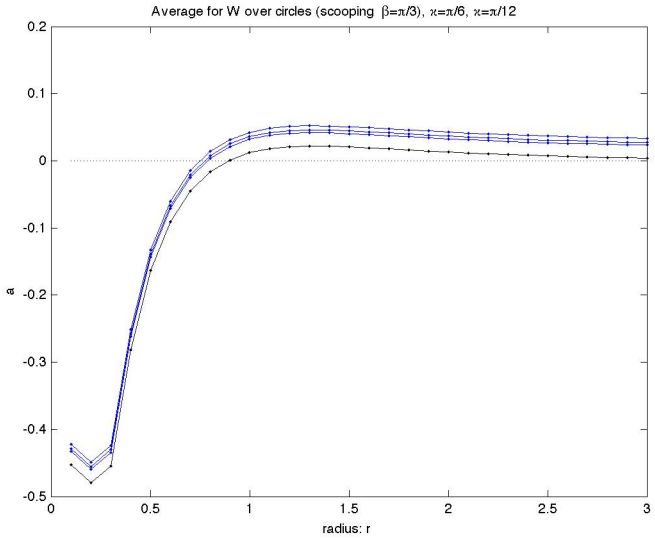

FIGURE 4.18. Average vertical velocity along circles of varying radius for free-surface heights of 8.5, 10.5, 12.5 cm with no free-surface (black) vs. Stokeslet imaging for the free surface (Zhao).

On the other hand, we may consider a free-surface which satisfies a no-slip boundary condition. This requires the use of a Blakeslet image at the free-surface. The use of this Blakeslet imaging allows us to compare the average vertical velocity along circles of varying radii to the use of Stokeslet imaging for a fixed free-surface height of 8.5 cm. This result is seen in Figure 4.19 (Zhao). In the figure, we see that the use of the Blakeslet image reduces the average vertical velocity by the greatest factor.

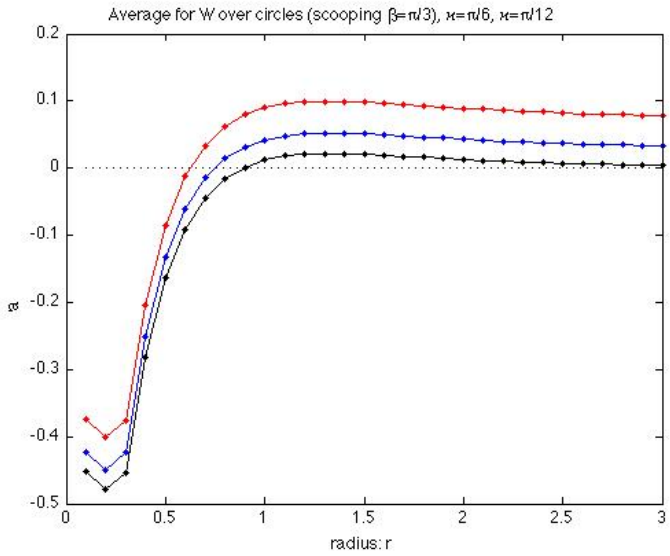

FIGURE 4.19. Average vertical velocity along circles of varying radius for a free-surface height of 8.5 cm with no free-surface (black) vs. Stokeslet imaging (blue) and Blakeslet imaging (red) for the free-surface (Zhao).

4.3.6. PIV conclusions and future work. The PIV experiments have been invaluable in the understanding the local and large-scale structures of the fluid flow for a bent rod sweeping a cone above a no-slip plane. Through examination of the various metrics presented in the previous sections, we have shown the effect of scooping angle on vertical transport, and the short-time indication of the large-scale fluid structures which we see over long periods of time. Perhaps more importantly, through our free-surface experiments we have obtained valuable and surprising information regarding the effects of changing the free-surface height on both vertical transport and particle trajectories. This new information is used to consider corrections which had been previously assumed to be negligible.

It is our hope that continued work on this experimentation in terms of a second free-surface study to corroborate the first will lead to an even better understanding of the role which the free-surface plays in the experiment. These results also suggest future work considering the effects of the tank walls and their appropriate imaging in the fluid theory.

CHAPTER 5

A comparison between singularity theory and lubrication theory for a sphere translating parallel to a plane wall

The fluid slender body theory for a rod sweeping a cone above a no-slip plane presented in Chapter 1 prescribes a linear distribution of Stokeslets, the fundamental solutions of the Stokes equation, along the center-line of the body along with a distribution of image singularities below the plane in order to satisfy a no-slip condition at the plane. In the case of a straight rod sweeping an upright cone, we found that this strength distribution is prescribed as $\boldsymbol{\alpha}(s) = \frac{\omega\epsilon\sin\kappa}{2}(0, s, 0)$ where ω is the angular speed of the rod, ϵ is the slenderness parameter, κ is the angle which the rod is tilted from the positive z-axis, and $0 \leq s \leq \ell$. This strength distribution implies that the effects of the rod on the fluid flow will be neglible near the base of the rod (since s is small). However, if we are to view the rod as a continuum of spheres along a center-line, the region near the base is one where the velocity gradients and pressure are large.

To understand the effects of the base of the rod, we analyze the case of a sphere translating very near a plane in a viscous fluid. This problem may be analyzed from the point of view of lubrication theory as examined by O'Neill & Stewartson [**12**]. We then may study the problem of a sphere precessing a circle of fixed radius at a fixed, small height above a plane by considering the motion as being piecewise translation. Once the velocity field is recovered in this problem, we may numerically integrate to find particle trajectories. These trajectories may be directly compared to those obtained by the singularity solution for a sphere in a similar background flow, where the solution is given by a single Stokeslet and point-source dipole with corresponding image singularites to enforce the no-slip condition on the plane.

5.1. A sphere translating parallel to a plane: a lubrication approach

We first must understand the results presented by O'Neill & Stewartson. We examine the problem of a rigid sphere of radius a translating uniformly near a plane wall with clearance ϵa, where ϵ is unrelated to the previous definition throughout the thesis. A schematic of this problem is shown in Figure 5.1.

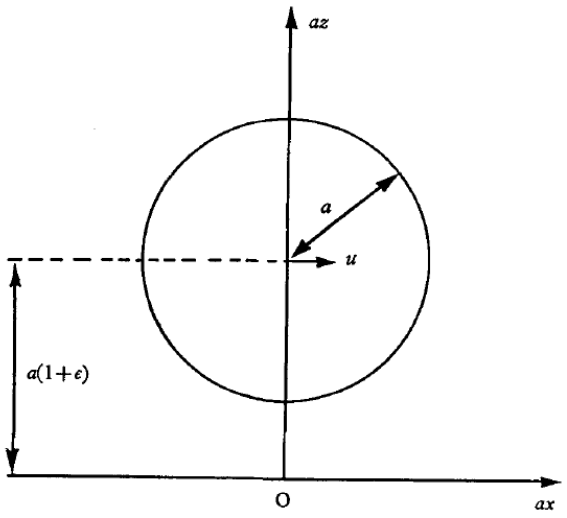

FIGURE 5.1. Problem sketch (O'Neill & Stewartson).

A matched asymptotic approach is used where an 'inner' solution is built for a region near the points closest to O. In this region, the leading order terms of the asymptotic expansion satisfy the classical equations of lubrication theory. A matching 'outer' solution is then constructed which is valid in the remainder of the fluid where it is possible to assume $\epsilon = 0$ [**12**]. If we assume the sphere has radius a and is moving with a uniform velocity $(U, 0, 0)$, the center of the sphere will be located at $(0, 0, a(1+\epsilon))$ instantaneously. Further, we assume that all conditions of Stokes flow are met, and thus the governing equations for the fluid flow are

$$\nabla p = \nabla^2 \mathbf{V}$$

$$\text{div}\mathbf{V} = 0$$

where p is the pressure and $\mathbf{V}$ is the velocity. The boundary conditions are that $\mathbf{V} \to 0$ at infinity and $\mathbf{V} = 0$ on the plane. The method followed by O'Neill & Stewartson considers a transformation into cylindrical polar coordinates (ar, θ, az), where at any point on the sphere the velocity components (u, v, w) of $\mathbf{V}$ are given by

$$\begin{aligned} u &= U\cos\theta \\ v &= -U\sin\theta \\ w &= 0 \end{aligned}$$

The flow region is then divided into a region where both r and z are small, and a region in which we may assume that $\epsilon = 0$ where the solution is found in terms of Bessel functions.

In the inner region the boundary conditions, as well as our assumption of small r and z, are exploited to discern the order of the expressions for $P(r,z),\ U(r,z),\ V(r,z)$, and $W(r,z)$. By considering each component of the equation $\nabla p = \nabla^2\mathbf{V}$, we find that

$$\begin{aligned} P(r,z) &\sim \epsilon^{-\frac{3}{2}}\frac{6R}{5H^2} + O(\epsilon^{-\frac{1}{2}}) \\ U(r,z) &\sim \frac{6-9R^2}{10H^3}Z^2 + \frac{2+7R^2}{5H^2}Z + O(\epsilon) \\ V(r,z) &\sim -\frac{3}{5H^2}Z^2 - \frac{2}{5H}Z + O(\epsilon) \\ W(r,z) &\sim \epsilon^{\frac{1}{2}}\left(\frac{8R-2R^3}{5H^4}Z^3 + \frac{2R^3-7R}{5H^3}Z^2\right) + O(\epsilon^{\frac{3}{2}}) \end{aligned}$$

where $R = \epsilon^{-\frac{1}{2}}r,\ Z = \epsilon^{-1}z$, and $H = 1 + \frac{1}{2}R^2$ (OS67).

In the outer region, the flow is still governed by the same equations, which are satisfied the pressure and cylindrical velocity components are of the form

$$\begin{aligned} ap &= 2\mu UQ\cos\theta, \quad u = U\left[rQ + \frac{1}{2}(\psi+\chi)\right]\cos\theta, \\ v &= \frac{1}{2}U\left[\chi-\psi\right]\sin\theta, \quad w = U\left[zQ+\phi\right]\cos\theta \end{aligned}$$

where $\psi,\ \chi,\ \phi$ and Q are functions of r and z satisfying

$$L_0^2\psi = L_2^2\chi = L_1^2\phi = L_1^2 Q = 0$$

where

$$L_m^2 \equiv \frac{\partial^2}{\partial r^2} + \frac{1}{r}\frac{\partial}{\partial r} - \frac{m^2}{r^2} + \frac{\partial^2}{\partial z^2}$$

The boundary conditions require

$$\phi + zQ = 0, \quad \chi + rQ = 0, \quad \psi + rQ = 0$$

on the plane, and

$$\phi + zQ = 0, \quad \chi + rQ = 0, \quad \psi + rQ = 2$$

on the surface of the sphere. In order to find the solution in this outer region, we follow the suggestion of O'Neill and Stewartson, and transform the coordinates $r,\ z$ to coordinates ξ, η by

$$r = \frac{2\eta}{\xi^2 + \eta^2}, \quad z = \frac{2\xi}{\xi^2 + \eta^2}$$

In these coordinates, the plane is given by $\xi = 0$, the boundary of the sphere by $\xi = 1$, the origin by $\eta = \infty$, and infinity by $\xi = \eta = 0$. This transformation requires that we transform the operator L_m^2 into these coordinates. In these coordinates, the operator may be presented as

$$\begin{aligned} L_m^2 \ = \ & \frac{1}{4}\left[(\xi^2+\eta^2)^2\frac{\partial^2}{\partial\eta^2} + \frac{\xi^4-\eta^4}{\eta}\frac{\partial}{\partial\eta} - 2\xi(\xi^2+\eta^2)\frac{\partial}{\partial\xi} - \frac{m^2(\xi^2+\eta^2)^2}{\eta^2}\right. \\ & \left. +(\xi^2+\eta^2)^2\frac{\partial^2}{\partial\xi^2}\right] \end{aligned}$$

To find the solutions of $L_m^2 f = 0$, we assume $f(\eta, \xi) = (\xi^2 + \eta^2)^p X(\xi) H(\eta)$ and seek a separable solution. Applying the operator to this function gives us that $p = \frac{1}{2}$ and

$$L_m^2 f = \frac{(\xi^2 + \eta^2)^{5/2}(\eta X(H' + \eta H'') + H(-m^2 X + \eta^2 X''))}{4\eta^2}$$

We then multiply by $\frac{4}{(\xi^2+\eta^2)^2} \frac{1}{f(\eta,\xi)}$ to obtain the equation

$$\frac{H' + \eta H''}{\eta H} - \frac{m^2}{\eta^2} + \frac{X''}{X} = 0$$

which is now separable. We let $\frac{X''}{X} = c^2$, thus $X(\xi) = A\sinh(c\xi) + B\cosh(c\xi)$. The above equation then simplifies to

$$\eta^2 H'' + \eta H' + H(c^2\eta^2 - m^2) = 0$$

whose solution is the Bessel function $J_m(c\eta)$. We then may construct the full solution for $0 \leq s \leq \infty$ as

$$f(\eta, \xi) = (\xi^2 + \eta^2)^{1/2} \int_0^\infty \left(A(s)\sinh(s\xi) + B(s)\cosh(s\xi)\right) J_m(s\eta) ds$$

where $A(s)$ and $B(s)$ are function such that the integral converges. Again remembering our transformation of variables, we must now assume we occupy a region such that the inner and outer solutions are valid. Matching in this region requires

$$\epsilon^{\frac{1}{2}} R \sim \frac{2}{\eta}.$$

and the boundary conditions imply that $\phi \sim -\frac{3}{5}\xi\eta$ for large values of η. With $L_1^2\phi = 0$, the solution is of the form

$$\phi = (\xi^2 + \eta^2)^{1/2} \int_0^\infty A(s)\sinh(s\xi) J_1(s\eta) ds$$

where the large η asymptotics dictate that $A(s) \sim -\frac{3}{5s^2}$ for small s and exponentially small for large s. The boundary conditions on the plane and the sphere give a relation between Q and ϕ, and we use these conditions to state $Q = Q_0 + \frac{3}{10}Q_1$ where

$L_1^2 Q_0 = L_1^2 Q_1 = 0$ and

$$\begin{aligned} Q_0 &= \frac{1}{2}(\xi^2+\eta^2)^{1/2} \int_0^\infty \left(B\cosh(s\xi) + C\sinh(s\xi)\right) J_1(s\eta) ds \\ Q_1 &= \eta(\xi^2+\eta^2) + (\xi^2+\eta^2)^{1/2} \int_0^\infty V_1(s,\xi) J_1(s\eta) ds \end{aligned}$$

where

$$\begin{aligned} B &= sA'' + A' - \frac{A}{s} + \frac{9}{5s^3} \\ C &= (sA'' - A')K + \frac{9}{5}\frac{e^{-s}-1}{s^3} \\ V_1 &= e^{-s\xi}\left(\frac{\xi^2}{s} + \frac{3\xi}{s^2}\right) - \frac{3e^{-s}\sinh(s\xi)}{s^3} \\ K &= \frac{1}{s} - \coth s \end{aligned}$$

We may construct the remaining functions similarly. $\chi = \chi_0 + \frac{3}{5}\chi_1$ where

$$\begin{aligned} \chi_0 &= (\xi^2+\eta^2)^{1/2} \int_0^\infty \left(F\cosh(s\xi) + G\sinh(s\xi)\right) J_2(s\eta) ds \\ \chi_1 &= -\eta^2 + (\xi^2+\eta^2)^{1/2} \int_0^\infty V_2(s,\xi) J_2(s\eta) ds \end{aligned}$$

where

$$\begin{aligned} F &= A - sA' + \frac{9}{5s^2} \\ G &= (2A - sA')K - \frac{9}{5s^2} \\ V_2 &= e^{-s\xi}\left(\xi^2 + \frac{3\xi}{s}\right) \end{aligned}$$

Finally, $\psi = \psi_0 + \frac{3}{5}\psi_1$ where

$$\begin{aligned} \psi_0 &= (\xi^2+\eta^2)^{1/2} \int_0^\infty \left(D\cosh(s\xi) + E\sinh(s\xi)\right) J_0(s\eta) ds \\ \psi_1 &= -\eta^2 + (\xi^2+\eta^2)^{1/2} \int_0^\infty V_0(s,\xi) J_0(s\eta) ds \end{aligned}$$

where

$$\begin{aligned} D &= sA' + A - \frac{3}{5s^2} \\ E &= sA'K - \frac{3}{5}\frac{e^{-s}-1}{s^2} + 2(\coth s - 1) \\ V_0 &= e^{-s\xi}\left(\xi^2 + \frac{3\xi}{s}\right) + \frac{e^{-s}\sinh(s\xi)}{s^2} \end{aligned}$$

We notice that if we have the function $A(s)$, this problem may be completed. It can be shown from the continuity equation that $A(s)$ satisfies the follow differential equation

$$s^3K'A'' + sA'\left[s^2K'' + 3sK' + 2K\right] - A\left[s^2K'' + 4sK' + 2K\right] + s^2X'' = 0$$

where $K = \frac{1}{s} - \coth s$ and $X = \coth s - 1$. We find the asymptotics for this solution by examining the above equation for small and large values of s. For small s, the equation becomes

$$A'' + \frac{5}{s}A' - \frac{6}{s^2}A - \frac{6}{s^4} = 0$$

The solutions to the homogeneous equation are $s^{-2\pm\sqrt{10}}$, and the particular solution is given as $-\frac{3}{5s^2}$. The particular solution satisfies the desired asymptotics for small s, so we must reject the solution $s^{-2-\sqrt{10}}$ since it violates these asymptotics. For large s, the equation becomes

$$A'' + \left(2 - \frac{1}{s}\right)A' - \frac{2}{s}A - 8se^{-2s} = 0$$

The solutions to the homogeneous equation in this case are given by e^{-2s} and $1-2s$, and the particular solution is given by $-2s^2e^{-2s}$, which defines the large s asymptotics.

5.1.1. Constructing $A(s)$. To construct the solution to this differential equation for all s, we seek two separate Frobenius solutions: a solution A_1 to the homogeneous equation, and a solution A_2 to the particular solution. The full solution may then be represented as $A = cA_1 + A_2$ for some constant c which we find to satisfy the required

asymptotics. We represent the differential equation as

$$A'' + \frac{p(s)}{s}A' + \frac{q(s)}{s^2}A + \frac{h(s)}{s^4} = 0$$

where

$$\begin{aligned}
\frac{p(s)}{s} &= \frac{K''}{K'} + \frac{3}{s} + \frac{2K}{s^2K'} \\
\frac{q(s)}{s^2} &= -\frac{K''}{sK'} - \frac{4}{s^2} - \frac{2K}{s^3K'} \\
\frac{h(s)}{s^4} &= \frac{X''}{sK'}
\end{aligned}$$

The Frobenius solution to the homogeneous equation is then given by

$$A_1(s) = s^\alpha \sum_{n=0}^{\infty} a_{2n}s^{2n}$$

since it can be shown that the series expansions for $p(s)$, $q(s)$, and $h(s)$ contain only even powers of s. It can also be shown that for $n > 0$ that $q_{2n} = -p_{2n}$. We may then represent these series as the following

$$\begin{aligned}
p(s) &= p_0 + \sum_{n=1}^{\infty} p_{2n}s^{2n} \\
q(s) &= q_0 - \sum_{n=1}^{\infty} p_{2n}s^{2n} \\
h(s) &= \sum_{n=0}^{\infty} h_{2n}s^{2n}
\end{aligned}$$

According to the method of Frobenius, we may construct the coefficients for our solution A_1 by first solving for α as the root of the indicial polynomial $\alpha^2 + (p_0 - 1)\alpha + q_0$. With $p_0 = 5,\ q_0 = -6$, we find that $\alpha = -2 \pm \sqrt{10}$. We only keep the positive root in order to satisfy the correct small s asymptotics. By the moethod of

Frobenius, the coefficients in the solution are defined recursively as

$$\begin{aligned} a_{2n} &= \frac{-\sum_{k=0}^{n-1} p_{2(n-k)}(1-\alpha-2k)a_{2k}}{(\alpha+n)^2+(p_0-1)(\alpha+n)+q_0} \\ &= \frac{\sum_{k=0}^{n-1} p_{2(n-k)}(2k+\sqrt{10})-3)a_{2k}}{(-2+\sqrt{10}+n)^2+4(-2+\sqrt{10}+n)-6} \end{aligned}$$

Similarly, the particular solution A_2 may be constructed as

$$A_2(s) = s^{-2}\sum_{n=0}^{\infty} b_{2n}s^{2n}$$

where $\alpha = -2,\ b_0 = -\frac{3}{5}$ in order to match the desired small s asymptotics and

$$\begin{aligned} b_{2n} &= \frac{-h_{2n}-\sum_{k=0}^{n-1} p_{2(n-k)}(1-\alpha-2k)a_{2k}}{(\alpha+n)^2+(p_0-1)(\alpha+n)+q_0} \\ &= \frac{-h_{2n}+\sum_{k=0}^{n-1} p_{2(n-k)}(2k-3)a_{2k}}{(n-2)^2+4(n-2)-6} \end{aligned}$$

These solutions, however, do not have an infinite radius of convergence. To find the radius of convergence for each of these solutions, we examine the zeros in the complex plane for the following series as the number of coefficients increases.

$$\begin{aligned} s^{2-\sqrt{10}}A_1(s) &= \sum_{n=0}^{\infty} a_{2n}s^{2n} \\ s^2 A_2(s) &= \sum_{n=0}^{\infty} b_{2n}s^{2n} \end{aligned}$$

For the first series, we retain 10 and then 80 terms and plot the zeros in the complex plane. This is shown in Figures 5.2 and 5.3.

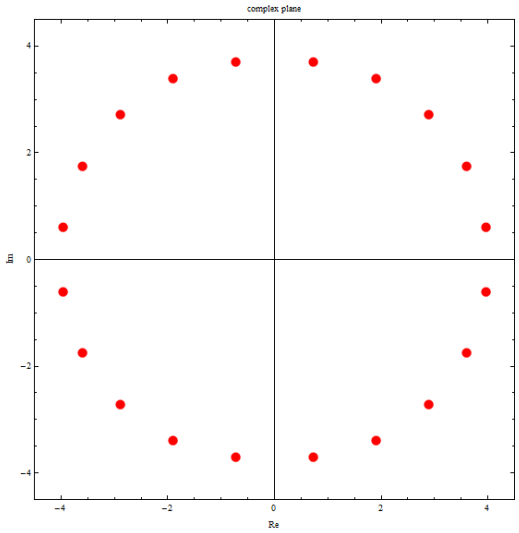

FIGURE 5.2. Zeros for $N = 10$.

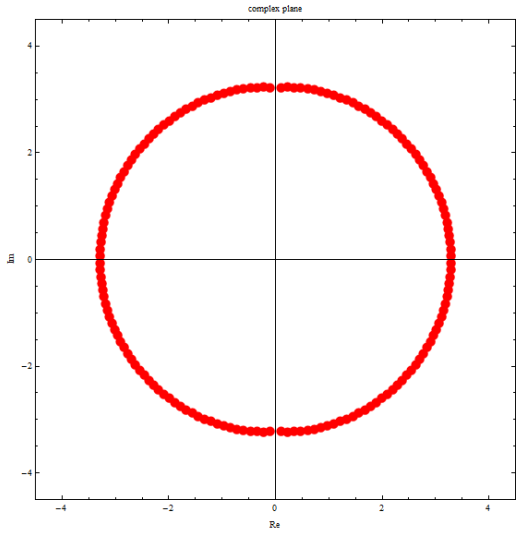

FIGURE 5.3. Zeros for $N = 80$.

The minimum modulus of these zeros is 3.76938 for $N = 10$ and 3.21249 for $N = 80$. Similarly, we may examine the zeros of the second series where we retain 10 and then 80 terms in Figures 5.4 and 5.5.

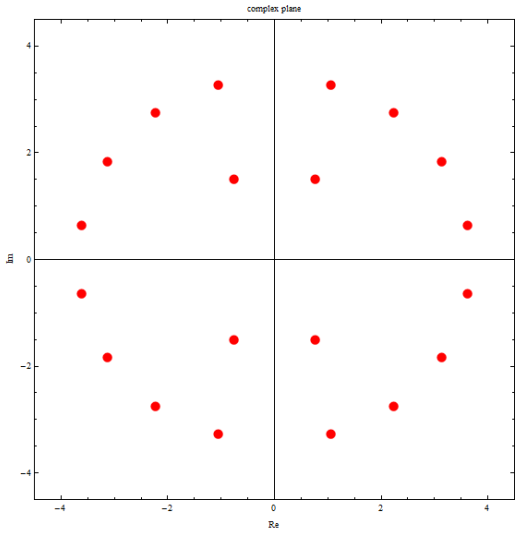

FIGURE 5.4. Zeros for $N = 10$.

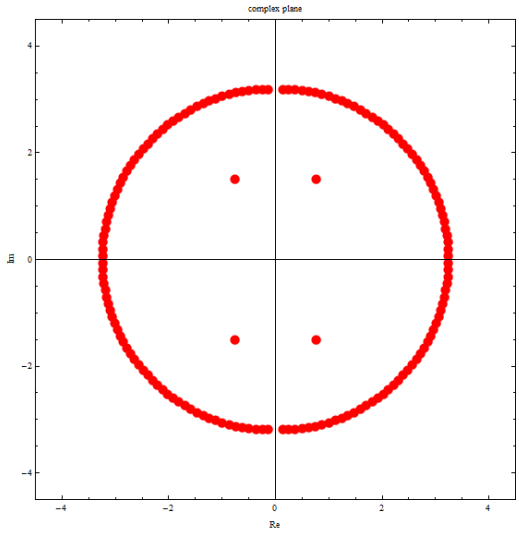

FIGURE 5.5. Zeros for $N = 80$.

The minimum modulus of these zeros is 1.68348 for both $N = 10$ and $N = 80$. The radius of convergence of the solution is given by the nearest singularity in the

coefficients of the differential equation, and this series examination shows that for an increasing number of terms, we approach this value.

This calculation is useful however if we instead search for a numerical solution to the differential equation. Since the series is convergent for small s, we may use the values of the homogeneous and particular solutions, as well as their derivatives, away from $s = 0$ as an input into a numerical solver. Specifically, we find a numerical solution to both the homogeneous and non-homogeneous equations on an interval from $0.05 \leq s \leq 5.6$, and then find a multiple of the homogeneous solution such that the full solution satisfies the desired asymptotics for small and large s. Figures 5.6 and 5.7 show these solutions.

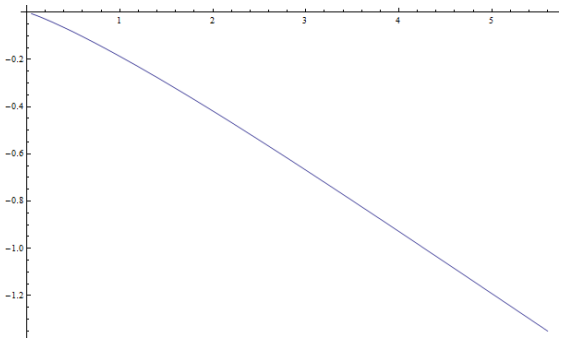

FIGURE 5.6. Numerical homogeneous solution.

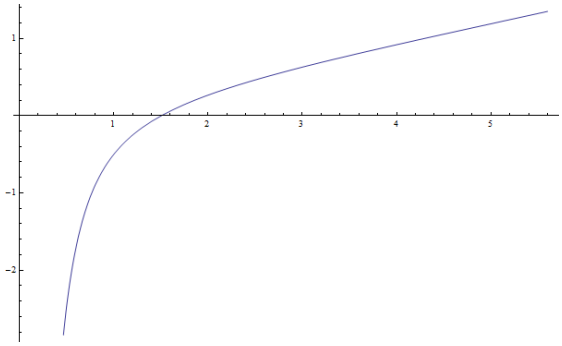

FIGURE 5.7. Numerical particular solution.

The multiple of the homogeneous solution which satisfies the asymptotic limits $A \sim -\frac{3}{5s^2}$ for small s and $A \sim -2s^2e^{-2s}$ for large s is found to be 0.18629. The full solution is shown in Figure 5.8.

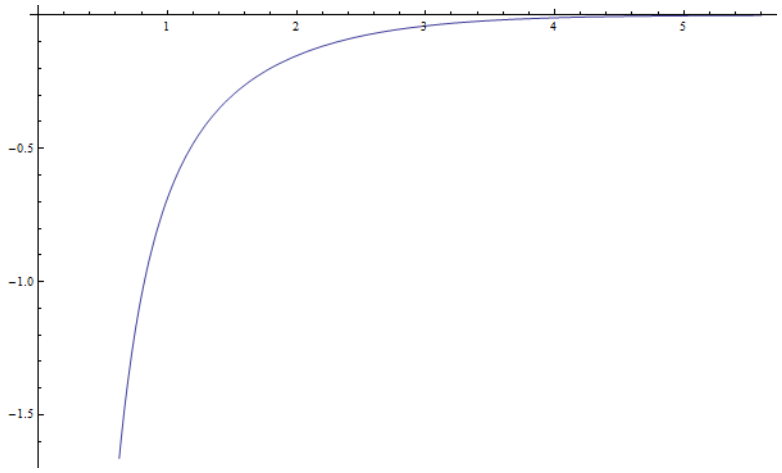

FIGURE 5.8. Full solution on the interval $0.05 \leq s \leq 5.6$.

We may compare the values of our numerical solution with those of the desired asymptotics at the endpoints to show the accuracy of matching. At the left endpoint we have

$$\begin{aligned} A(0.05) &= -240.231 \\ -\frac{3}{5s^2}\bigg|_{s=0.05} &= -240 \end{aligned}$$

which is an error of 0.1%. At the right endpoint we have

$$\begin{aligned} A(5.6) &= -0.000871 \\ -2s^2e^{-2s}\big|_{s=5.6} &= -0.000857 \end{aligned}$$

which has an error of 1.5%.

This numerical solution is differentiable, and may be substituted for A into the expressions for $\phi,\ Q,\ \psi$, and χ in order to obtain the velocity field (u, v, w) at a point (η, ξ) in the transformed coordinates. This velocity field in cylindrical coordinates may then be integrated numerically to find particle trajectories. A criterion must then be established which tells us when to move from the outer solution to the inner. This will enable us to obtain particle trajectories originating far from the sphere which may pass near or under the sphere. A direct comparison is currently underway

between particle trajectories generated using the lubrication theory and the singularity methods found in Happel & Brenner [**9**], and an example of a few trajectories generated using the lubrication theory is seen in Figure 5.9 [**3**].

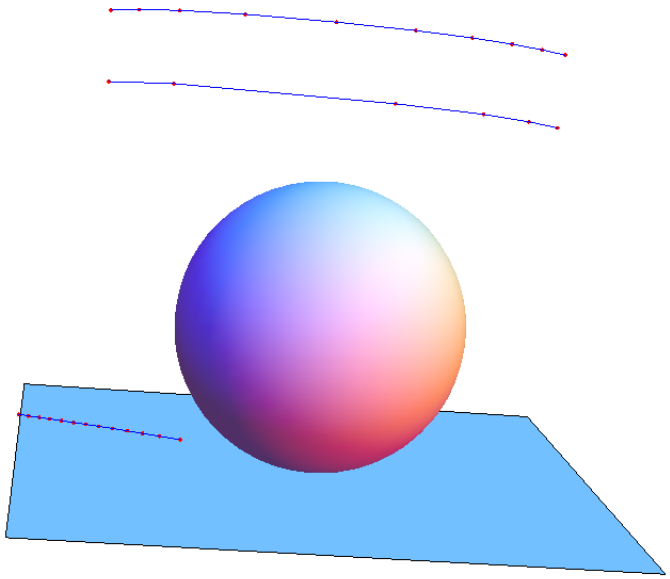

FIGURE 5.9. A few trajectories for a sphere of radius 1 in a background flow $\mathbf{U} = (1, 0, 0)$.

As a first-order qualitative comparison, we may examine a few trajectories created by a single Blakeslet in Figure 5.10.

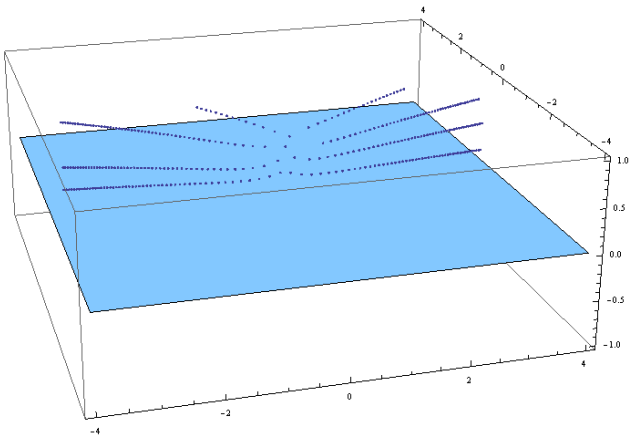

FIGURE 5.10. A few trajectories for a Blakeslet.

The effect of the plane is clear when we plot the free space solution for a sphere embedded in a uniform flow $\mathbf{U} = (1, 0, 0)$ at infinity. The solution is represented as a Stokeslet and source dipole located at the center of the sphere. In this particular example, the sphere has radius 1. Several trajectories are seen in Figure 5.11.

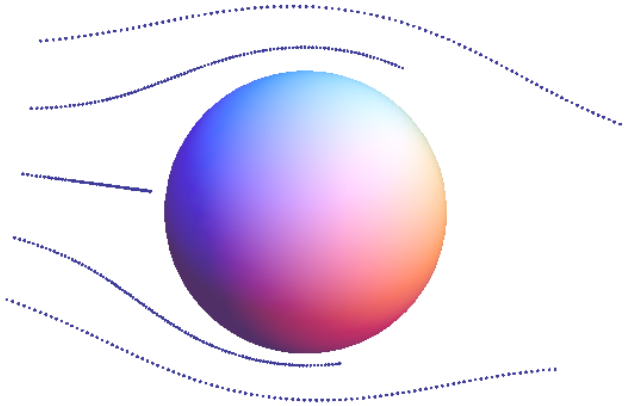

FIGURE 5.11. Free-space particle trajectories for sphere embedded in uniform flow.

The behavior of Lagrangian trajectories in this case is in stark contrast to their behavior given a single reflection. To see this, we consider the problem of two spheres translating perpendicular to the segment which joins their centers. Here, I have kept the same singularity strengths in the Stokeslet and source dipoles as the free space solution. The behavior of the particle trajectories is highly dependent on the separation distance between the spheres, and if the spheres are too close, there is a blocking phenomenon where the particle trajectories must deflect around the sphere [**3**]. This behavior can been seen in Figures 5.12 and 5.13

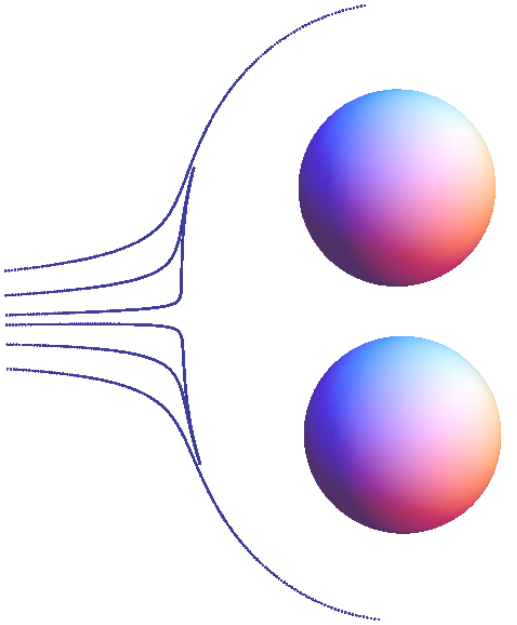

FIGURE 5.12. Two spheres of radius 1 whose centers are separated by a distance of 2.5 units.

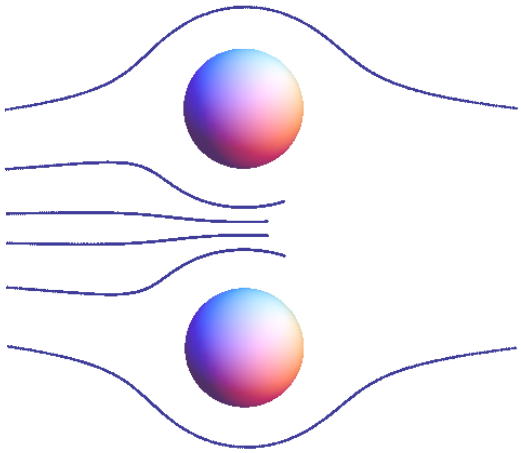

FIGURE 5.13. Two spheres of radius 1 whose centers are separated by a distance of 4 units.

5.2. A far-field comparison

Since the fluid theory involves a distribution of Blakeslets, we may then examine the far-field flow to due to a single Blakeslet and compare this to the far-field flow from the lubrication theory [**3**]. The outer solution may be recovered from the lubrication theory in cylindrical coordinates in the limit of fixed z for $r \to \infty$. This limit may be examined for the lubrication theory, and yields the far-field behavior

$$\begin{aligned} u &= U\cos\theta\frac{24}{5r^2} \\ v &= U\sin\theta\frac{24}{5r^2} \\ w &= -U\cos\theta\frac{12z}{5r^3} \end{aligned}$$

The far-field flow for a single Blakeslet with a force component in the x-direction where the singularity is located at a height of h above the plane is given by Blake [**1**] as

$$\begin{aligned} u &= \frac{F_1}{8\pi\mu}\frac{12hz}{r^3} \\ v &= \frac{F_1}{8\pi\mu}\frac{12hz}{r^3} \\ w &= \frac{F_1}{8\pi\mu}\frac{12hz^2}{r^4} \end{aligned}$$

This theory, along with the theory presented in O'Neill [**13**] concerning linear shear flow past a plane with a cylindrical trough will be of particular interest in our understanding the fluid flow near the base of the rod.

CHAPTER 6

Conclusions and future work

I have sought to answer two distinct questions with the work presented in the previous chapters. The first of these questions, addressed in chapter 2 concerns the finding of the position of the rod given only the intrinsic parameters of the fluid and magnetic systems. I have shown that given an external magnetic field $\mathbf{B_0}$, this question reduces to a static problem (after all initial transients have cleared) which can then be solved analytically for the case of a straight rod driven by a uniform external field, and numerically for linear background fields and a prescribed bent rod geometry. In the former case, I have also shown that the solution we obtain for the rod orientation is unique within certain limits of the background magnetic field angle θ and the non-dimensionalized constant λ which is a ratio of the fluid and magnetic field influence in the static problem. This theory helps us understand the role of magnetically driven ciliary models, which may be micro- or macro-scale.

The second question, addressed in chapters 3 and 4, concerns the accurate resolution of the flow field and particle trajectories given a prescribed motion of the rod. As was shown from Lagrangian particle tracking, the current theory underpredicts the motion of a particle in such flows. This neccessitated a better understanding of the flows in the experiment, which was the motivation for adopting the Eulerian PIV approach, where we could examine the fully 3-dimensional velocity field in a plane just above the rod tip. The PIV experiments allowed us to see several features of the flow and quantitatively measure the vertical transport using both local and broader metrics. This technique proved invaluable when a study of the free-surface was performed, as it showed us that possibly large differences in the vertical transport occur

when this free-surface height is changed. Further, it lead to a re-examination of the current theory to take into account the free-surface. Future work in this area will include another set of free-surface experiments to corroborate the current data, as well as a consideration of wall effects on the fluid flow.

In chapter 5, an ancillary problem of a sphere at a small, fixed height above a no-slip plane is considered. This problem aides in the understanding of the role which the base of the rod plays in determining the fluid flow near the plane given that the current slender body theory is not valid near the rod base. Futhermore, an understanding of the far-field flow in such a setting provides a justification for neglecting these lubrication effects for points away from the plane.

The ciliary models discussed within, along with their future corrections, would extend very well to elastic rods with small curvature. These rods may also be manufactured in a way that allows for magnetic driving, which would preserve aspects of the current magnetic slender body theory. Also of interest in the future is an extension of these models which would better mimic the biological setting from which they were derived - namely an examination of such models in non-Newtonian fluids. I am particularly interested in the future work of fluid theory and experimentation for multiple-cilia models.

Appendix A: Matlab Programs

A.1. Read text files output from PIV

```
files = dir('*.txt');
NumFiles = length(files);
N = 68*102; % number of velocity entries - need to make dynamic

% initialize velocity vectors and skewness vectors
vX = zeros(N,NumFiles); vY = vX; vZ = vX;
% skewX = zeros(NumFiles,1); skewY = skewX; skewZ = skewX;

tic
for i=1:NumFiles %should be NumFiles
    fid = fopen(files(i).name); % opens ith file
    strData = textscan(fid,...
        '%s%s%s%s%s','Delimiter','\t','headerLines',1);

    for j=1:N
        strZ = strData{5}(j); % cell {5} is vZ
        new_str = strrep(strZ, ',', '.');
        vZ(j,i) = 1000*str2double(new_str);

        strX = strData{3}(j); % cell {3} is vX
        new_str = strrep(strX, ',', '.');
        vX(j,i) = 1000*str2double(new_str);

        strY = strData{4}(j); % cell {4} is vY
        new_str = strrep(strY, ',', '.');
```

```
        vY(j,i) = 1000*str2double(new_str);

%         strXc = strData{1}(j); % cell {1} is Xcoord
%         new_str = strrep(strXc, ',', '.');
%         Xcoord(j,i) = str2double(new_str);
%
%         strYc = strData{2}(j); % cell {2} is Ycoord
%         new_str = strrep(strYc, ',', '.');
%         Ycoord(j,i) = str2double(new_str);
    end

    fclose(fid);
end
toc

% save('Xcoord','Xcoord')
% save('Ycoord','Ycoord')
save('NumFiles','NumFiles')
save('vX','vX')
save('vY','vY')
save('vZ','vZ')
```

A.2. Find centroids, orientations, and vertical velocity along slices

```
N = 102; M = 68;

Vtot = zeros(N,M,NumFiles); % in plane speed used for peanut finding
maxes = zeros(NumFiles,1); % stores max in-plane speed for each frame
B = Vtot; % logical matrix from thresholding
Centroids = zeros(NumFiles,2); % centers of peanuts
```

```
Orientations = zeros(NumFiles,1); % peanut orientation

maxZs = zeros(NumFiles,1); % max vert velocity slice through peanut
minZs = maxZs; % min vert velocity for same slice
Zslice = zeros(NumFiles,101); % keeps whole slice for each frame
Xslice = Zslice;
Yslice = Zslice;

for i=1:NumFiles

    % reshape velocity arrays into matrices
    reVx = reshape(vX(:,i),N,M);
    reVy = reshape(vY(:,i),N,M);
    reVz = reshape(vZ(:,i),N,M);

    % find in-plane velocity for peanut
    for j = 1:N
        for k=1:M
            Vtot(j,k,i) = sqrt(reVx(j,k)*reVx(j,k) +...
                reVy(j,k)*reVy(j,k));
        end
    end

    maxes(i) = max(max(Vtot(:,:,i)));
    B(:,:,i) = Vtot(:,:,i)>0.667*maxes(i); %threshold
    STATS = regionprops(B(:,:,i),'all');
    Centroids(i,:) = STATS.Centroid;
    Orientations(i) = STATS.Orientation;
```

```
tempOrient = pi/180*Orientations(i);
L = 39; %STATS.MajorAxisLength;
xL = cos(tempOrient)*4*L/3;
h = xL/100;
x = Centroids(i,1)-xL/2:h:Centroids(i,1)+xL/2;

tempSlope = sin(tempOrient)/cos(tempOrient);
y = zeros(1,length(x));
tempZ = zeros(1,length(x));
tempX = tempZ; tempY = tempZ;

for j=1:length(x)
    y(j) = Centroids(i,2) - tempSlope*(x(j)-Centroids(i,1));
    tempX(j) = interp2(reVx,x(j),y(j));
    tempY(j) = interp2(reVy,x(j),y(j));
    tempZ(j) = interp2(reVz,x(j),y(j));
end

if i==7
    hold on; axis equal
    contour(Vtot(:,:,i),0.667*maxes(i),'blue')
    plot(x,y,'red')
    plot(Centroids(i,1),Centroids(i,2),'bo')
end

Xslice(i,:) = tempX; %contains peanut slice for each frame
Yslice(i,:) = tempY;
Zslice(i,:) = tempZ;
```

```
    minZs(i) = min(tempZ);
    maxZs(i) = max(tempZ);
end

% fits circle to centroids
[CenterOfRotation,RotRadius] = fitcircle(Centroids);

% fit ellipse to centroids to check uprightness of cone
ellipse = fit_ellipse(Centroids(:,1),Centroids(:,2));
if ellipse.a>ellipse.b
    eccent = sqrt(1-(ellipse.b)^2/(ellipse.a)^2);
else
    eccent = sqrt(1-(ellipse.a)^2/(ellipse.b)^2);
end

save('Centroids','Centroids')
save('Orientations','Orientations')
save('Xslice','Xslice')
save('Yslice','Yslice')
save('Zslice','Zslice')
save('ellipse','ellipse')
save('minZs','minZs')
save('maxZs','maxZs')
save('Vtot','Vtot')
```

A.3. Find and plot particle trajectories from PIV data

```
[Cen,Rad]=fitcircle(Centroids);
PIX2MM = .4632; % mm/pix
h = 2/5;
```

```
N = 102; M = 68;
x = Cen(1)+10*(4.0044292e-01)/PIX2MM;
y = Cen(2)+10*(8.0062255e-04)/PIX2MM;
p = ones(2,299);
p(1,:) = x*ones(1,299);
p(2,:) = y*ones(1,299);
InstSpeed = zeros(1,298);
InstSpeedTwo = zeros(1,298);

for i=3:299-1
    reVx = reshape(vX(:,i),N,M);
    reVy = -reshape(vY(:,i),N,M);

    a1 = interp2(reVx,p(1,i),p(2,i));
    a2 = interp2(reVy,p(1,i),p(2,i));

    b1 = interp2(reVx,p(1,i)+h/2*a1,p(2,i)+h/2*a1);
    b2 = interp2(reVy,p(1,i)+h/2*a2,p(2,i)+h/2*a2);

    c1 = interp2(reVx,p(1,i)+h/2*b1,p(2,i)+h/2*b1);
    c2 = interp2(reVy,p(1,i)+h/2*b2,p(2,i)+h/2*b2);

    d1 = interp2(reVx,p(1,i)+h*c1,p(2,i)+h*c1);
    d2 = interp2(reVy,p(1,i)+h*c2,p(2,i)+h*c2);

    a = [a2 a1]';
    b = [b2 b1]';
    c = [c2 c1]';
```

```
    d = [d2 d1]';

    p(:,i+1) = p(:,i) + h/6*(a+2*b+2*c+d);

    InstSpeedTwo(i) = norm(1/6*(a+2*b+2*c+d));
end

hold on
p(1,:) = PIX2MM*(p(1,:) - ones(1,299)*Cen(1));
p(2,:) = PIX2MM*(p(2,:) - ones(1,299)*Cen(2));
plot(p(1,:),p(2,:)); axis equal; grid on

Cent(:,1) = PIX2MM*(Centroids(:,1) - ones(299,1)*Cen(1));
Cent(:,2) = PIX2MM*(Centroids(:,2) - ones(299,1)*Cen(2));
plot(Cent(:,1),Cent(:,2),'bo'); axis equal; grid on
```

A.4. Find average vertical velocity along circles of varying radius

```
NumFiles=299;
N = 100; % number of points along each circle
numR = 50;
Rstep = 0.5;

[CenterOfRotation,RotRadius] = fitcircle(Centroids);
MV = 102;
NV = 68;

meanZcircle = zeros(NumFiles,numR);
MeanMean = zeros(numR,1);
StdMeans = MeanMean;
```

```
x = zeros(N,1);
y = x;
temp = x;
Rs = (Rstep:Rstep:Rstep*numR)';

for j=1:numR

    % define circle of radius Rstep*j around rotation center
    for i=1:N
        x(i) = CenterOfRotation(1) + Rstep*j*cos(2*pi*(i-1)/N);
        y(i) = CenterOfRotation(2) + Rstep*j*sin(2*pi*(i-1)/N);
    end

    % for each frame, find z-velocities around given circle
    for i=1:NumFiles
        redoneZ = reshape(vZ(:,i),MV,NV);
        % reshape z-velocity vectors into matrix
        temp = interp2(redoneZ,x,y);
        % interpolate this matrix on circle
        meanZcircle(i,j) = mean(temp);
        % take mean of values on circle
    end

    MeanMean(j) = mean(meanZcircle(:,j));
    StdMeans(j) = std(meanZcircle(:,j));
end

%convert Rs to mm by factor of .4639 mm/pix
```

```
Pix2MM = .4632;
hold on
grid on
plot(Pix2MM*Rs,MeanMean,'blue')
plot(Pix2MM*Rs,zeros(size(Rs)),'red')
hold off

interp1(Pix2MM*Rs,MeanMean,Pix2MM*RotRadius)

save('MeanMean','MeanMean')
```

A.5. Main rod tracking program

```
frameI=4050;
nF=77*2; % one orbit is around 77 frames

movR=aviread('Cam8481078_9Dec10Take0_clockwise_...
    0to20_fps15_rpm12_df1_crop',frameI:frameI+nF);
movL=aviread('Cam8481100_9Dec10Take0_clockwise_...
    0to20_fps15_rpm12_df1_crop',frameI:frameI+nF);
maxind=length(movR);

addpath('TOOLBOX_calib')
load('Calib_Results_stereoNewSiliconeOil')

regionL = [515 515+158; 400 400+149];
regionR = [515 515+153; 625 625+149];

yminR = regionR(1,1); ymaxR = regionR(1,2);
xminR = regionR(2,1); xmaxR = regionR(2,2);
```

```
yminL = regionL(1,1); ymaxL = regionL(1,2);
xminL = regionL(2,1); xmaxL = regionL(2,2);

kappavecC=zeros(maxind,1); phivecC=kappavecC;
basevecC=zeros(3,maxind); topvecC=basevecC;
kappavecCm=kappavecC; phivecCm=kappavecC;

for k=1:maxind

imR = movR(k).cdata;
imL = movL(k).cdata;
imR2=im2double(imR); imR2=imR2(:,:,3);
imL2=im2double(imL); imL2=imL2(:,:,3);

% contour levels manually set
figure(1)
ContL=contour(imL2,0.7,'red');
figure(2)
ContR=contour(imR2,0.45,'red');

% find xtremepix (base, 2 top pix) and pass
% back all info for debugging
% suffix "t" stands for pixel translated correctly
[xtremepixL xtremepixLt]=RMX_Contour_Pix(ContL,xminL,yminL);
[xtremepixR xtremepixRt]=RMX_Contour_Pix(ContR,xminR,yminR);

% find top, bottom 3D coords - use right frame to match LHZ
[topL topR]=stereo_triangulation(0.5*(xtremepixLt(:,2)+...
```

```
    xtremepixLt(:,3)),0.5*(xtremepixRt(:,2)+xtremepixRt(:,3)),...
    om,T,fc_left,cc_left,kc_left,alpha_c_left,fc_right,cc_right,...
    kc_right,alpha_c_right);
[baseL baseR]=stereo_triangulation(xtremepixLt(:,1),...
    xtremepixRt(:,1),om,T,fc_left,cc_left,kc_left,alpha_c_left,...
    fc_right,cc_right,kc_right,alpha_c_right);
% [kinkL kinkR]=stereo_triangulation(0.5*(kinkpixLt(:,1)+...
%     kinkpixLt(:,2)),0.5*(kinkpixRt(:,1)+kinkpixRt(:,2)),...
%     om,T,fc_left,cc_left,kc_left,alpha_c_left,fc_right,...
%     cc_right,kc_right,alpha_c_right);

basevecC(:,k)=baseR;
topvecC(:,k)=topR;
% kinkvecC(:,k)=kinkR;

end

meanbaseJD=[mean(basevecC(1,:)) mean(basevecC(3,:)) ...
    mean(basevecC(2,:))];
% using my measure for the base
% loop through and calc angles based on 2 different base points
for k=1:maxind

topR=topvecC(:,k);

%[kappaval phival]=RMX_Find_Angles(topR,meanbaseH);
[kappaval2 phival2]=RMX_Find_Angles(topR,meanbaseJD);
```

```
%kappavecC(k,1)=kappaval;
%phivecC(k,1)=phival;
kappavecCm(k,1)=kappaval2;
phivecCm(k,1)=phival2;

end

save kappavecC kappavecC;
save kappavecCm kappavecCm;
save phivecC phivecC;
save phivecCm phivecCm;
save basevecC basevecC;
save topvecC topvecC;

% find tilt angle based on fitting plane to top data
x=topvecC(1,:); y=topvecC(3,:); z=topvecC(2,:);
Xcol=x(:); Ycol=y(:); Zcol=z(:); Const = ones(size(Xcol));
Coefficients = [Xcol Ycol Const]\Zcol; % Find the coefficients
XCoeff = Coefficients(1); YCoeff = Coefficients(2);...
    CCoeff = Coefficients(3);
figure(3)
L=plot3(x,y,z,'ro'); % Plot the original data points
set(L,'Markersize',2*get(L,'Markersize')) % Make circle markers larger
set(L,'Markerfacecolor','r') % Filling in the markers
hold on
[xx, yy]=meshgrid(floor(min(Xcol)):0.2:ceil(max(Xcol)),...
    floor(min(Ycol)):0.2:ceil(max(Ycol))); % regular grid for plotting
zz = XCoeff * xx + YCoeff * yy + CCoeff;
```

```
surf(xx,yy,zz) % Plotting the surface
title(sprintf('Plotting plane z=(%f)*x+(%f)*y+(%f)',...
    XCoeff, YCoeff, CCoeff))

% calc tilt angle. normal of plane is a=(-Xcoeff,-YCoeff,1)
% dotted with b=(0,0,1) is 1
a=[-XCoeff -YCoeff 1]; b=[0 0 1];
Na=norm(a); Nb=norm(b);
tiltang=acos(dot(a,b)/(Na*Nb))*180/pi;
tiltazi=atan2(YCoeff,XCoeff)*180/pi;
```

A.6. Procedure to locate corners of contour in rod tracking

```
function [ xtremepix xtremepixt] = RMX_Contour_Pix(Cont,xmin,ymin)

points=zeros(2,5); pint=zeros(2,3); maxpoint=zeros(2,length(Cont));
maxdist=zeros(1,length(Cont)); num=5;
slopes=zeros(length(Cont),1);
for i=1:length(Cont)-(num-1)
    for k=1:num
        points(:,k)=Cont(:,i+k-1);
    end
    % find line from p1 to p5
    x1 = points(1,1); y1 = points(2,1);
    x5 = points(1,5); y5 = points(2,5);
    m1 = (y5-y1)/(x5-x1);
    slopes(i)=m1;
    b1 = y1-m1*x1;
    mp = -1/m1; % slope of perpendicular line
    % find b for all other points
```

```
    b2 = points(2,2)-mp*points(1,2);
    b3 = points(2,3)-mp*points(1,3);
    b4 = points(2,4)-mp*points(1,4);
    % find intersection point of lines
    pint(:,1)=[(b1-b2)/(mp-m1) mp*(b1-b2)/(mp-m1)+b2]';
    % intersection point of perp line from p2 and line from p1 to p5
    pint(:,2)=[(b1-b3)/(mp-m1) mp*(b1-b3)/(mp-m1)+b3]';
    pint(:,3)=[(b1-b4)/(mp-m1) mp*(b1-b4)/(mp-m1)+b4]';
    maxd=0;
    for j=1:3
        if (norm(points(:,j+1)-pint(:,j))>maxd)
            maxd=norm(points(:,j+1)-pint(:,j));
            maxpoint(:,i)=points(:,j+1);
        end
    end
    maxdist(1,i)=maxd/(norm(points(:,1)-points(:,num)));
    %normailizing by distance between p1 and pnum
end


xtremepix=zeros(2,3);
% find base pixel
max=0;
for i=1:length(Cont)
    if (Cont(2,i)>max)&&(Cont(2,i)<200)
        max=Cont(2,i);
        xtremepix(:,1)=Cont(:,i);
        baseindex=i;
    end
```

```
end

% need to find maxdist points which will be topL, topR
% in loop, say that maxdist<1 so we don't get outliers
maxd1=0; maxd2=0; maxd3=0;
for i=2:length(maxdist)-1
    if (maxpoint(1,i)>10)&&(Cont(2,i)<100)&&(maxdist(i)>maxd1)&&...
            (maxdist(i)>maxd2)&&(maxdist(i)<1)&&...
            (norm(maxpoint(:,i)-maxpoint(:,i+1))<5)&&...
            (norm(maxpoint(:,i)-maxpoint(:,i-1))<5)
        maxd1=maxdist(i);
        xtremepix(:,2)=maxpoint(:,i);
        topindex2=i;
    end
end
for i=2:length(maxdist)-1
    if (maxpoint(1,i)>10)&&(norm(maxpoint(:,i)-xtremepix(:,2))>5)&&...
            (Cont(2,i)<100)&&(maxdist(i)<maxd1)&&...
            (maxdist(i)>maxd2)&&...
            (norm(maxpoint(:,i)-maxpoint(:,i+1))<5)&&...
            (norm(maxpoint(:,i)-maxpoint(:,i-1))<5)
        maxd2=maxdist(i);
        xtremepix(:,3)=maxpoint(:,i);
        topindex3=i;
    end
end
for i=2:length(maxdist)-1
    if (maxpoint(1,i)>10)&&(norm(maxpoint(:,i)-xtremepix(:,2))>5)&&...
```

```
            (norm(maxpoint(:,i)-xtremepix(:,3))>5)&&...
            (Cont(2,i)<100)&&(maxdist(i)<maxd1)&&...
            (maxdist(i)<maxd2)&&(maxdist(i)>maxd3)&&...
            (norm(maxpoint(:,i)-maxpoint(:,i+1))<5)&&...
            (norm(maxpoint(:,i)-maxpoint(:,i-1))<5)
        maxd3=maxdist(i);
        temppix=maxpoint(:,i);
        topindex4=i;
    end
end

% set up conditions to weed out bumps due to contour error
if (norm(xtremepix(:,2)-xtremepix(:,3))>12)&&...
        (norm(xtremepix(:,2)-temppix)>12)&&...
        (norm(xtremepix(:,3)-temppix)<12)
    xtremepix(:,2)=temppix;
    topindex2=topindex4;
end
if (norm(xtremepix(:,2)-xtremepix(:,3))>12)&&...
        (norm(xtremepix(:,3)-temppix)>12)&&...
        (norm(xtremepix(:,2)-temppix)<12)
    xtremepix(:,3)=temppix;
    topindex3=topindex4;
end

kinkpix=zeros(2,2);
maxd3=0; maxd4=0;
for i=2:length(maxdist)-1
```

```
    if (maxpoint(1,i)>10)&&(norm(maxpoint(:,i)-xtremepix(:,1))>5)&&...
            (Cont(2,i)>100)&&(maxdist(i)>maxd3)&&...
            (maxdist(i)>maxd4)&&(maxdist(i)<1)&&...
            (norm(maxpoint(:,i)-maxpoint(:,i+1))<5)&&...
            (norm(maxpoint(:,i)-maxpoint(:,i-1))<5)
        maxd3=maxdist(i);
        kinkpix(:,1)=maxpoint(:,i);
        kinkindex1=i;
    end
end
for i=2:length(maxdist)-1
    if (maxpoint(1,i)>10)&&(norm(kinkpix(:,1)-maxpoint(:,i))>5)&&...
            (norm(maxpoint(:,i)-xtremepix(:,1))>5)&&...
            (Cont(2,i)>100)&&(maxdist(i)<maxd3)&&...
            (maxdist(i)>maxd4)&&(maxdist(i)<1)&&...
            (norm(maxpoint(:,i)-maxpoint(:,i+1))<5)&&...
            (norm(maxpoint(:,i)-maxpoint(:,i-1))<5)
        maxd4=maxdist(i);
        kinkpix(:,2)=maxpoint(:,i);
        kinkindex2=i;
    end
end

xtremeindex=[baseindex topindex2 topindex3]';
kinkindex=[kinkindex1 kinkindex2]';

xtremepixt=xtremepix+[(xmin-1)*ones(1,3) ; (ymin-1)*ones(1,3)];
```

```
end
```

A.7. Procedure to test angle data on rod silhouettes

```
function [ minpix maxpix minpixL maxpixL ] = ...
RMX_Find_Silhouette( kappa,beta,phi,baseL )

addpath('TOOLBOX_calib')
load('Calib_Results_stereoNewSiliconeOil')

scale=10.15;
Rc=scale*(2.8); %rad of curv Leandra's 10/22/07 meas 28mm
l=scale; dt=0.05; %length of rod and discretization size
centerline=zeros(3,round(l/dt)); %center line coords
inrad=scale*0.074/2; %should be .074
nvec=zeros(3,round(l/dt)); %normal vector
bvec=zeros(3,round(l/dt));  %binormal vector

dth=dt;
circle=zeros(3,round(2*pi/dth)); %3D circle around each CL pt
newcirc=circle; newcircprime=circle; %circle shifted properly
pixR=zeros(2,round(2*pi/dth)); pixL=pixR; %pixel coords circle
maxpix=zeros(2,round(l/dt)); minpix=maxpix;
maxpixL=zeros(2,round(l/dt)); minpixL=maxpixL;
rotphi=[cos(phi) -sin(phi) 0; sin(phi) cos(phi) 0; 0 0 1];
%rotation matrix based on LEFT frame

% modeltop(1,1)=2*Rc*sin(kappa)*cos((l-l)/(2*Rc))*sin((l)/(2*Rc));
% modeltop(2,1)=0;
% modeltop(3,1)=2*Rc*cos(kappa)*cos((l-l)/(2*Rc))*sin((l)/(2*Rc));
```

```
% modeltop=rotphi*modeltop;
%
% trans(1,1)=topL(1)-modeltop(2);
% trans(2,1)=topL(2)+modeltop(3);
% trans(3,1)=topL(3)-modeltop(1);

for i=0:l/dt-1
    % centerline parametrization from LHZ thesis
    centerline(1,i+1)=-2*Rc*cos(beta)*cos(kappa)*sin((l-i*dt)/...
        (2*Rc))*sin((i*dt)/(2*Rc))+2*Rc*sin(kappa)*...
        cos((l-i*dt)/(2*Rc))*sin((i*dt)/(2*Rc));
    centerline(2,i+1)=-2*Rc*sin(beta)*sin((l-i*dt)/(2*Rc))*...
        sin((i*dt)/(2*Rc));
    centerline(3,i+1)=2*Rc*cos(kappa)*cos((l-i*dt)/(2*Rc))*...
        sin((i*dt)/(2*Rc))+2*Rc*cos(beta)*sin(kappa)*...
        sin((l-i*dt)/(2*Rc))*sin((i*dt)/(2*Rc));

    % normal unit vector
    nvec(1,i+1)=sin(kappa)*sin((l-2*i*dt)/(2*Rc))+cos(beta)*...
        cos(kappa)*cos((l-2*i*dt)/(2*Rc));
    nvec(2,i+1)=sin(beta)*cos((l-2*i*dt)/(2*Rc));
    nvec(3,i+1)=cos(kappa)*sin((l-2*i*dt)/(2*Rc))-...
        cos(beta)*sin(kappa)*cos((l-2*i*dt)/(2*Rc));

    % binormal unit vector
    bvec(1,i+1)=-cos(kappa)*sin(beta);
    bvec(2,i+1)=cos(beta);
    bvec(3,i+1)=sin(kappa)*sin(beta);
```

```
minpixelR=2000; maxpixelR=0;
minpixelL=2000; maxpixelL=0;

for j=0:round(2*pi/dth)-1
    circle(:,j+1)=centerline(:,i+1)+inrad*nvec(:,i+1)*...
        sin(j*dth)+inrad*bvec(:,i+1)*cos(j*dth);
    circle(:,j+1)=rotphi*circle(:,j+1);
    % translate circle to match coords
    newcirc(1,j+1)=circle(2,j+1)+baseL(1);
    newcirc(2,j+1)=-circle(3,j+1)+baseL(2);
    newcirc(3,j+1)=circle(1,j+1)+baseL(3);

    % invert 3D coords to right pixel frame
    [xp,dxpdom,dxpdT,dxpdf,dxpdc,dxpdk,dxpdalpha] = ...
        project_points2(newcirc(:,j+1),om,T,fc_right,...
        cc_right,kc_right,alpha_c_right);
    pixR(:,j+1)=xp(:);

    % invert 3D coords to left pixel frame
    newcircprime(:,j+1)=R'*(newcirc(:,j+1)-T);
    [xpL,dxpdom,dxpdT,dxpdf,dxpdc,dxpdk,dxpdalpha] = ...
        project_points2(newcircprime(:,j+1),om,T,...
        fc_left,cc_left,kc_left,alpha_c_left);
    pixL(:,j+1)=xpL(:);

    % find extremal pixels
    if pixR(1,j+1)<minpixelR
        minpix(:,i+1)=pixR(:,j+1);
```

```
            minpixelR=pixR(1,j+1);
        end
        if pixR(1,j+1)>maxpixelR
            maxpix(:,i+1)=pixR(:,j+1);
            maxpixelR=pixR(1,j+1);
        end

        if pixL(1,j+1)<minpixelL
            minpixL(:,i+1)=pixL(:,j+1);
            minpixelL=pixL(1,j+1);
        end
        if pixL(1,j+1)>maxpixelL
            maxpixL(:,i+1)=pixL(:,j+1);
            maxpixelL=pixL(1,j+1);
        end
    end
end
end
```

Appendix B: Mathematica Programs

B.1. Lubrication Theory

```
KK[s_] := 1/s - Coth[s];
XX[s_] := Coth[s] - 1;
f[s_] := Simplify[KK''[s]/KK'[s] + 3/s + (2 KK[s])/(s^2 KK'[s])];
g[s_] := Simplify[-(KK''[s]/(s KK'[s])) - 4/s^2 - (2 KK[s])/(
    s^3 KK'[s])];
nh[s_] := XX''[s]/(s KK'[s]);
(* Need to make sure the series below
are expanded to at least the number of terms
as you need *)
p = Simplify[Series[s f[s], {s, 0, 50}]];
q = Simplify[Series[s^2 g[s], {s, 0, 50}]];
gnh = Simplify[Series[s^4 nh[s], {s, 0, 50}]];
(* below is the potential - it should be greater
than zero for large s *)
H[s_] := Simplify[1/4 f[s]^2 + 1/2 f'[s] - g[s]];
Plot[H[s], {s, 0, 10000}]
Limit[H[s], s -> \[Infinity]]


NUM = 80; \[Alpha] = -2; a0 = N[-3/5]; a =
 ConstantArray[0, 2 NUM]; Do[
 a[[2 n]] = (-Coefficient[gnh, s,
       2 n] + (Coefficient[p, s, 2 (n) + 2] (\[Alpha] - 3) a0) + \!\(
\*UnderoverscriptBox[\(\[Sum]\), \(k =
        2\), \(n\)]\((Coefficient[p, s,
         2\ \((n - k)\) + 2]\ \((\[Alpha] + 2\ k -
```

```
          3)\) a[\([\)\(2\ k - 2\)\(]\)])\)\))/((\[Alpha] +
       2 n)^2 + (N[Coefficient[p, s, 0]] - 1) (\[Alpha] + 2 n) +
     N[Coefficient[q, s, 0]]), {n, 1, NUM}]; a;
AI[s_] := s^(-2) (a0 + \!\(
\*UnderoverscriptBox[\(\[Sum]\), \(n =
       1\), \(NUM\)]\(a[\([\)\(2\ n\)\(]\)]\ s^\((2\ n)\)\)\))
series[s_] := s^2 AI[s]; Expand[AI[s], s]; pN = Plot[AI[s], {s, 0, 1}];
zurros = s /. NSolve[series[s] == 0, s];
Min[Abs[zurros]]
Abs[zurros[[1]]]
pzurro = ListPlot[{Re[#], Im[#]} & /@ zurros, AxesOrigin -> {0, 0},
   PlotRange -> {{-4.5, 4.5}, {-4.5, 4.5}}, ImagePadding -> 40,
   AspectRatio -> 1, Frame -> True,
   FrameLabel -> {{Im, None}, {Re, "complex plane"}},
   PlotStyle -> Directive[Red, PointSize[.02]], ImageSize -> 600];
Show[pzurro]

NUM = 80; \[Alpha] = -2 + Sqrt[10]; b0 = -1; b =
 ConstantArray[0, 2 NUM];
Do[b[[2 n]] = ((N[
        Coefficient[p, s, 2 (n) + 2]] (\[Alpha] - 3) b0) + \!\(
\*UnderoverscriptBox[\(\[Sum]\), \(k =
        2\), \(n\)]\((N[
         Coefficient[p, s, 2\ \((n - k)\) + 2]]\ \((\[Alpha] + 2\ k -
          3)\) b[\([\)\(2\ k - 2\)\(]\)])\)\))/((\[Alpha] +
       2 n)^2 + (N[Coefficient[p, s, 0]] - 1) (\[Alpha] + 2 n) +
     N[Coefficient[q, s, 0]]), {n, 1, NUM}]; b;
AII[s_] := s^(-2 + Sqrt[10]) (b0 + \!\(
```

```
\*UnderoverscriptBox[\(\[Sum]\), \(n =
       1\), \(NUM\)]\(b[\([\)\(2\ n\)\(]\)]\ s^\((2\ n)\)\)\))
seriesH[s_] := s^(2 - Sqrt[10]) AII[s]; Expand[AII[s], s]; pH =
 Plot[AII[s], {s, 0, 1}];
zurrosH = s /. NSolve[seriesH[s] == 0, s];
Min[Abs[zurrosH]]
Abs[zurrosH[[1]]]
pzurroH =
  ListPlot[{Re[#], Im[#]} & /@ zurrosH, AxesOrigin -> {0, 0},
   PlotRange -> {{-4.5, 4.5}, {-4.5, 4.5}}, ImagePadding -> 40,
   AspectRatio -> 1, Frame -> True,
   FrameLabel -> {{Im, None}, {Re, "complex plane"}},
   PlotStyle -> Directive[Red, PointSize[.02]], ImageSize -> 600];
Show[pzurroH]
```

B.2. Numerical integration to find homogeneous and particular solutions

```
x0 = .05;
x1 = 5.6;
f0 = N[s^2 AI[s] /. s -> x0];
f0P = N[D[s^2 AI[s], s] /. s -> x0];
t = NDSolve[{s KK'[s] (funN^\[Prime]\[Prime])[s] +
      Derivative[1][funN][s] (s KK''[s] - KK'[s] + 2 s^(-1) KK[s]) -
      funN[s] (3 KK''[s] + 4 s^(-1) KK'[s] + 6 s^(-2) KK[s]) +
      s^2 XX''[s] == 0, funN[x0] == f0, funN'[x0] == f0P},
   funN, {s, x0, x1}];
APart[s_] := Evaluate[funN[s]/s^2 /. t];
Plot[APart[s], {s, x0, x1}, ImageSize -> 600]


x0 = .05;
```

```
x1 = 5.6;
f0h = N[s^(2 - Sqrt[10]) AII[s] /. s -> x0];
f0Ph = N[D[s^(2 - Sqrt[10]) AII[s], s] /. s -> x0];
t1 = NDSolve[{s KK'[s] (funH^\[Prime]\[Prime])[
        s] + (s KK''[s] + (-1 + 2 Sqrt[10]) KK'[s] +
         2 s^-1 KK[s]) Derivative[1][funH][
        s] + ((-3 + Sqrt[10]) KK''[s] + (6 - 2 Sqrt[10]) s^-1 KK'[
           s] + (-6 + 2 Sqrt[10]) s^-2 KK[s]) funH[s] == 0,
    funH[x0] == f0h, funH'[x0] == f0Ph}, funH, {s, x0, x1}];
AHom[s_] := (.18629) Evaluate[funH[s]/s^(2 - Sqrt[10]) /. t1];
Plot[AHom[s], {s, x0, x1}, ImageSize -> 600]

Afull[s_] := APart[s] + AHom[s];
Plot[Afull[s], {s, x0, x1}, ImageSize -> 600]
```

B.3. Obtaining particle trajectories

```
KK[s_] := s^(-1) - Coth[s];
V0[var_, s_] := -E^(s var) (var^2 + var/s) + (E^(-s) Sinh[s var])/s^2;
V1[var_, s_] :=
  E^(-s var) (var^2/s + (3 var)/s^2) - (3 E^(-s) Sinh[s var])/s^3;
V2[var_, s_] := E^(-s var) (var^2 + (3 var)/s);
BB[s_] := s Afull''[s] + Afull'[s] - Afull[s]/s + 9/(5 s^3);
CC[s_] := (s Afull''[s] - Afull'[s]) KK[s] + (9/5) (E^(-s) - 1)/s^3;
FF[s_] := Afull[s] - s Afull'[s] + 9/(5 s^2);
GG[s_] := (2 Afull[s] - s Afull'[s]) KK[s] - 9/(5 s^2);
DD[s_] := s Afull'[s] + Afull[s] - 3/(5 s^2);
EE[s_] :=
  s Afull'[s] KK[s] - (3/5) (E^(-s) - 1)/s^2 + 2 (Coth[s] - 1);
```

```
Ntot = 100;
cut = 12;
U = 1;
dt = 1/10;
points1 = ConstantArray[0, Ntot];
points2 = ConstantArray[0, Ntot];
points3 = ConstantArray[0, Ntot];
r0 = 1.6; z0 = 0.25; th0 = N[11 Pi/12];
points1[[1]] = r0; points2[[1]] = th0; points3[[1]] = z0;
Do[eta = (2 points1[[i]])/(points1[[i]]^2 + points3[[i]]^2);
 xi = (2 points3[[i]])/(points1[[i]]^2 + points3[[i]]^2);
 \[Phi] = (xi^2 + eta^2)^(1/2) NIntegrate[
    Afull[s] Sinh[s xi] BesselJ[1, s eta], {s, x0, x1}];
 Q0 = (1/2) (xi^2 + eta^2)^(1/
      2) NIntegrate[(BB[s] Cosh[s xi] + CC[s] Sinh[s xi]) BesselJ[1,
      s eta], {s, x0, x1}];
 Q1 = eta (xi^2 + eta^2) + (xi^2 + eta^2)^(1/2) NIntegrate[
     V1[xi, s] BesselJ[1, s eta], {s, x0, x1}];
 Q = Q0 + (3/10) Q1;
 \[Chi]0 = (xi^2 + eta^2)^(1/
      2) NIntegrate[(FF[s] Cosh[s xi] + GG[s] Sinh[s xi]) BesselJ[2,
      s eta], {s, x0, x1}];
 \[Chi]1 = -eta^2 + (xi^2 + eta^2)^(1/2) NIntegrate[
     V2[xi, s] BesselJ[2, s eta], {s, x0, x1}];
 \[Chi] = \[Chi]0 + (3/5) \[Chi]1;
 \[Psi]0 = (xi^2 + eta^2)^(1/
      2) NIntegrate[(DD[s] Cosh[s xi] + EE[s] Sinh[s xi]) BesselJ[0,
      s eta], {s, x0, x1}];
```

```
 \[Psi]1 = -eta^2 + (xi^2 + eta^2)^(1/2) NIntegrate[
     V0[xi, s] BesselJ[0, s eta], {s, x0, x1}];
 \[Psi] = \[Psi]0 + (3/5) \[Psi]1;
 u = U (points1[[i]] Q + (1/2) (\[Psi] + \[Chi])) Cos[points2[[i]]];
 v = U (1/2) (\[Chi] - \[Psi]) Sin[points2[[i]]];
 w = U (points3[[i]] Q + \[Phi]) Cos[points2[[i]]];
 points1[[i + 1]] = points1[[i]] + u dt;
 points2[[i + 1]] = points2[[i]] + v dt;
 points3[[i + 1]] = points3[[i]] + w dt;
 , {i, cut}]
trun = 1 + cut;
r = Flatten[points1[[1 ;; trun]]];
x = Flatten[r Cos[points2[[1 ;; trun]]]];
y = Flatten[r Sin[points2[[1 ;; trun]]]];
z = Flatten[points3[[1 ;; trun]]];
data7 = ConstantArray[0, {trun, 3}];
Do[data7[[i]] = {x[[i]], y[[i]], z[[i]]}, {i, 1, trun}]
```

References

1. J.R. Blake and A.T. Chwang, *Fundamental singularities of viscous flow*, Journal of Engineering Mathematics **8** (1974), no. 1, 23–29 (English).

2. Roberto Camassa, Terry Jo Leiterman, and Richard M. McLaughlin, *Trajectory and flow properties for a rod spinning in a viscous fluid. I. An exact solution*, J. Fluid Mech. **612** (2008), 153–200. MR 2457587 (2010c:76037)

3. Roberto Camassa, James Martindale, and Richard McLaughlin, *A comparison of lagrangian trajectories between classical lubrication theory and singularity methods for a sphere translating parallel to a nearby no-slip plane*, 2013.

4. Roberto Camassa, James Martindale, Richard McLaughlin, and Leandra Vicci, *On the precession of a soft-magnetic slender body in a highly viscous fluid.*, 2013.

5. Roberto Camassa, James Martindale, Richard McLaughlin, Leandra Vicci, and Longhua Zhao, *Large-scale toroidal structures induced by the precession of a bent rod in a highly viscous fluid.*, 2013.

6. J.H.E. Cartwright, O. Piro, and I. Tuval, *Fluid-dynamical basis of the embryonic development of left-right asymmetry in vertebrates.*, Proc Natl Acad Sci U S A **101** (2004), no. 19, 7234–9.

7. Allen T. Chwang and T. Yao Tsu Wu, *Hydromechanics of low-Reynolds-number flow. II. Singularity method for Stokes flows*, J. Fluid Mech. **67** (1975), 787–815. MR 0368585 (51 #4826)

8. H. Hamada, *Breakthroughs and future challenges in left-right patterning.*, Dev Growth Differ **50 Suppl 1** (2008).

9. J. Happel and H. Brenner, *Low Reynolds Number Hydrodynamics*, (1965).

10. John David Jackson, *Classical electrodynamics*, 3rd ed. ed., Wiley, New York, NY, 1999.

11. Terry Jo Leiterman, *Exact and asymptotic low reynolds, time-varying solutions for spinning rods with a comparison to experiments on the micro and macroscale*, 2006.

12. M. E. O'Neill and K. Stewartson, *On the slow motion of a sphere parallel to a nearby plane wall*, J. Fluid Mech. **27** (1967), 705–724. MR 0210375 (35 #1268)

13. M.E. O'Neill, *On the separation of a slow linear shear flow from a cylindrical ridge or trough in a plane.*, Z. Angew. Math. Phys. **28** (1977), 439–448 (English).

14. K. Shinohara, A. Kawasumi, A. Takamatsu, S. Yoshiba, Y. Botilde, N. Motoyama, W. Reith, B. Durand, H. Shiratori, and H. Hamada, *Two rotating cilia in the node cavity are sufficient to break left-right symmetry in the mouse embryo.*, Nat Commun **3** (2012).

15. D. J. Smith, A. A. Smith, and J. R. Blake, *Mathematical embryology: the fluid mechanics of nodal cilia*, J. Engrg. Math. **70** (2011), no. 1-3, 255–279. MR 2803465 (2012g:92104)

16. Longhua Zhao, *Fluid-structure interaction in viscous dominated flows*, 2010, Copyright - Copyright ProQuest, UMI Dissertations Publishing 2010; Last updated - 2010-09-30; DOI - 2140413571; 54293061; 66569; 9781124171456; 3418643; First page - n/a; M1: 3418643; M3: Ph.D.